Title
MASS TRANSFER AND TRANSPORT OF RADIONUCLIDES IN FRACTURED POROUS ROCK

Author
Ahn, J.

Publication Date
1988-04-01

Lawrence Berkeley Laboratory
UNIVERSITY OF CALIFORNIA

EARTH SCIENCES DIVISION

Mass Transfer and Transport of Radionuclides in Fractured Porous Rock

J. Ahn
(Ph.D. Thesis)

April 1988

Prepared for the U.S. Department of Energy under Contract Number DE-AC03-76SF00098.

DISCLAIMER

LBL-25594

MASS TRANSFER AND TRANSPORT OF RADIONUCLIDES IN FRACTURED POROUS ROCK

Joonhong Ahn
Ph.D. Thesis

Lawrence Berkeley Laboratory
University of California
Berkeley, CA 94720

April 1988

This work was supported by the U.S. Department of Energy under Contract No. DE-AC03-76SF00098.

Mass Transfer and Transport of Radionuclides

in Fractured Porous Rock

by

Joonhong Ahn

Mass Transfer and Transport of Radionuclides in Fractured Porous Rock

by

Joonhong Ahn

Abstract

Analytical studies are made to predict space-time-dependent concentrations of radionuclides transported through water-saturated fractured porous rock. A basic model, which is expected to generate conservative results when used in long-term safety assessment of geologic repositories for radioactive waste, is established. Applicability and limitations of the model are investigated.

In the basic model, one-dimensional advection in a single planar fracture of infinite extent is coupled with diffusion in the rock matrix perpendicular to the fracture. Sorption and radioactive decay with no precursors are included. Matrix diffusion and radioactive decay make contaminant stay within some distance away from the source releasing contaminant for a finite period of time. Back diffusion is observed after the release period in the vicinity of the fracture entrance.

Though enhancing early-time transport, longitudinal dispersion in the fracture may be neglected for long-term evaluations by assuming greater advection and fracture apertures than actual values. For multiple parallel fractures, the single-fracture model is still applicable for moderate overlap of concentration fields inside the rock matrix. Neglecting radioactive-decay precursors results in overly optimistic estimates of concentration in the fracture in early times. Transverse dispersion merges plumes released from individual waste forms in a repository. Beyond the near region, the repository is treated as a single large source. An equivalent single-finite-source solution is a very good approximation.

Mass transfer and transport from a cylindrical waste solid are studied in the cylindrical geometry by assuming molecular diffusion in the rock matrix parallel to, as well as perpendicular to the fracture, without advection. Radioactive decay enhances mass release from the cylinder. Even though the mass flux from the waste into rock is lower than to the fracture because of lower porosity, the larger waste surface exposed to the rock matrix and the greater matrix sorption can result in greater release rate to the matrix. With diffusion only, the basic model cannot be conservative against the cylinder model, with respect to the diffusive mass flux from the waste surface and to the distance that the contaminant can reach.

Acknowledgements

I would like to take this opportunity to thank Professor Thomas H. Pigford and Professor Paul L. Chambré. They have been continuously and patiently guiding my research work, with great enthusiasm. They gave me stimulating discussions and showed me clearly what the logical argument should be. If this dissertation is illogical, the responsibilities are all mine. Without their support, this work could not have been completed. It has been a great pleasure for me to make this dissertation completed with such scholars of outstanding excellence.

I also wish to express my gratitude to Professor Paul A. Witherspoon for his reviewing my thesis and giving very helpful comments.

This work was suppported by the United States Department of Energy. Discussions with Dr. A. B. Gureghian of Office of Waste Technology Development (OWTD) of Battelle Project Management Division were especially insightful and helpful. Dr. William W.-L. Lee in Lawrence Berkeley Laboratory gave me quite a lot of helpful suggestions when I prepared reports for OWTD.

I will never forget the life in the International House spent for the first four years in Berkeley. The then residents who came from Japan as visiting scholars or graduate students encouraged me when I was depressed. I am especially indebted to Dr. Jun-ichi Tanaka, Dr. Shigeru Ogawa, Ms. Eiko Saito, Mr. Masashi Matsui, Professor Masashi Kaneko and Professor Eizo Matsuki, if I name a few of them.

Last but not least, I cannot thank my parents enough for their continuous encouragement and support. I would like to dedicate this thesis to them with my greatest thanks.

Joonhong Ahn
Berkeley, California
April 1988

Table of Contents

List of Figures

Chapter 1
Introduction and Summary

1.1 Introduction

A geological waste repository will be the final reservoir for radioactivity generated by nuclear power. It will remain radioactive for a very long time, with some radioactivity even remaining for millions of years. As yet, complete analyses for predicting safety of geological disposal are not available. Such analyses would include three stages, proceeding from the assumption that water will be the only vehicle for transport from the repository to people: (1) failure of the artificial containment and subsequent water intrusion, (2) contaminant migration by groundwater to the biosphere, and (3) injestion of radioactivity by human beings [1]. This dissertation deals with processes involved in migration of contaminants to the biosphere.

In a geological disposal system, radioactivity is confined by engineered barriers and dense geological formations. Engineered barriers may include inert waste solid, such as borosilicate glass, a container, and backfill. Engineered barriers are especially effective for confining relatively short half-life nuclides such as ^{90}Sr and ^{137}Cs. The geological formation surrounding the waste repository plays an important role in the case of long-lived actinides. It is essential for predicting the safety of the geological disposal system to understand how radionuclides are transported into and through geological layers.

The prime requirement for the rock hosting the waste solid is low permeability and porosity. The waste repository would be constructed at depth of several hundred meters below the surface, where the permeability of some dense host rocks may be completely due to fractures. Fractures have permeabilities several orders of magnitude larger than the rock matrix itself, if the geological layers are fully saturated with water. Assuming that hydrogeologic migration of radionuclides is very slow because the porosity of the saturated rock matrix is very low might lead to overly optimistic estimates of repository performance.

For a saturated fractured porous medium, two approaches are considered. In one approach it is assumed that regional flow through great volumes of fractured rock cannot be analyzed by describing each of the discrete fractures deterministically, and that continuum or equivalent-porous-media analysis can be used if equivalent-porous-medium parameters can be assigned to the fractured system [2]. If such an equivalent porous medium exists, then we can apply earlier analyses of mass transfer and transport through a porous medium [3–6]. In the other approach fractures of large aperture are considered to be of special importance to safety assessment of waste disposal. Fractures are divided into principal and minor fractures depending on their aperture. Principal fractures are considered as main paths to the biosphere, whereas minor fractures are considered as pores together with other void spaces in rock matrix (Figure 1.1).

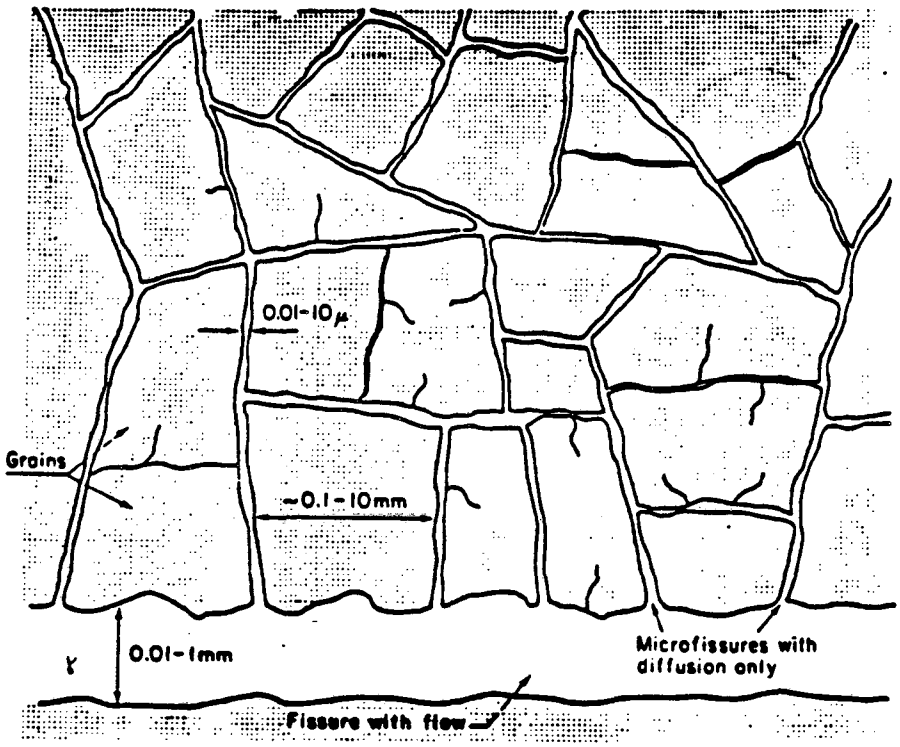

Figure 1.1 A two dimensional view of the microstructure in granite showing typical sizes of grains, microfractures and fractures (Source: *Birgersson and Neretnieks* [8])

To have an equivalent porous medium, a fractured medium of interest must have the following properties: (1) fracture number density is sufficiently high, (2) fractures have similar apertures rather than broadly-distributed apertures, (3) fractures have distributed orientations rather than uniform orientation, and (4) the medium has a representative elementary volume (REV) [2]. An REV can be thought as follows: Porous media actually consist of pores and solid. Microscopically, rocks are heterogeneous media. By taking a large enough volume of rock, we can average over the volume various rock properties such as porosity and density and consider the averaged properties to apply at every point inside the volume.

It is observed, however, in candidate geological formations such as granite, basalt and tuff that fracture apertures have log-normal distribution [2]. The log-normal distribution of fracture apertures implies that there are a few fractures of large aperture and enormous numbers of microfractures. If this is the case of the waste repository, we should take the latter approach.

1.2 State of the Art

Studies of migration in discrete fractures with matrix diffusion were begun by *Neretnieks* [7] in early 80's. He first pointed out the importance of diffusion of radionuclides from the principal fractures to the surrounding rock matrix in the context of the waste disposal. Clear indication of matrix diffusion was obtained by *Birgersson and Neretnieks* [8][9] in the field tests in the Stripa mine, Sweden. In Neretnieks's model fractures and pores in rock matrix are assumed to be saturated with water. Water flows in fractures, whereas in rock pores water is assumed to be stationary. Fractures are simplified as planar parallel conduits. Molecular diffusion of the contaminant from fractures to the surrounding rock matrix was pointed out to be an important retention mechanism for transport in fractures.

Many efforts have been made for investigating transport through a fracture-matrix

system in natural environment or in laboratory experiments. One of the key issues in fracture-flow transport is how to deal with hydrodynamic dispersion in fractures. Fickian dispersion and channeling dispersion are two widely-accepted mechanisms. Channeling dispersion in fractures can be considered because in actual fractures both fracture walls contact with each other at various points, creating multiple water conduits in one fracture. Each conduit might have different hydraulic properties, such as path length and width, resulting in dispersion of the contaminant.

Abelin et al. [10] made an attempt to simulate tracer migration in natural fractures by applying Fickian and channeling dispersions. Migration was investigated by injecting tracer solution into a fracture and by measuring breakthrough curves at points about 10 m apart from the injection point. They also measured the concentration of the tracer in the rock matrix adjacent to the fracture, and obtained direct evidence of matrix diffusion. Observed breakthrough curves show long tailing after the injection is terminated. Both the Fickian and channeling models could yield very good "best-fit" curves for the long-tailed breakthrough curves, and they claimed that available data are not sufficient to firmly conclude which is the principal mechanism for dispersion.

Hadermann and Jakob [11] measured fracture-flow transport in laboratory experiment. They used drilling bore cores of crystalline rock originated from northern Switzerland. Fickian dispersion-advection model is applied. They pointed out that the main feature to be explained by any model is the trailing part of the breakthrough curves over long times, and proposed matrix diffusion, non-linear sorption, sorption kinetics, and channeling in fractures for possible mechanisms causing the trailing part. They chose matrix diffusion, with which they claimed that they could show quantitative consistency. Channeling model was not recommended there because the model could increase the number of independent parameters dramatically.

Reeves et al. [12] studied migration through the highly-fractured Culebra dolomite in the Waste Isolation Pilot Plant in New Mexico, and concluded that matrix diffusion is

very important as a retardation mechanism, and that fracture dispersivity exhibits a decidedly secondary importance.

Thus, experimentally the importance of matrix diffusion is well established whereas for the dispersion in fractures more discussions are still needed.

Many analytical studies have been done after *Neretnieks* [7]. They are based on the same assumptions made by Neretnieks: planar fractures, stationary water in rock pores, water flow in fractures, and matrix diffusion.

Rasmuson and Neretnieks [13] and *Tang et al.* [14] studied the effect of longitudinal hydrodynamic dispersion with a mathematical model and parameter sensitivity studies. Both studies claim that longitudinal dispersion has significant influence on early arrival of the contaminant. *Sudicky and Frind* [15] showed the effect of neighboring parallel fractures by solving the mathematical problem analytically. However, the analytical solutions proposed by them contain errors; the solutions do not satisfy the boundary conditions.

Effects of radioactive decay chains of multiple members are studied by *Chambré et al.* [5] and *Sudicky and Frind* [16]. In [5] an attempt was made to obtain the non-recursive analytical solution for a decay chain of arbitrary length, and the decay in the rock matrix was neglected. The recursive solution for a chain of arbitrary length was obtained as the preceding form of the approximated non-recursive solution. In [16], on the other hand, the solution for a two-member chain and for an impulse release at the fracture entrance is obtained analytically.

In these analytical studies, including this dissertation, the region of interest excludes the region near the repository, where repository heating and possible mechanical disturbance during the construction of the repository make the situation more complex. Because repository heating is a function of time, physical properties such as the molecular diffusion coefficient, the sorption distribution coefficient, and water viscosity would also be a function of time. Also in this near-region, hydrodynamic dispersion in the fracture may not be

a Fickian dispersion [17].

One important feature of fracture-flow transport which has never been discussed explicitly in the previous analytical studies is the intersection of fractures. Hydraulic properties of fracture network consisting of intersected fractures have been analyzed in [2], where contaminant transport associated with matrix diffusion, sorption, and hydrodynamic dispersion is not considered. Intersection of fractures introduces a lot of mathematical complexity. Moreover, we do not have enough data to establish a deterministic model, where we at least need to know the mean distance between intersections and angles formed by two intersected fractures. Three-dimensional description of fracture network might be necessary. It is unlikely to obtain such information in future. Rather, we should consider that for a considerably large distance repeated intersections of fractures make the contaminant well-mixed among these fractures, so that one averaged fracture can represent the transport phenomena. The effect of intersection, then, might be treated as the dispersion in mathematical models.

Besides these analytical studies, there are several numerical analyses available, usually by finite-element method [18][19] or the integrated finite-difference method [20]. Although numerical schemes can handle more complex systems, validation of results is usually a problem. Analytical studies are more suitable for validation of numerical schemes as well as parametric studies.

1.3 Purposes of This Dissertation

Transport models for radioactive contaminant through a fractured medium would be established aiming at two different goals. In one category, a transport model is established to explain in-situ experiments or to predict migration of contaminant for a certain specific repository site. The model would be required to generate numerically as close results as possible against experimental results. Numerical methods would be applied to incorporate complex physical and chemical mechanisms that are actually observed in the experiments.

In the other category, including this dissertation, a transport model is established in order to understand what are the key mechanisms and how they control the contaminant transport. The actual situation may be abstracted to emphasize important processes. Knowledge obtained from this type of studies can provide the logic for establishing future national criteria for long-term performance and repository-site selection.

The analyses in the second category stated above, then, should be performed from the standpoint of looking for a "bounding theory" for migration of radionuclides through a geological medium. Considering that before actual waste emplacement we must assure that the waste repository system, including the host rock, can confine radioactivity for tens of thousands to possibly millions of years, depending upon what national criteria are adopted for long-term performance, we must have a reliable theory that can predict migration of radionuclides for such a long time. Complicating the model is not necessary the best way to obtain a reliable model. Rather, we should investigate every physical processes that could affect migration and its relative importance, and establish a model with essential physical processes and assumptions that are reliably known to generate conservative results.

The previous analytical studies reviewed above lack the standpoint of looking for a bounding theory. For example, we saw that there are discussions and confusion about how to deal with hydrodynamic dispersion. If, however, we need a bounding theory, then we could neglect this mechanism in the model; what we need is the logic that assures that the model without hydrodynamic dispersion can generate conservative results. Another example is found in the study with the multiple-parallel-fracture model. Since there is no such fracture system as multiple parallel fractures in natural environment, increasing complexity of the model from a discrete fracture to multiple fractures does not directly contribute the reliability of safety assessment for the overall geologic disposal system. The meaning for increasing complexity should be sought in finding whether or when the discrete-fracture model becomes a conservative one.

In this dissertation, first the advection-dispersion-matrix diffusion model for a planar parallel fracture in the Cartesian coordinates is established as a basic bounding model. Then, the effects of longitudinal dispersion, adjacent fractures, multiple-member decay chains, and transverse dispersion with multiple patch sources are investigated by comparing a model incorporated with each of these mechanisms to the basic bounding model, to obtain under what conditions the proposed basic model can apply, or these effects can be neglected.

One remaining question is the effect of the planar geometry used instead of the cylindrical geometry of the candidate waste containers. The geometry would affect the near-field transport and mass transfer from the waste container, i.e., the source term for the far-field transport. It is important to understand how the near-field transport affects the far-field transport.

Thus, the purposes of this study can be summarized as (1) obtaining a basic, yet bounding model to predict the far-field transport of radionuclides through a fractured porous rock together with the conditions for applicability of the basic model, and (2) predicting the near-field mass transfer and transport from a cylindrical waste solid to a fractured porous rock and investigating how the difference in geometry would affect the far-field transport.

1.4 Summary of Results and Conclusions

Chapter 2 is the key chapter in this thesis. Proposed there is the basic bounding model whose applicability and limitation are investigated in subsequent chapters. The basic bounding model is established based upon the following assumptions: (1) radioactive decay with no precursing nuclides, (2) a discrete fracture of infinite extent, filled with water, (3) rock matrix saturated with stationary water, (4) unidirectional flow in the fracture, (5) longitudinal hydrodynamic dispersion in the fracture, (6) one-dimensional molecular diffusion in the rock matrix, perpendicular to the fracture plane (7) local sorption

equilibrium between rock surfaces and water. The contaminant source is exposed only to the fracture and of infinite extent along the direction perpendicular to the flow direction, so the fracture is considered to be one-dimensional.

Analytical solutions for (1) the concentrations in the fracture and in the rock matrix, (2) advective mass flux in the fracture, and (3) cumulative release in the fracture are obtained for a source strength given as an arbitrary function of time, and with or without longitudinal dispersion in the fracture. Analytical solutions for a band release are also derived. The band release is defined by assuming congruent dissolution of the contaminant with the waste solid and no dispersion at the dissolution location. The waste solid is assumed to be dissolved for a leach time at a constant rate. Then, the concentration at the boundary vanishes after the leaching period.

The characteristics of the fracture-matrix transport are investigated with the basic bounding model in Chapters 2 and 4, using the band-release solutions. Matrix diffusion retards significantly the transport in the fracture even without sorption. Unlike transport through porous media, where the contaminated area advances chromatographically, the contaminant remains in the region near the source even after the source ceases emitting the contaminant, and eventually decays out. Chapter 4 gives new insight into how a contaminant is transported after the source ceases emitting the contaminant. In the vicinity of the fracture entrance, the contaminant diffuses back to the fracture because uncontaminated water is entering the fracture. The contaminant is, then, carried by advection in the fracture, and again diffuses into the rock matrix.

Followings are the summary of the applicability and limitations of the above-mentioned basic bounding model.

In Chapter 3 longitudinal dispersion in a fracture is investigated. Comparison of the cases, (1) infinite Pechlet number and large fracture aperture, and (2) small Pechlet number and realistically small fracture aperture, shows that in case (1) contaminant is transported to a farther point even at an early time. Over long times, especially after the

leaching period, matrix diffusion becomes dominant so that effects of longitudinal dispersion become negligible. Thus, longitudinal dispersion can be safely neglected by assuming large fracture aperture and water velocity compared to the values observed in natural environment.

Transverse dispersion in the fracture is studied in Chapter 7 with mutiple-patch sources of finite areal extent, by comparison of the multiple-patch solution with (1) the solution for the infinite-extent source obtained in Chapter 2, and with (2) the solution for a single-patch source equivalent to the multiple-patch source. The multiple-patch source would be better description of actual repository consisting of thousands of canisters than the infinite source. In the most near region from the source, where plumes generated from the patches are distinguishable, the multiple-patch-source solution must be used. Due to transverse dispersion, plumes generated from patches begin to merge with each other, and at some distance away from the repository these plumes are completely merged. There both the infinite-source and the equivalent-finite-single-patch solutions give identical results. At larger distance we can consider a repository as a finite single-patch source. Except the near region, the basic bounding model considered in Chapter 2 gives conservative results.

In Chapter 5, effects of multiple parallel fractures are investigated. *Sudicky and Frind* [15] gave analytical solutions that contain some serious errors. In Chapter 5 corrected solutions are given, and it is pointed out that the exact analytical solutions are not suitable for numerical evaluations for the case of shallow penetration into the rock matrix by molecular diffusion. A superposition approximation is proposed as an alternative. A maximum Fourier number is given for the criterion for a valid superposition. After the source ceases releasing the contaminant, the criterion becomes more limited. In a region very far from the source location superposition yields good approximation at any time because so little contaminant can reach there that penetration into the rock matrix is very shallow. This analysis is limited to a system of parallel fractures.

In Chapter 6 two-member chain transport through a single fracture is considered. Analytical solutions for a general release mode are derived, utilizing the analytical solutions for an instantaneous release obtained by *Sudicky and Frind* [16]. Numerical examples are given for a band release for the $^{237}Np \rightarrow {}^{233}U \rightarrow$ chain and the $^{234}U \rightarrow {}^{230}Th \rightarrow$ chain to compare with the results of *Chambré et al.* [5], who neglected radioactive decay in the rock matrix. Also investigated is the effect of presence of a mother nuclide, by comparing the ^{237}Np concentration obtained from a $^{241}Am \rightarrow {}^{237}Np \rightarrow$ chain with that from the assumption that ^{237}Np is a mother nuclide. Approximation applied by *Chambré et al.* is found to introduce considerable errors for the concentration of the daughter nuclide. Ignoring the presence of ^{241}Am in the source results in optimitic evaluation of maximum concentration and time of first arrival of ^{237}Np.

In Chapter 8, a new topic is dealt with. Turning our eyes from the far field, we look at near-field phenomena. We investigate in this chapter the effects of the geometry and molecular diffusion in the rock matrix parallel to the fracture plane. A cylindrical waste solid of infinite length is assumed to be intersected by a planar fracture. At the entire cylinder surface, solubility-limited concentration is maintained. The contaminant is release into the rock matrix as well as to the fracture. Two-dimensional diffusion in the fracture and three-dimensional diffusion in the rock matrix are assumed. The governing equations are established in the cylindrical geometry. The exact analytical solution for this problem has been first obtained by Chambré. The numerical evaluations are shown here.

For shorter-lived radionuclides, diffusion from the cylinder reaches the steady state faster. Because the fracture is assumed to conduct the contaminant faster than the rock matrix, mass flux from the cylinder into the rock matrix becomes less near the fracture. Although the mass flux into the fracture is much higher than into the rock matrix, the amout released into the rock matrix can be greater than that into the fracture, because of much larger surface area exposed to the rock matrix. If that is the case, the earlier mass-transfer theory [5] for a waste cylinder completely surrounded by porous rock is applicable.

Comparing the results from the planar-geometry model, considered in Chapter 2, the cylinder model gives greater mass flux into the fracture and deeper penetration into the fracture than the planar model, if molecular diffusion only is assumed in the fracture. In diffusion-dominant fractured media, the basic "bounding" model is no longer bounding, and the cylindrical geometry and the diffusion in the rock matrix parallel to the fracture plane must be assumed.

1.5 Recommendations for Further Studies

For the far-field transport, more attention should be paid to the fact that sorption and de-sorption are irreversible reactions. On de-sorption some of nuclides sorbed on the solid phase will remain in the solid phase, and never return to the water phase. Or, considering their low solubilities, actinides are very likely to form a precipitate in the medium. So far these are included in few studies of fracture transport [5][21].

For the matter of the near-field, we need to know the limitations of the assumptions such as an infinite cylinder and a pure diffusion field. By assuming them, we could avoid quite a lot of mathematical complexity. Yet, we need to test these assumptions. Especially for the latter, it is desired to know how advection in the fracture affects the mass transfer from the cylinder. With that, the current analysis becomes completed.

References

[1] Benedict, M., T. H. Pigford and H. Levi, *Nuclear Chemical Engineering,* Second ed., McGraw-Hill, New York, 1981,

[2] Long, J. C. S., *Verification and Characterization of Continuum Behaviour of Fractured Rock at AECL Underground Research Laboratory,* LBL-14975, Lawrence Berkeley Lab., 1985,

[3] Harada., M., P. L. Chambré, M. Foglia, K. Higashi, F. Iwamoto, D. Leung, T. H. Pigford, and D. Ting, *Migration of Radionuclides through Sorbing Media:*

Analytical Solutions—I, LBL-10500, Lawrence Berkeley Lab., 1980,

[4] Pigford, T. H., P. L. Chambré, M. Albert, M. Foglia, M. Harada, F. Iwamoto, T. Kanki, D. Leung, S. Masuda, S. Muraoka, and D. Ting, *Migration of Radionuclides through Sorbing Media: Analytical Solutions—II,* LBL-11616, Lawrence Berkeley Lab., 1980,

[5] Chambré, P. L., T. H. Pigford, A. Fujita, T. Kanki, A. Kobayashi, H. Lung, D. Ting, Y. Sato, and S. J. Zavoshy, *Analytical Performance Models for Geologic Repositories,* LBL-14842, Lawrence Berkeley Lab., 1982,

[6] Burkholder, H. C., M. O. Cloninger, D. A. Baker, and G. Jansen, Incentives for Partitioning High-Level Waste, *Nucl. Technol., 31,* 202, 1976,

[7] Neretnieks, I., Diffusion in the Rock Matrix: An Important Factor in Radionuclide Retardation?, *J. Geophys. Res., 85,* 4379, 1980,

[8] Birgersson, L., and I. Neretnieks, *Diffusion in the Matrix of Granitic Rock Field Test in the Stripa Mine. Part 1,* SKBF/KBS Teknisk Rapport, 82-08, Royal Inst. of Technol., Stockholm, Sweden, 1982,

[9] Birgersson, L., and I. Neretnieks, *Diffusion in the Matrix of Granitic Rock Field Test in the Stripa Mine. Part 2,* SKBF/KBS Teknisk Rapport, 83-39, Royal Inst. of Technol., Stockholm, Sweden, 1983,

[10] Abelin, H., I. Neretnieks, S. Tunbrant, and L. Moreno, *Final Report of the Migration in a Single Fracture—Experimental Results and Evaluation,* Stripa Project Tech. Report 85-03, Royal Inst. of Technol., Stockholm, Sweden, 1985,

[11] Hadermann, J., and A. Jakob, *Modelling Small Scale Infiltration Experiments into Bore Cores of Crystalline Rock and Break-Through Curves,* EIR-Bericht Nr. 622, Swiss Federal Inst. for Reactor Research, Würenlingen, Switzerland, 1987,

[12] Reeves, M., V. A. Kelley, and J. F. Pickens, *Regional Double-Porosity Solute Transport in the Culebra Dolomite: An Analysis of Parameter Sensitivity and Importance at the Waste Isolation Pilot Plant (WIPP) Site,* SAND87-7105,

Sandia National Lab., Albuquerque, New Mexico, 1987,

[13] Rasmuson, A., and I. Neretnieks, Migration of Radionuclides in Fissured Rock: The Influence of Micropore Diffusion and Longitudinal Dispersion, *J. Geophys. Res., 86,* 3746, 1981,

[14] Tang, D. H., E. O. Frind, and E. A. Sudicky, Contaminant Transport in Fractured Porous Media: Analytical Solution for a Single Fracture, *Water Resources Res., 17,* 555, 1981,

[15] Sudicky, E. A., and E. O. Frind, Contaminant Transport in Fractured Porous Media: Analytical Solution for a System of Parallel Fractures, *Water Resources Res., 18,* 1634, 1982,

[16] Sudicky, E. A., and E. O. Frind, Contaminant Transport in Fractured Porous Media: Analytical Solution for a Two-Member Decay Chain in a Single Fracture, *Water Resources Res., 20,* 2021, 1984,

[17] Matheron, G., and G. de Marsily, Is Transport in Porous Media Always Diffusive? A Counterexample, *Water Resources Res., 16,* 901, 1980,

[18] Ahn, J., A. Suzuki, R. Kiyose, Numerical Analysis of Nuclide Migration through Fissured Geological Media, *Nucl. Technol., 64,* 154, 1984,

[19] Grisak, G. E., and J. F. Pickens, Solute Transport through Fractured Media, I, The Effect of Matrix Diffusion, *Water Resources Res., 16,* 719, 1980,

[20] Rasmuson, A., T. Narasimhan, and I. Neretnieks, Chemical Transport in a Fractured Rock: Verification of a Numerical Model, *Water Resources Res., 18,* 1479, 1982,

[21] Neretnieks, I., Some Uses for Natural Analogues in Assessing the Function of HLW Repository, *Chemical Geology, 55,* 175, 1986.

Chapter 2
Migration of Radionuclide through a Single Fracture Surrounded by Rock Matrix of Infinite Extent

2.1 Introduction

This chapter establishes the formulation of radionuclide migration through a single, infinite, planar fracture surrounded by porous rock matrix of infinite extent, and shows the analytical solutions to (1) the space-time-dependent concentrations of radionuclide in the water both in the fracture and in the rock pores, (2) the space-time-dependent advective mass flux in the fracture, and (3) the space-time-dependent cumulative release in the fracture.

Analytical solutions are obtained for an arbitrary release mode, and then for a band release, whose definition is also given. The mathematical problem must be solved separately for the cases with zero or non-zero longitudinal dispersion in the fracture. Lateral dispersion will be considered in Chapter 7 with a multiple-patch source.

By numerical examples, several important observations such as retardation effect of matrix diffusion, back diffusion after the leach time, and effect of longitudinal dispersion are made. These observations and the assumptions made in the present model will be reconsidered in the following chapters.

2.2 Assumptions and Physical Processes

Consider a rock matrix containing multiple parallel planar fractures of width $2b$, situated in a water-saturated porous rock of porosity ε. Here the fractures are assumed to be widely separated so that each fracture can be assumed to be surrounded by infinite porous rock (See Figure 2.1). We consider (a) advective transport along the fracture with velocity v, (b) longitudinal hydrodynamic dispersion in the direction of the fracture axis in the fracture, with coefficient D, (c) molecular diffusion in the rock matrix, with coefficient

D_p, (d) sorption onto the fracture surfaces, (e) sorption in the rock matrix, and (f) radioactive decay without any precursors, with decay constant λ.

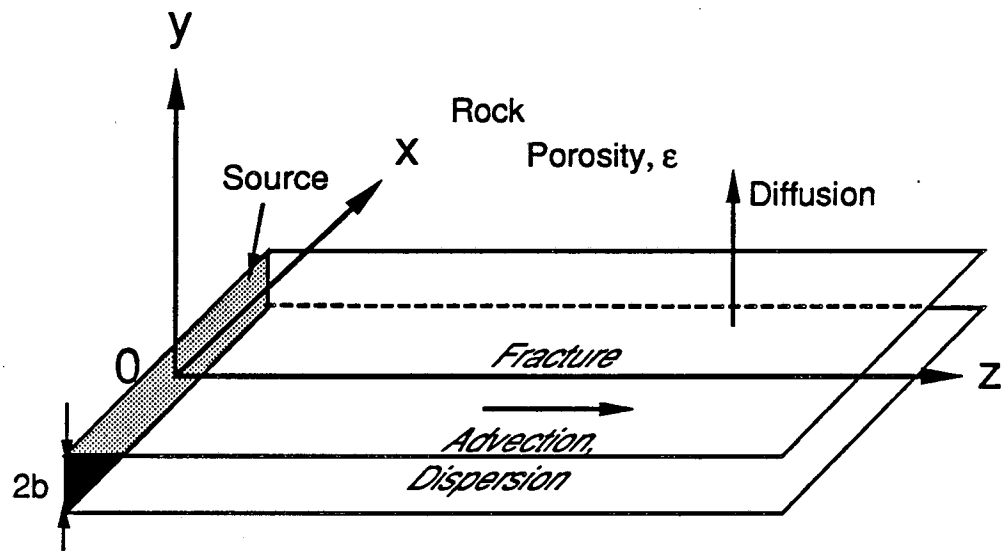

Figure 2.1 Geometry and physical processes considered in the model with a single, planar, infinite fracture.

In the fracture, water flow is assumed to be laminar, subject to Darcy's law. Resistive force due to shear stress acting on the rock-fracture interface results in a parabolic velocity profile across fracture width with the maximum velocity at the midplane in the fracture. To simplify, we average velocity over the width. Velocity is assumed to be constant with time and uniform in space. The fracture is assumed to contain no filling material, so pore velocity becomes identical to the Darcy velocity.

Longitudinal hydrodynamic dispersion is considered as combined effects of mechanical dispersion and molecular diffusion [1]. Mechanical dispersion occurs due to the roughness of the fracture walls and the parabolic velocity profile across the fracture width (Figure 2.2). Mechanical dispersion is caused also by channeling effect in the fracture [2]. In reality the both fracture-walls contact with each other at various points, so there would be multiple paths of water flow between the source location and the observation point in the same fracture. These water-flow paths would have different length, sorption properties,

and roughness, resulting in different arrival times.

Longitudinal hydrodynamic dispersion can be mathematically treated in several ways. One of the most common ways is to treat it as a diffusion-like process; dispersive flux of the contaminant is assumed to be proportional to the concentration gradient. This is not necessarily true. Because dispersion is a macroscopic view of movement of many contaminant particles, it takes some distance away from the contaminant source to average movement of contaminant particles, and in some cases, it is never possible to model dispersion by a diffusion-like process [3] [4].

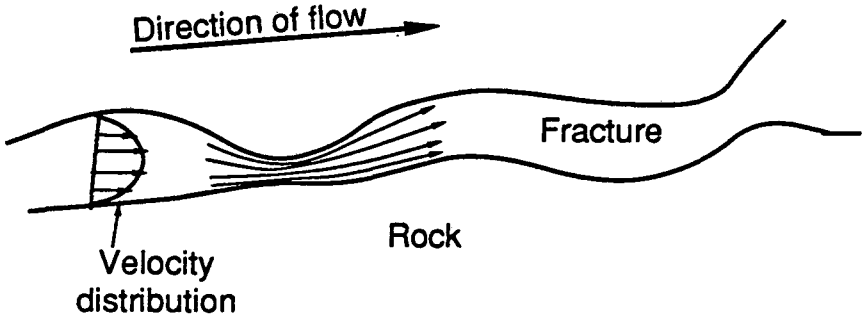

(a) Illustration of mechanical dispersion due to a parabolic velocity profile and surface roughness

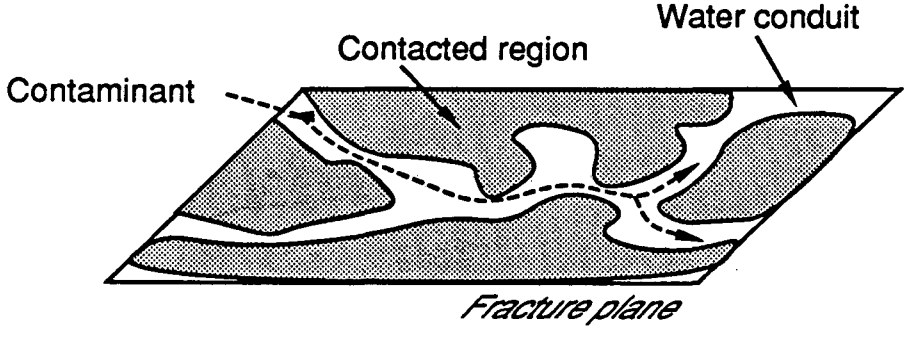

(b) Illustration of channeling of water conduits in a fracture

Figure 2.2 Spreading due to mechanical dispersion in a fracture

Other researchers apply channeling dispersion as the principal mechanism for hydrodynamic dispersion. In this treatment multiple paths are considered to exist between

the source and the observation point. Due to different properties of each path, the effluent concentration from one channel at the observation point differs from concentrations from other channels, resulting in dispersion of the contaminant. It is assumed in *Moreno, Neretnieks, and Eriksen* [2] that the fracture widths have a lognormal distribution and the interconnection between the different channels is negligible. The concentration at the observation point is then obtained by averaging effluent concentrations from all channels, assuming the lognormal distribution. In other cases, the channeling dispersion model is used to obtain the property of paths which are observed ocularly in actual fractures by curve fitting against field measurements [5]. To analyze field measurements, however, the channeling model has so many degrees of freedom that one can always obtain a very good "best-fit" curve.

We assume in the present study that longitudinal dispersion can be expressed as a diffusion-like process with a constant coefficient D, for mathematical simplicity. A constant longitudinal dispersion coefficient independent of the distance from the source may be true for a large-distance region where the water in different fractures has been repeatedly mixed. For a medium where only few of fractures intersect each other, an advection-dispersion model with constant longitudinal dispersion may not be a good description.

The diffusion coefficient in the rock matrix D_p includes the effect of matrix tortuosity. Because diffusion is constrained in a tortuous path in porous rock, the diffusion coefficient becomes smaller than that in unconstrained water. The diffusion coefficient of a species of low molecular weight (less than 500) in unconstrained water at ambient temperature is $D_v \approx 0.05 \sim 0.15$ m^2/yr [6]. In porous rock this value is reduced by a factor τ:

$$D_p = \tau D_v \qquad (2.1)$$

The factor τ depends on porosity of rock, pressure applied on rock, and temperature. Some experimental data on various rock types show that τ ranges from 0.01 to 0.3 [7].

Interactions of radionuclides with the solid phase are another uncertain factor. Possible interactions are sorption, precipitation, mineralization, diffusion into the solid phase and so on. In the last three interactions, radionuclides might not return to the water phase again. If these occur, the performance of a geologic disposal system will improve. We assume local chemical equilibrium between the water and the solid phases. Sorption is assumed to be a reversible reaction with a constant distribution coefficient. Sorption onto the fracture walls and sorption within the rock matrix are considered separately because of the possibility of differing chemical properties in the matrix and in the fracture.

2.3 Formulation of Problem

We make the following assumptions relating to the geometry and hydraulic properties of the system:

(1) The fracture aperture, $2b$, is much smaller than the scale considered in the z-direction,

(2) Diffusion and dispersion across the fracture aperture assure complete mixing,

(3) The permeability of the porous rock is very low and transport in the rock will be mainly by molecular diffusion,

(4) Transport along the fracture is much faster than transport in the rock, and

(5) The contaminant source at the fracture entrance is uniformly distributed over the y-direction.

By assumptions (1), (2) and (5), mass transport along the fracture can be represented in a one-dimensional rectangular coordinate. Assumptions (3) and (4) allow us to take the direction of mass flux in the rock matrix to be perpendicular to the fracture plane. We can simplify the basically two-dimensional system into two orthogonal one-dimensional systems: one for the concentration in water in the fracture and one for the concentration in water in the rock pores. The coupling of two one-dimensional systems is provided by the continuity of fluxes and concentrations along the rock/fracture interface.

The differential equation for the concentration in the water in the fracture can be

obtained by balancing the total mass of the radionuclide in the fracture:

$$\frac{\partial N}{\partial t} + v\frac{\partial N}{\partial z} - D\frac{\partial^2 N}{\partial z^2} + \lambda N + \frac{q}{b} + \frac{r_f}{b} = 0, \quad t > 0, \; z > 0. \qquad (2.2)$$

where

$r_f(z, t)$: soprtion rate from fracture water to fracture surfaces [kg-nuclide/m^2·yr],

$q(z, t)$: diffusive flux from fracture water into rock matrix [kg-nuclide/m^2·yr],

$N(z, t)$: concentration of radionuclide in water in fracture [kg-nuclide/m^3],

b : half fracture-aperture [m],

v : water velocity in the fracture [m/yr],

z : distance along the fracture from the source [m], and

t : time [yr].

Denoting the concentration of sorbed contaminant on the fracture surface as $N_s(z, t)$ [kg-nuclide/m^2-surface] and neglecting surface diffusion, the following rate equation applies:

$$\frac{\partial N_s}{\partial t} + \lambda N_s - r_f = 0, \qquad t > 0, \; z > 0. \qquad (2.3)$$

If we assume that mass transfer of nuclide between fracture water and fracture surface is so rapid that the concentration of nuclide on fracture surface becomes instantaneously in local equilibirum with that of nuclide in fracture water, and that a linear sorption isotherm applies, then we can write the relation:

$$N_s = K_f N \qquad (2.4)$$

where K_f is the sorption distribution coefficient [m]. Substituting (2.4) into (2.3) and cancelling the r_f terms both in the resultant equation and (2.2) yields the equation for the concentration in the water in the fracture as:

$$R_f\frac{\partial N}{\partial t} + v\frac{\partial N}{\partial z} - D\frac{\partial^2 N}{\partial z^2} + R_f\lambda N + \frac{q}{b} = 0, \quad z > 0, \; t > 0, \qquad (2.5)$$

where R_f is retardation factor for in-fracture transport, and is defined as:

$$R_f = 1 + \frac{K_f}{b}. \qquad (2.6)$$

Transport processes in the fracture, such as advection and dispersion, are apparently retarded by the factor of R_f. For the case of no sorption ($K_f = 0$) the factor becomes unity, and the nuclide is transported at the same speed of the water in the fracture. If the fracture width becomes small, the factor becomes large.

On the other hand, the governing equations for the nuclide in the rock matrix can be written by considering one-dimensional molecular diffusion in the pore water, radioactive decay, and sorption from the pore water to pore surfaces and by neglecting surface diffusion:

$$\varepsilon \frac{\partial M}{\partial t} - \varepsilon D_p \frac{\partial^2 M}{\partial y^2} + \varepsilon \lambda M + a_p r_p = 0, \quad y > b, t > 0, \qquad (2.6)$$

and

$$a_p \frac{\partial M_s}{\partial t} + a_p \lambda M_s - a_p r_p = 0, \quad t > 0, \qquad (2.7)$$

where (2.6) is for the water phase and (2.7) for the sorbed phase, and where

$M(y, z, t)$: concentration of radionuclide in water in rock pores [kg/m^3],

$M_s(y, z, t)$: concentration of radionuclide on pore surfaces [kg/m^2],

ε : porosity of rock excluding the pores which are not connected to the fracture,

a_p: pore surface area per unit volume of rock matrix, which are connected to the fracture [m^2-surface/m^3-rock], and

r_p : rate of sorption from pore water onto pore surfaces [kg/m^2·yr].

Assuming the instantaneous local equilibrium between the pore water and the pore surfaces and a linear sorption isotherm,

$$M_s = K_p M, \qquad (2.8)$$

where K_p is the sorption distribution coefficient [m], we can obtain the governing equation

for $M(y, z, t)$ from (2.6), (2.7), and (2.8) as

$$R_p \frac{\partial M}{\partial t} - D_p \frac{\partial^2 M}{\partial y^2} + R_p \lambda M = 0, \quad y > b, z > 0, t > 0, \tag{2.9}$$

where R_p is retardation factor for transport in rock matrix, and is defined as:

$$R_p = 1 + \frac{a_p}{\varepsilon} K_p . \tag{2.10}$$

Equations (2.5) and (2.9) are the governing equations to be solved. The rate of diffusion from the fracture to the rock matrix, $q(z, t)$, in (2.5) can be defined by using $M(y, z, t)$ as:

$$q(z, t) = - \varepsilon D_p \left. \frac{\partial M}{\partial y} \right|_{y=b}, \quad z > 0, t > 0. \tag{2.11}$$

We solve (2.5) and (2.9), which are coupled by (2.11), subject to the following side conditions:

$$N(z, 0) = 0, \ z > 0, \tag{2.12}$$

$$M(y, z, 0) = 0, \quad y > b, \quad z > 0, \tag{2.13}$$

$$N(0, t) = \psi(t), \quad t > 0, \tag{2.14}$$

$$N(0, \infty) = 0, \quad t > 0, \tag{2.15}$$

$$M(b, z, t) = N(z, t), \quad z > 0, t > 0, \tag{2.16}$$

$$M(\infty, z, t) = 0, \ z > 0, \ t > 0. \tag{2.17}$$

A prescribed function $\psi(t)$ in (2.14) represents the time-dependency of the concentration at the fracture entrance, and is determined by considering how the radionuclide is released from the waste source. $\psi(t)$ is any integrable function. Equation (2.16) is the other coupling of the two governing equations, representing the continuity of concentration at the rock/fracture interface.

In addition to the concentrations, $N(z, t)$ and $M(y, z, t)$, we will derive the following auxiliary quantities:

$$j(z, t) \equiv vN(z, t) - D \frac{\partial N}{\partial z}, \quad t > 0, \; z \geq 0, \tag{2.18}$$

$$J(z, t) \equiv \int_0^t j(z, \tau)\, d\tau, \quad t > 0, z \geq 0, \tag{2.19}$$

where

$j(z, t)$: the advective mass flux of the radionuclide at position z in the fracture, and

$J(z, t)$: the time-dependent cumulative release of the radionuclide across a plane at z, and normal to z, in the fracture.

2.4 Solutions to General Release Mode

The analytical solutions to (2.5) and (2.9) subject to the side conditions, (2.12) to (2.17) can be obtained by applying Laplace transform with respect to t. We must solve the case of zero dispersion in the fracture separately because (2.5) becomes the first-order partial differential equation. Derivation of the analytical solutions is shown in the following for the case of non-zero dispersion. Because solution procedure is quite similar, all of the steps for the case of zero dispersion are not shown.

By Laplace transform of (2.9) with the aid of the initial condition (2.13), we obtain:

$$p\tilde{M} = \frac{D_p}{R_p} \frac{d^2\tilde{M}}{dy^2} - \lambda\tilde{M}, \quad y > b, \tag{2.20}$$

where the tilde ~ stands for the Laplace-transformed variable and p is a Laplace variable, complex. (2.20) is solved with the Laplace-transformed boundary conditions,

$$\tilde{M}(b, z, p) = \tilde{N}(z, p), \quad z > 0, \tag{2.16a}$$

$$\tilde{M}(\infty, z, p) = 0, \quad z > 0. \tag{2.17a}$$

The solution to (2.20), then, can be written as:

$$\tilde{M}(y, z, p) = \tilde{N}(z, p)\, e^{-B(y-b)\sqrt{p+\lambda}}, \; z > 0, \quad y > b, \tag{2.21}$$

where

$$B = \sqrt{\frac{R_p}{D_p}} . \qquad (2.22)$$

The Laplace-transformed flux across the rock-fracture interface, can be calculated from (2.21) as

$$\tilde{q}(z,p) = -\varepsilon D_p \left.\frac{d\tilde{M}}{dy}\right|_{y=b} = \varepsilon D_p B \sqrt{p+\lambda}\,\tilde{N}(z,p). \qquad (2.23)$$

Applying Laplace transform to (2.5) and substituting (2.23) into the resultant equation yields, for $D \neq 0$,

$$\frac{d^2\tilde{N}}{dz^2} - \frac{v}{D}\frac{d\tilde{N}}{dz} - \frac{R_f}{D}\left(p+\lambda+\frac{\sqrt{p+\lambda}}{A}\right)\tilde{N} = 0, \quad z>0, \qquad (2.24)$$

where

$$A \equiv \frac{b R_f}{\varepsilon\sqrt{D_p R_p}} .$$

If D is zero, then we have

$$\frac{d\tilde{N}}{dz} + \frac{R_f}{v}\left(p+\lambda+\frac{\sqrt{p+\lambda}}{A}\right)\tilde{N} = 0, \quad z>0. \qquad (2.24')$$

(2.24) or (2.24') should be solved with the Laplace-transformed boundary conditions:

$$\tilde{N}(0,p) = \tilde{\psi}(p), \qquad (2.14a)$$

$$\tilde{N}(\infty,p) = 0. \qquad (2.15a)$$

For (2.24) and (2.24'), we obtain:

$$\tilde{N}(z,p) = \tilde{\psi}(p)\, e^{\alpha z} exp\left[-\alpha z\sqrt{1+\beta^2\left(p+\lambda+\frac{\sqrt{p+\lambda}}{A}\right)}\right], \; z \geq 0, D \neq 0, \qquad (2.25)$$

$$\tilde{N}(z,p) = \tilde{\psi}(p)\, exp\left[-\frac{z R_f}{v}\left(p+\lambda+\frac{\sqrt{p+\lambda}}{A}\right)\right], \quad z \geq 0,\ D = 0, \qquad (2.25')$$

where

$$\alpha = \frac{v}{2D} \quad and \quad \beta^2 = \frac{4R_f D}{v^2}\ . \qquad (2.26)\ and\ (2.27)$$

We will show the steps to the solution for $D \neq 0$ below. In order to avoid the difficulty of the double square root in (2.25), we apply the formula [8]:

$$\int_0^\infty e^{-\xi^2 - \frac{X^2}{\xi^2}} d\xi = \frac{\sqrt{\pi}}{2} e^{-2X}, \quad X > 0, \qquad (2.28)$$

obtaining from (2.25):

$$\tilde{N}(z,p) = e^{\alpha z}\frac{2}{\sqrt{\pi}}\int_0^\infty e^{-\xi^2 - \frac{\alpha^2 z^2}{4\xi^2}} \tilde{\psi}(p)\, exp\left[-Y\sqrt{p+\lambda} - YA(p+\lambda)\right] d\xi,$$

$$z \geq 0, \qquad (2.29)$$

where

$$Y \equiv \frac{\alpha^2 \beta^2 z^2}{4A\xi^2}\ . \qquad (2.30)$$

Substituting (2.29) into (2.21) gives the Laplace-transformed concentration in the rock matrix as:

$$\tilde{M}(y,z,p) = e^{\alpha z}\frac{2}{\sqrt{\pi}}\int_0^\infty e^{-\xi^2 - \frac{\alpha^2 z^2}{4\xi^2}} \tilde{\psi}(p)\, exp\left[-\{Y+B(y-b)\}\sqrt{p+\lambda} - YA(p+\lambda)\right] d\xi,$$

$$y \geq b,\ z \geq 0. \qquad (2.31)$$

(2.29) and (2.31) can be inverted by using the shift property of Laplace transform [9],

$$\mathcal{L}^{-1}\left[\tilde{\Phi}(p)\, e^{-pE}\right] = \Phi(t-E)\, h(t-E), \quad E > 0, \qquad (2.32)$$

and the following formula [8]:

$$\mathcal{L}^{-1}\left[e^{-k\sqrt{p}}\right] = \begin{cases} \dfrac{k}{2\sqrt{\pi t^3}}\, e^{-\frac{k^2}{4t}}, & k > 0, \\ \delta(t), & k = 0, \end{cases} \tag{2.33}$$

where $\mathcal{L}^{-1}[\cdot]$ stands for the inverse Laplace transform, and $h(\cdot)$ for Heaviside step function. We extend the range of k in (2.33) to include zero. This extension is reasonable because if $k \to 0$ for $t > 0$, then the inverse vanishes, while if $k \to 0$ with $t \to 0$, then the inverse blows up. The solutions are obtained as follows:

$$N(z, t) = \frac{2}{\sqrt{\pi}}\, e^{\alpha z} \int_g^\infty G(\xi; z, t)\, e^{-\lambda YA} \int_0^{t-YA} \psi(t - YA - t')\, E(t'; Y) dt'\, d\xi,$$

$$z \geq 0,\ t \geq 0, \tag{2.34}$$

and

$$M(y, z, t) = \frac{2}{\sqrt{\pi}}\, e^{\alpha z} \int_g^\infty G(\xi; z, t)\, e^{-\lambda YA} \int_0^{t-YA} \psi(t - YA - t')\, E(t'; Y + B(y-b)) dt' d\xi,$$

$$y \geq b,\ z > 0,\ t \geq 0, \tag{2.35}$$

where

$$G(\xi; z, t) \equiv e^{-\xi^2 - \frac{\alpha^2 z^2}{4\xi^2}}, \qquad g = \frac{z}{2}\sqrt{\frac{R_f}{Dt}}, \tag{2.36}$$

and

$$E(t'; k) = \begin{cases} \dfrac{k}{2\sqrt{\pi t'^3}}\, e^{-\frac{k^2}{4t'} - \lambda t'}, & k > 0, \\ \delta(t'), & k = 0, \end{cases} \tag{2.37}$$

Equations (2.34) and (2.35) are the solutions to the governing equations (2.5) and (2.9) subject to (2.12) to (2.17).

The advective mass flux, $j(z, t)$, and the cumulative release, $J(z, t)$, can be obtained from the definitions (2.18) and (2.19) as, using the expression for $N(z, t)$, (2.34):

$$j(z,t) = \frac{e^{\alpha z}}{\sqrt{\pi}} \int_g^{\infty} G(\xi; z, t)\, e^{-\lambda YA} \int_0^{t-YA} \psi(t - YA - t')\, E(t'; Y)\, H(t', \xi; z)\, dt' d\xi,$$

$$t > 0,\ z \geq 0, \tag{2.38}$$

and

$$J(z,t) = \frac{e^{\alpha z}}{\sqrt{\pi}} \int_g^{\infty} G(\xi; z, t)\, e^{-\lambda YA} \int_0^{t-YA} \int_0^{t-YA-t'} \psi(\tau) d\tau \cdot E(t'; Y)\, H(t', \xi; z)\, dt' d\xi,$$

$$t > 0, \quad z \geq 0, \tag{2.39}$$

where

$$H(t', \xi; z) \equiv \nu \left(1 + \frac{\alpha z}{2\xi^2}\right) + \frac{R_f z}{2\xi^2} \left\{ \left(\frac{Y^2}{2t'} + \frac{Y}{A} - 3 \right) \frac{1}{t'} - \frac{2}{YA} \right\}. \tag{2.40}$$

For the case of zero dispersion, we can obtain the analytical solutions in the very similar way shown above, obtaining:

$$N(z,t) = e^{-\lambda ZA}\, h(t - ZA) \int_0^{t-ZA} \psi(t - ZA - t')\, E(t'; Z)\, dt', \quad z \geq 0,\ t \geq 0, \tag{2.41}$$

$$M(y,z,t) = e^{-\lambda ZA} h(t - ZA) \int_0^{t-ZA} \psi(t - ZA - t')\, E(t'; Z + B(y-b))\, dt',\ y \geq b,\ z > 0,\ t \geq 0, \tag{2.42}$$

$$j(z,t) = \nu N(z,t), \quad z \geq 0,\ t \geq 0, \tag{2.43}$$

$$J(z,t) = \nu\, e^{-\lambda ZA} h(t - ZA) \int_0^{t-ZA} \int_0^{t-ZA-t'} \psi(\tau) d\tau \cdot E(t'; Z)\, dt', \quad z \geq 0,\ t \geq 0, \tag{2.45}$$

where

$$Z \equiv \frac{R_f z}{\nu A} \tag{2.45}$$

2.5 Solutions to Band Release

2.5.1 Definition of Band Release

To illustrate fracture-flow transport, we introduce a band release for the nuclide release mode at the fracture entrance. We follow the definition of a band release given in [10], and give the fracture-transport version of the definition hereafter.

For a band release, we must assume that:

(1) A constant amount of the total waste material dissolves into ground-water in the fracture per unit time,

(2) All of the waste material begins to dissolve at $t = 0$. Dissolution is complete within a leach time T,

(3) All radionuclides contained within the waste material go into the water phase at the dissolution location when the waste matrix dissolves, i.e., all nuclides dissolve congruently with the waste matrix, and

(4) The effect of dispersion at $z = 0$ is neglected.

A "band release" comes from assumption (2).

Suppose the initial amount W^o of the total waste material is available per unit area of the fracture opening at $z = 0$. The rate of dissolution $\dot{M}_T$ of the total waste material is, because of assumptions (1) and (2),

$$\dot{M}_T = \frac{W^o\ [kg/m^2]}{T\ [yr]} \quad for\ 0 \le t \le T. \tag{2.46}$$

If water flows at velocity v past the waste material, the concentration $N_i(t)$ of a dissolved radionuclide i at the dissolution location ($z = 0$) is given by, because of assumption (4),

$$N_i(t) = \frac{\dot{M}_T\ [kg/m^2] \cdot 1\ [m^2]}{v\ [m/yr] \cdot 1\ [m^2] \cdot T\ [yr]}\ n_i(t), \quad 0 \le t \le T, \tag{2.47}$$

where $n_i(t)$ is the amount of nuclide i per unit amount of waste material. In the denominator, $v \cdot 1$ gives the volumetric flow rate past the unit cross-sectional area of the waste

material exposed to the fracture opening. Since we assume that the radionuclide has no precursor, we may write $n_i(t)$ as

$$n_i(t) = n_i^o e^{-\lambda_i t}, \qquad (2.48)$$

where n_i^o is the initial fraction of nuclide i in the total waste material. Because we are interested in a single radionuclide with no decaying mother, we can omit subscript i without confusion. Thus, the time-dependent concentration $N(t)$ in the water phase at the dissolution point ($z = 0$) is given by, because of assumption (3),

$$N(t) = N^o e^{-\lambda t} \{h(t) - h(t - T)\}, \qquad (2.49)$$

where N^o is the initial concentration in the water phase at the dissolution point and is given by

$$N^o = \frac{\dot{M}_T}{vT} n^o \qquad (2.50)$$

The concentration $N(t)$ are the real concentration $N(0, t)$ at the boundary *only* if assumption (4) holds. Equation (2.49) is depicted in Figure 2.3. We will use (2.49) for $\psi(t)$ in the next section.

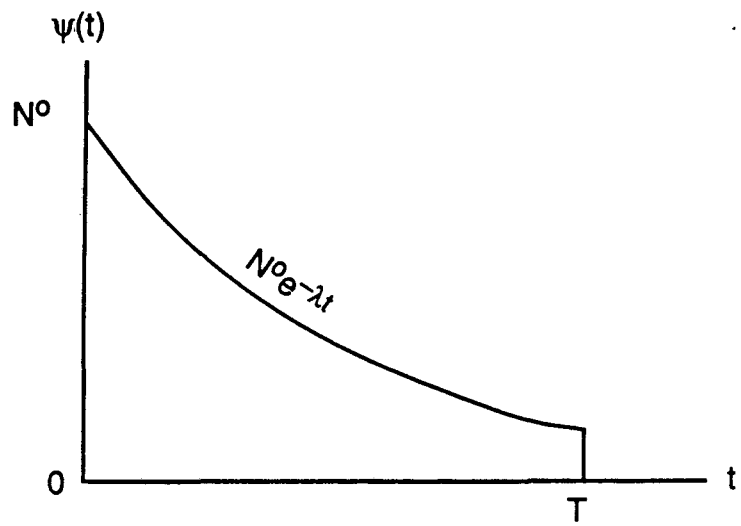

Figure 2.3 Concentration profile at the inlet boundary of the fracture for a band release. Nuclide release continues for a period of a leach time, T

2.5.2 Solutions to Band Release

By substituting (2.49) into function $\psi(t)$ in the analytical solutions obtained in Section 2.4, we can obtain the analytical solutions for the case of a band release as follows:

For non-zero dispersion:

$$N(z, t)/N^o = F_1(b, z, t) - e^{-\lambda T} F_1(b, z, t-T), \quad t \geq 0, \ z \geq 0, \tag{2.51}$$

$$M(y, z, t)/N^o = F_1(y, z, t) - e^{-\lambda T} F_1(y, z, t-T), \quad t \geq 0, \ y \geq b, z > 0, \tag{2.52}$$

$$j(z, t)/N^o = F_2(z, t) - e^{-\lambda T} F_2(z, t-T), \quad t > 0, \ z \geq 0, \tag{2.53}$$

$$J(z, t)/N^o = F_3(z, t) - e^{-\lambda T} F_3(z, t-T), \quad t > 0, \ z \geq 0, \tag{2.54}$$

where

$$F_1(y, z, t) = \frac{2}{\pi} e^{\alpha z} \int_g^\infty G(\xi; z, t)\, e^{-\lambda t} erfc\left(\frac{Y + B(y-b)}{2\sqrt{t - YA}}\right) d\xi, \tag{2.55}$$

$$F_2(z, t) = \frac{e^{\alpha z}}{\pi} \int_g^\infty G(\xi; z, t)\, e^{-\lambda t}\, Q(\xi; 0, z, t)\, d\xi \tag{2.56}$$

$$F_3(z, t) = \frac{-1}{\lambda} F_2(z, t) + \frac{e^{\alpha z}}{\lambda \pi} \int_g^\infty G(\xi; z, t)\, e^{-\lambda YA}\, Q(\xi; \lambda, z, t)\, d\xi, \tag{2.57}$$

$$Q(\xi; k, z, t) \equiv \frac{v\sqrt{\pi}}{2}\left(1 + \frac{\alpha z}{2\xi^2} + \frac{R_f z}{\xi^2 v} k\right) P_+(k, Y, t) + \frac{R_f z}{2\xi^2} \frac{2t - YA}{A\sqrt{(t - YA)^3}} \times$$

$$exp\left\{-\frac{Y^2}{4(t - YA)} - k(t - YA)\right\} + \frac{R_f z}{2\xi^2 A} \sqrt{k\pi}\, P_-(k, Y, t), \tag{2.58}$$

$$P_\pm(k, Y, t) \equiv \pm e^{Y\sqrt{k}}\, erfc\left(\frac{Y}{2\sqrt{t - YA}} + \sqrt{k(t - YA)}\right) +$$

$$+ e^{-Y\sqrt{k}}\, erfc\left(\frac{Y}{2\sqrt{t - YA}} - \sqrt{k(t - YA)}\right), \tag{2.59}$$

For zero dispersion:

$$N(z, t)/N^o = F_4(b, z, t) - e^{-\lambda T} F_4(b, z, t-T),\ t \geq 0, z \geq 0, \qquad (2.60)$$

$$M(y, z, t)/N^o = F_4(y, z, t) - e^{-\lambda T} F_4(y, z, t-T), y \geq b,\ z > 0,\ t \geq 0, \qquad (2.61)$$

$$j(z, t)/N^o = v\ \frac{N(z, t)}{N^o}\ ,\quad t \geq 0,\ z \geq 0, \qquad (2.62)$$

$$J(z, t)/N^o = F_5(z, t) - e^{-\lambda T} F_5(z, t),\quad t \geq 0,\ z \geq 0, \qquad (2.63)$$

where

$$F_4(y, z, t) \equiv h(t - ZA)\, e^{-\lambda t}\, erfc\left(\frac{Z + B(y-b)}{2\sqrt{t - ZA}}\right), \text{ and} \qquad (2.64)$$

$$F_5(z, t) \equiv \frac{v}{\lambda} h(t - ZA) \left\{ \frac{e^{-\lambda ZA}}{2} P_+(\lambda, Z, t) - e^{-\lambda t}\, erfc\left(\frac{Z}{2\sqrt{t - ZA}}\right)\right\}. \qquad (2.65)$$

2.6 Numerical Illustrations

2.6.1 Description on Computer Codes

Analytical solutions (2.51) to (2.54) and (2.60) to (2.63) are implemented into computer programs written in FORTRAN 77. For non-zero dispersion cases, integrations with respect to ξ in (2.55), (2.56) and (2.57) must be evaluated numerically. We first introduce a variable transformation:

$$\xi = \frac{z}{2}\sqrt{\frac{R_f}{Dt}}\,\frac{1}{\mu}, \qquad (2.66)$$

so that the integration interval is changed from $\frac{z}{2}\sqrt{\frac{R_f}{Dt}} \leq \xi < \infty$ to $0 \leq \mu \leq 1$.

The term, $exp(\alpha z)$, in functions $F_1(y, z, t)$, $F_2(z, t)$, and $F_3(z, t)$ causes computer overflow for large z. To avoid overflow, we combine this exponential term with the exponential term in $G(\xi; z, t)$ as

$$e^{\alpha z} G(\xi; z, t) = e^{\alpha z} e^{-\xi^2 - \frac{\alpha^2 \zeta^2}{4\xi^2}} = exp\left\{ -\left(\alpha\mu \sqrt{\frac{Dt}{R_f}} - \frac{z}{2} \sqrt{\frac{R_f}{Dt}} \frac{1}{\mu} \right)^2 \right\}. \quad (2.67)$$

After these preparations, we adopt Gaussian quadratures for numerical integration. Each of the integrands has a sharp peak in the integration interval, $\mu \in [0, 1]$; the integrands become less than the computer underflow limit in most of the interval. We must determine the effective interval inside [0, 1], where the integrands exceed the computer underflow limit, by checking the magnitude of the exponential term, (2.67), and of the complimentary error functions in (2.55) or in $Q(\xi; k, z, t)$, (2.58). The effective interval becomes smaller for larger times.

Numerical integration was performed by the package subroutine D01AJF of NAG library [11]. The relative error of the numerical integration was set to be less than 10^{-6}.

2.6.2 Input Data

Numerical results are shown for ^{237}Np in Figures 2.4 to 2.8. There are significant uncertainties in determining input parameter values. One of the uncertainties comes from the fact that every parameter value has its distribution. For example, it is observed that fracture width shows a lognormal distribution [12]. Uncertainties arise also in measurement of parameter values. For example, because actual fractures are not perfect planar planes, we must introduce some kind of average width for the present model. There are several ways to measure average widths: by compressing a rock sample containing fractures and observing the volume change with the applied pressure [13–15], or by calculating the width from measured permeability of fractures based on the cubic law [5]. The results obtained by these methods, however, usually show large discrepancy even for the same rock sample.

One way to avoid the complexity, keeping the argument still useful, is to take conservative values. For example, if we take a large value for the fracture width, the

contaminant will be transported faster, which could be a worst-case prediction. Parameter values for water velocity v, fracture width $2b$, and in-fracture retardation factor R_f, shown in the following graphs, were chosen so that the considered cases become reasonably conservative.

The diffusion coefficient in the rock matrix is reletively well determined based on (2.1). We choose $D_p = 0.01$ m^2/yr for illustration.

We use $D = 1$ m^2/yr for the longitudinal dispersion coefficient in the following examples. This value is found to be in the range of values obtained from some tracer experiments in fractured crystalline rocks [16]. Because we have assigned a relatively large value for velocity, we cannot immediately judge the importance of longitudinal dispersion in the following numerical examples. We investigate the importance of longitudinal dispersion in the context of Pechlet number in the next chapter.

2.6.3 Numerical Results

In Figures 2.4 to 2.6, actually two cases are compared: $D = 0$ and $D = 1$ m^2/yr. However, these two cases give so close results in many cases.

In Figure 2.4, plotted are the normalized concentration in the fracture as a function of distance along the fracture, at times 10,000 yr and 50,000 yr for three sets of pore retardation factors. Solid lines stand for the case of 10,000 yr and dashed lines for the case of 50,000 yr. Because the leach time is assumed to be 30,000 yr, these two cases represent the cases before and after the leach time, respectively. For each time three curves are plotted for different R_p values.

Let us look at the three curves for 10,000 yr. The rightmost curve represents the case without any sorption in the fracture or in the rock matrix, and shows, though, that the front edge of the contaminant moves more slowly than water flows. Because water velocity is 10 m/yr, the contaminant front should reach 10^5 m by 10,000 yr. Due to

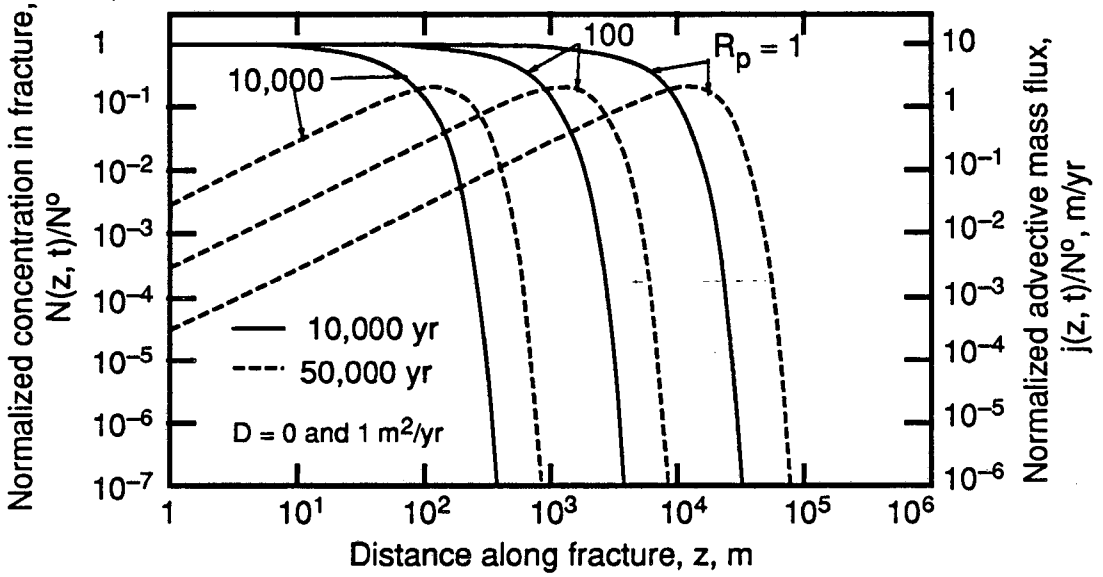

Figure 2.4 Profiles of normalized concentrations and advective mass fluxes in the fracture for a band release. Curves are for v = 10 m/yr, $2b$ = 0.01 m, ε = 0.01, R_f = 1, D_p = 0.01 m²/yr, T = 30,000 yr. Difference between D = 0 and D = 1 m²/yr is so slight that curves for these two cases cannot be distinguished. ^{237}Np is assumed.

diffusion into rock matrix, some of the contaminant in the fracture is taken away, resulting in rapid decrease in concentration in the fracture. The rest of the solid curves show the effect of pore retardation in addition to retardation due to matrix diffusion. As the pore retardation factor increases, diffusion into matrix becomes apparently slower, and penetration into rock matrix is shallower (See also Figure 2.6). As a result, the concentration gradient at the rock/fracture interface becomes steeper (See Figure 2.7(a)), and so more nuclide is taken away from the fracture.

At 50,000 yr, the source at z = 0 no longer emits radionuclide, and uncontaminated water enters the fracture. This causes reversing the direction of diffusion flux in the rock matrix (See Figure 2.7(b)); in the region near the fracture entrance the contaminant diffuses from rock matrix to the fracture again. We call this "back diffusion." Notice that due to back diffusion the contaminant exists near the fracture entrance even after the leach time. We will investigate the back diffusion in detail in Chapter 4.

Because the effect of longitudinal dispersion is so slight, the advective mass flux in

the fracture, $j(z, t)$, normalized by the initial boundary concentration N^o is proportional to $N(z, t)$ by a factor of velocity v.

In Figures 2.5(a) and (b), plotted are the cumulative release of the contaminant for $D = 0$ and $D = 1$ m^2/yr. Again the effect of longitudinal dispersion is so slight, but in early times we see slight difference. Figure 2.5(a) shows the profiles against the distance along the fracture at 10,000 yr and 50,000 yr. Almost all the contaminant released during the leach time T has passed the region near the fracture entrance by 50,000 yr because, if one sets $z = 0$ and $t > T$ in (2.63), one can get the total amount of the contaminant released into the fracture from unit cross-sectional area of the source as:

$$\frac{J(0, t > T)}{N^o} = \frac{v}{\lambda}\left\{1 - e^{-\lambda t}\right\} - \frac{v}{\lambda}e^{-\lambda T}\left\{1 - e^{-\lambda(t-T)}\right\} = \frac{v}{\lambda}\left(1 - e^{-\lambda T}\right) \approx vT$$

$$= 3 \times 10^5 [m] \qquad (2.68)$$

Notice that in the small-z region the cumulative release is nearly equal to, but slightly less than 3×10^5 m at 50,000 yr. On comparison of three dashed curves, more nuclide is transported in the fracture for smaller pore retardation factors. The difference between the curves for large and small pore retardations is kept in rock matrix as a sorbed phase.

At every point of z in the fracture the cumulative release reaches the maximum as time goes to infinity. The maximum at point z in the fracture can be calculated for the $D = 0$ case from (2.63) as:

$$\lim_{t \to \infty} J(z, t)/N^o = \frac{v}{\lambda}\left(1 - e^{-\lambda T}\right) e^{-\lambda ZA - \sqrt{\lambda}\, Z}, \quad z \geq 0, \qquad (2.69)$$

The right-hand side of (2.69) is smaller than (2.68) because of the loss by radioactive decay during transport from the origin to point z. Figure 2.5(b) depicts the change of the cumulative release with time at $z = 10^2$, 10^4, 10^6, and 10^7 m. The maximum value for each location is obtained from (2.69) as 2.98×10^5, 2.66×10^5, 9.53×10^4, and 3.29 m, respectively. Thus, we can say for ^{237}Np that most of the contaminant decays out before it reaches the point of 10^7 m.

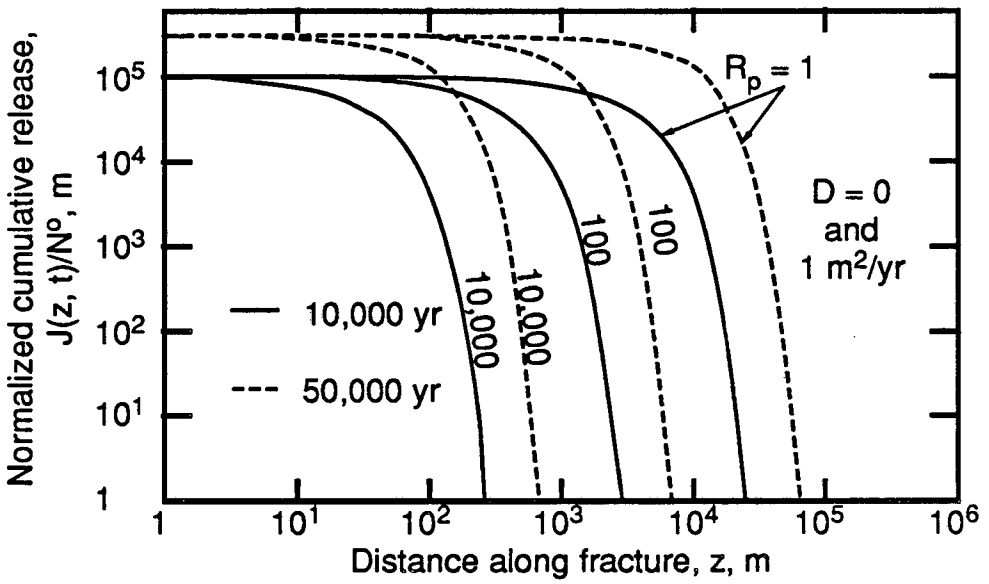

Figure 2.5(a) Profiles of normalized cumulative release in fracture as a function of distance from the source before and after the leach time. Parameters are assumed to be the same as Figure 2.4.

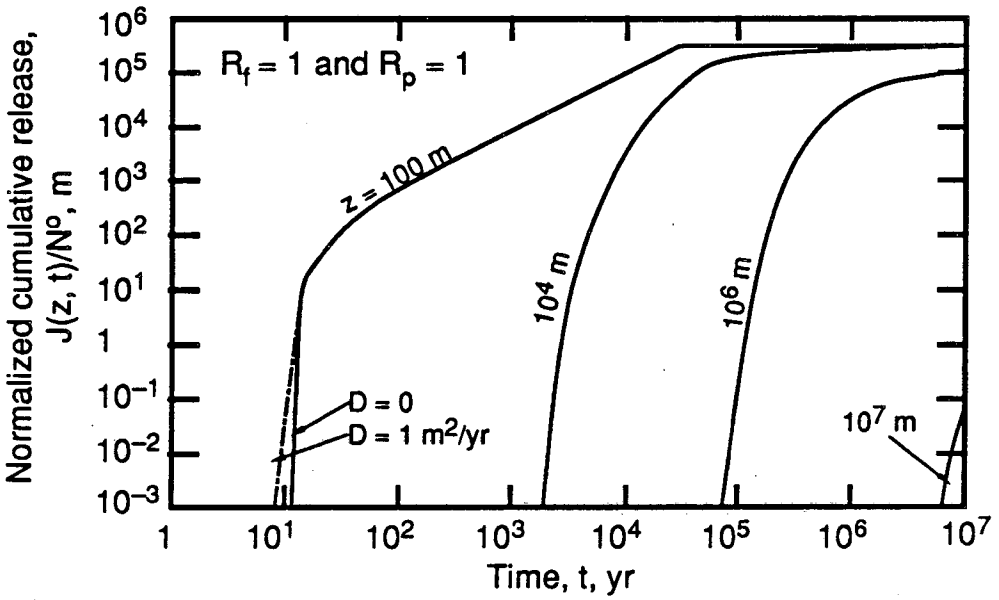

Figure 2.5(b) Change of normalized cumulative release with time at three locations in the fracture. As time increases, each curve approaches the value given by eq. (2.69).

In Figure 2.6 concentration profiles in the rock matrix at 10,000 yr and 50,000 yr at z = 100 m are depicted. In Figures 2.7(a) and (b), diffusive fluxes from the fracture to rock matrix at the rock-fracture interface normalized by the initial concentration at the boundary are plotted against the distance from the source for t = 10,000 yr and 50,000 yr, respectively. At 10,000 yr, before the end of the leach time, concentration decreases monotonically with the distance from the rock-fracture interface. Deeper penetration can be observed in Figure 2.6 for smaller pore retardation, resulting in smaller concentration gradient at the rock-fracture interface as shown in Figure 2.7(a).

At 50,000 yr, uncontaminated water enters into the fracture. From dashed curves for pore retardation factors 1 and 100 in Figure 2.6, we observe that back diffusion occurs, because concentration in the fracture is less than that in the rock matrix. In Figure 2.7(b) we see two domains; in the region near the source the diffusive flux becomes negative, and

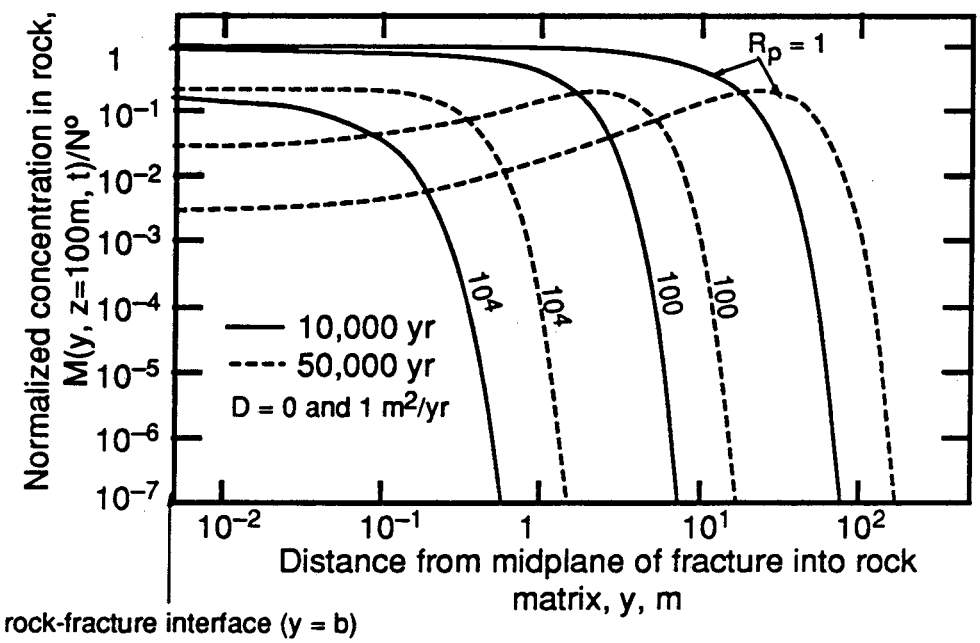

Figure 2.6 Normalized concentration in the rock matrix at z = 100 m as a function of distance from the midplane of the fracture. The rock-fracture interface locates at $y = b$. Parameters for Figure 2.4 apply.

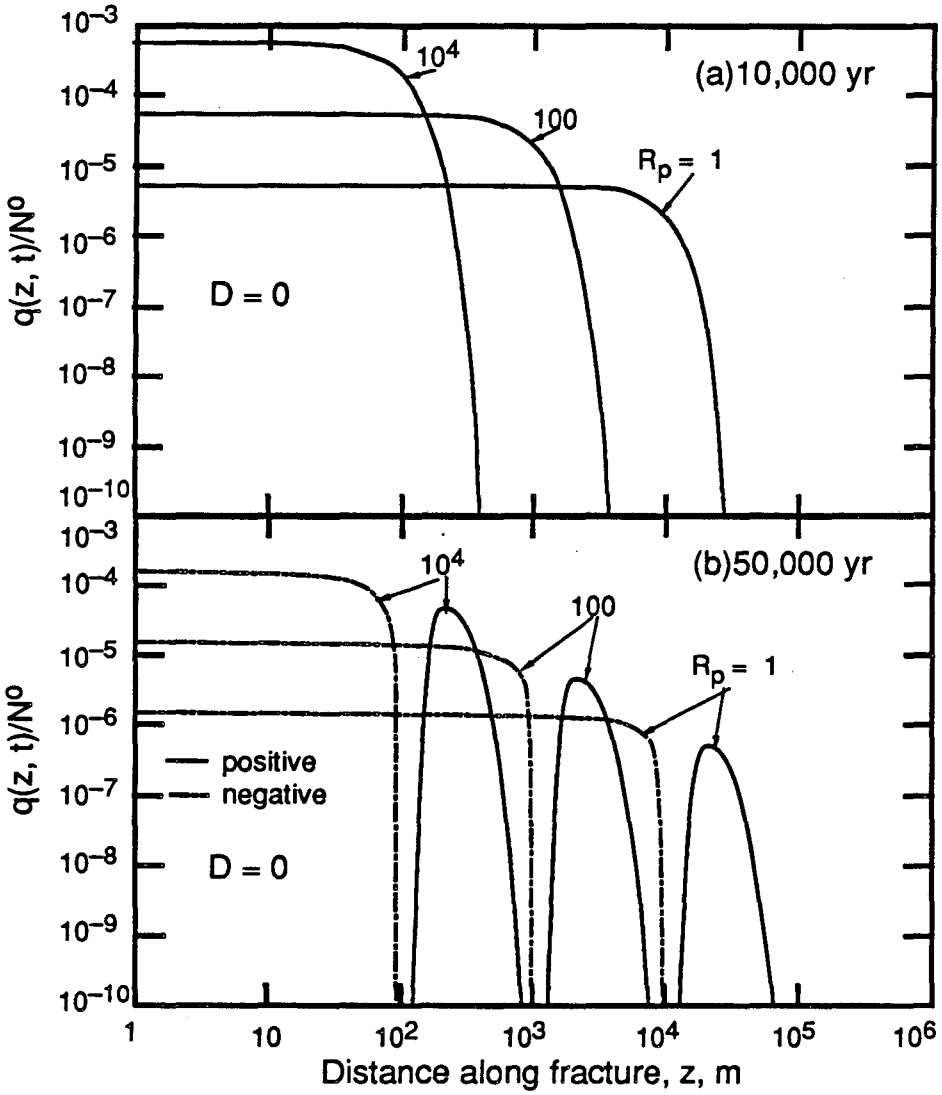

Figure 2.7 Diffusive mass flux across the rock-fracture interface from the fracture to rock matrix, normalized by the initial concentration at the boundary. Negative fluxes in the bottom figure mean that the contaminant diffuses from rock to the fracture. Parameter values in Figure 2.4 apply. Longitudinal dispersion coefficient is assumed to be zero.

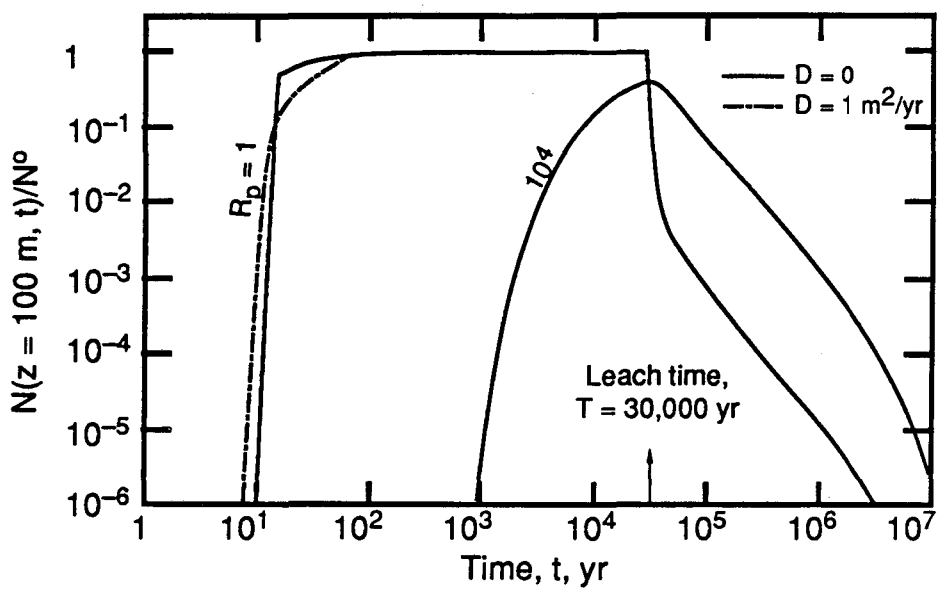

Figure 2.8 Change of normalized concentration in the fracture at $z = 100$ m as a function of time. Parameter values in Figure 2.4 apply.

in the far region positive. The 100-m-point for $R_p = 1$ and 100 is in the domain where the contaminant diffuses back to the fracture. Concentration in the rock matrix for $R_p = 10^4$ still shows the monotonically decreasing profile at 50,000 yr, meaning that the contaminant still diffuses from the fracture to the rock matrix at $z = 100$ m. In Figure 2.7(b) the 100-m-point for $R_p = 10^4$ exists in the domain where the contaminant diffuses into the matrix.

Figure 2.8 is a breakthrough curve at the 100-m-point in the fracture. For unit pore retardation factor the first contaminant reaches this point after 10 yr, and the nearly constant concentration is maintained until the release of the contaminant ceases at 30,000 yr. The tail after 30,000 yr results from back diffusion. For pore retardation of 10^4 arrival of the first contaminant delays by strong retardation due to sorption in the rock matrix. There is no flat region as for $R_p = 1$ because strong sorption in rock matrix takes the contaminant from the fracture before it reaches the 100-m-point. Slight effect of dispersion is observed for $R_p = 1$ at early times.

2.7 Conclusions

Analytical solutions to the quantities describing radionuclide migration through a planar fracture surrounded by rock matrix of infinite extent have been obtained, for a general release mode. Analytical solutions for a band release have been derived from these general solutions. From numerical investigation on the band-release solutions, the following observations are considered to be characteristic of fracture-flow transport:

(1) Even without sorption, nuclide migration through a fracture is retarded by matrix diffusion.

(2) Greater sorption in rock matrix causes larger concentration gradient at the rock/fracture interface, resulting in greater retardation of in-fracture transport.

(3) After the leach time, back diffusion occurs in the region near the fracture entrance. Back diffusion is one of the most important characteristics of transport through a fracture-matrix system, and so is thoroughly investigated in Chapter 4.

(4) From observations on the cumulative release, the contaminated area will remain within limited distance away from the source because of radioactive decay. For example, only about 0.01 percent of the total amount of ^{237}Np released into the fracture during the leach time reaches 10^6-m-point even without sorption in the entire medium.

(5) Longitudinal dispersion in the fracture seems insignificant. This will be investigated in detail in Chapter 3.

The model has been established based on a number of assumptions, which limit the validity of the model. We will question several of these assumptions in Chapter 5 and thereafter, such as (1) the effect of neighboring fractures (Chapter 5), (2) the effect of a decaying precursor (Chapter 6), (3) the effect of multiple-patch sources of finite areal extent and of transverse hydrodynamic dispersion in the fracture (Chapter 7), and (4) the effect of diffusion parallel to the fracture axis in rock matrix and planar geometry (Chapter 8).

References

[1] Bear, J., *Hydraulics of Groundwater*, McGraw-Hill, New York, 1979,

[2] Moreno, L., I. Neretnieks, and T. Eriksen, Analysis of Some Laboratory Tracer Runs in Natural Fissures, *Water Resouces Res. 21*, 951, 1985,

[3] Matheron, G., and G. de Marsily, Is Transport in Porous Media Always Diffusive? A Counterexample, *Water Resources Res., 16,* 901, 1980,

[4] Gelhar, L. W., and C. L. Axness, Three-dimensional Stochastic Analysis of Macrodispersion in Aquifer, *Water Resources Res., 19,* 161, 1983,

[5] INTRACOIN, *International Nuclide Transport Code Intercomparison Study, Final Report Levels 2 and 3, Model Validation and Uncertainty Analysis,* Stockholm, 1986,

[6] Weast, R. C. (ed.), *Handbook of Chemistry and Physics,* 5th ed., p. F62, Chemical Rubber Company Press, Boca Raton, Fla., 1976-1977,

[7] Brace, W. F., A. S. Orange, and T.R.Madden, The Effect of Pressure on the Electrical Resistivity of Water-Saturated Crystalline Rocks, *J. Geophys. Res., 70,* 5669, 1965,

[8] Abramowitz, M., and I. A. Stegun, *Handbook of Mathematical Functions with Formulas, Graphs, and Mathematical Tables,* 10th ed., Dover, New York, 1972,

[9] Chambré, P. L., *Notes for Mathematics 220A/B,* Department of Mathematics, University of California, Berkeley, 1984-1985,

[10] Harada, M., P. L. Chambré, M. Foglia, K. Higashi, F. Iwamoto, D. Leung, T. H. Pigford, and D. Ting, *Migration of Radionuclides Through Sorbing Media: Analytical Solutions —I,* LBL-10500, Lawrence Berkeley Lab., 1980,

[11] NAG library Mark 10, Numerical Algorithm Group,

[12] Long, J. C. S., *Verification and Characterization of Continuum Behaviour of Fractured Rock at AECL Underground Research Laboratory,* LBL-14975, Lawrence Berkeley Lab., 1985,

[13] Witherspoon, P. A., J. S. Y. Wang, K. Iwai, and J. E. Gale, Validity of Cubic Law for Fluid Flow in a Deformable Rock Fracture, *Water Resources Res., 16,* 6, 1980,

[14] Tsang, Y. W., and P. A. Witherspoon, Hydromechanical Behavior of a Deformable Rock Fracture Subject to Normal Stress, *J. Geophys. Res., 86,* 9287, 1981,

[15] Tsang, Y. W., and P. A. Witherspoon, The Dependence of Fracture Mechanical and Fluid Flow Properties on Fracture Roughness and Sample Size, *J. Geophys. Res., 88,* 2359, 1983,

[16] Neretnieks, I., Transport in Fractured Rocks, *Proceedings, Memories of the 17th International Congress of IAH, 17,* 301, International Assoc. of Hydrologists, Tucson, Arizona, 1985.

Chapter 3
Effect of Longitudinal Dispersion in Fracture-Flow Transport with Matrix Diffusion

3.1 Introduction

From numerical illustrations in the previous chapter, longitudinal dispersion in the fracture seems to be secondary, compared with matrix diffusion. *Rasmuson and Neretnieks* [1] investigated effect of longitudinal dispersion with spherical geometry for matrix diffusion instead of planar geometry used in the model in Chpater 2. They expressed the analytical solution in terms of Pechlet number. They observed concentration in the fracture as a function of time at z = 1,000 m for Pechlet numbers of 0.5, 5, and ∞, and concluded that longitudinal dispersion has a large impact on the early arrival of radionuclides. Assuming that ground water velocity in a fracture is about 1 m/yr and that the observation point is at 1,000 m, one can obtain the dispersion coefficient D as 2,000 m^2/yr and 200 m^2/yr for Pechlet numbers of 0.5 and 5, respectively. These values for D are fairly larger than the values used in Chapter 2.

Tang, Sudicky and Frind [2] studied effect of longitudinal dispersion in a planar fracture with the same geometry as in the model in Chapter 2, but with a different inlet boundary condition; a constant concentration boundary condition is assumed at $z = 0$. They used the following relation between longitudinal dispersion coefficient D and velocity v:

$$D = \alpha_L v + D_v , \qquad (3.1)$$

where α_L is dispersivity [m] and D_v is molecular diffusion coefficient in water. They assumed 0.5 m for α_L, 0.05 m^2/yr for D_v, and 3.65 m/yr and 36.5 m/yr for v, resulting in 1.8 m^2/yr and 18 m^2/yr, respectively. Although these values for D and v imply stronger advection than those assumed in *Rasmuson and Neretnieks*, they claimed considerable effect of longitudinal dispersion in the fracture. This might result from choosing tritium for

illustration. Because of the constant boundary condition, concentration in the medium eventually reaches the steady state. For a shorter half-life nuclide time for reaching the steady state becomes shorter. Within 100 yr concentration of tritium (half-life 12.35 yr) reaches its steady state. For such a relatively short period of time, however, matrix diffusion is not so effective, which otherwise would retard nuclide movement by longitudinal dispersion.

In this chapter studied are the effect of longitudinal dispersion subject to the band release and the effect of matrix diffusion on the dispersive transport in the fracture.

3.2 Theoretical Development

Importance of longitudinal hydrodynamic dispersion is usually discussed together with advective transport because hydrodynamic dispersion is caused by advection. To discuss, we rewrite the analytical solutions (2.34) for a general release mode and (2.51) for a band release in terms of Pechlet number,

$$Pe = \frac{z\,v}{D}. \tag{3.2}$$

As Pechlet number decreases, longitudinal dispersion becomes more prominent. For zero dispersion Pechlet number becomes infinity. For pure diffusion field Pechlet number becomes zero.

We obtain the following rewritten solutions for a general release and a band release, respectively,

$$N(T_n, t) = \frac{2}{\sqrt{\pi}} e^{Pe/2} \int_g^\infty G(\xi; T_n, t, Pe) e^{-\gamma\lambda} \int_0^{t-\gamma} \psi(t-\gamma-t') E(t'; \frac{\gamma}{A}) dt'\, d\xi,$$

$$t \geq 0,\ T_n \geq 0, \tag{3.3}$$

$$N(T_n, t) = F_1(b, T_n, t) - e^{-\lambda T} F_1(b, T_n, t-T),\quad t \geq 0,\ T_n \geq 0, \tag{3.4}$$

where

$$F_1(b, T_n, t) = \frac{2}{\pi} e^{Pe/2} \int_g^\infty G(\xi; T_n, t, Pe)\, e^{-\lambda t} erfc\left(\frac{\gamma/A}{2\sqrt{t-\gamma}}\right) d\xi, \qquad (3.5)$$

$$G(\xi; T_n, t, Pe) = exp\left(-\xi^2 - \frac{Pe^2}{16\xi^2}\right), \qquad (3.6)$$

$$g = \sqrt{\frac{Pe\, T_n}{4t}}, \qquad (3.7)$$

$$T_n = \frac{z\, R_f}{v}, \qquad (3.8)$$

$$\gamma = \frac{Pe\, T_n}{4\xi^2}, \qquad (3.9)$$

and

$$A = \frac{bR_f}{\varepsilon\sqrt{D_p R_p}} \ [yr^{1/2}]. \qquad (3.10)$$

A new variable T_n is introduced as well as Pechlet number. The nuclide travel time, T_n, is time for nuclide to reach the location z by advection subject to retardation by surface sorption on the fracture walls. Function $E(t'; k)$ is defined by (2.37).

Observation of (3.3) and (3.4) tells us that two parameters affect migration: Pe and A. Pechlet number represents the effect of longitudinal dispersion. Parameter A represents the effect of matrix diffusion. An infinite Pechlet number corresponds to the case of zero dispersion, where (2.41) and (2.60) are to be used instead of (3.3) and (3.4), respectively. By taking A infinity, solutions (3.3) and (3.5) approach

$$N(T_n, t) = \frac{2}{\sqrt{\pi}} e^{Pe/2} \int_g^\infty G(\xi; T_n, t, Pe)\, e^{-\gamma\lambda} \psi(t-\gamma)\, d\xi, \ t \geq 0, \ T_n \geq 0 \qquad (3.11)$$

and

$$F_1(b, T_n, t) = \frac{2}{\pi} e^{Pe/2} \int_g^\infty G(\xi; T_n, t, Pe)\, e^{-\gamma\lambda} d\xi, \qquad (3.12)$$

respectively (see Appendix A for derivation). Notice that these resultant expressions are

identical to the solutions to the partial differential equation without the q/b term in (2.5) subject to a general or a band release, respectively. Taking A to infinity is physically equivalent to making porosity of rock zero (so that no nuclide can diffuse into rock), or to making the fracture aperture infinitely large (no rock matrix exists). If A becomes smaller, the magnitude of the integrands in (3.3) and (3.5) reduces, resulting in smaller concentration. Transport in the fracture appears to be retarded.

An important consequence from these observations is that we must use for D the value measured without the influence of matrix diffusion. Measurement of longitudinal dispersion is, however, usually done under the influence of matrix diffusion. Values for D measured in a porous medium cannot apply, either, because size and shape of pores in a porous medium are quite different from those of fractures, resulting in different hydrodynamic properties.

3.3 Numerical Illustrations

Breakthrough curves for different Pechlet numbers are given in Figures 3.1 and 3.2. These graphs show change of ^{237}Np concentration in the fracture with time at the location, T_n = 1,000 yr, the distance such that it takes 1,000 yr advection for nuclide to reach the location subject to retardation due to surface sorption. In each graph, three curves are depicted for Pechlet numbers of 1, 100, and ∞. Two graphs compare the effect of matrix diffusion represented by parameter A. The band release is assumed.

Figure 3.1 is for A = 100 yr$^{1/2}$. In this case matrix diffusion has very little influence on transport in the fracture. With values of R_f = 1, ε = 0.01, D_p = 0.01 m^2/yr, and R_p = 1, half-width of the fracture b can be calculated as 10 cm, which is unrealistically large for fractures. Because of very small effect of matrix diffusion, the profile for $Pe \rightarrow \infty$ keeps the band shape, which is originated by the assumed boundary condition. After the leach time, T = 30,000 yr, we can observe a trailing tail due to back diffusion. For Pe = 100, the contaminant arrives about 500 years earlier than the case of zero dispersion ($Pe \rightarrow$

∞). The maximum concentration is reduced by dispersion. For $Pe = 1$, the contaminant appears 100 times earlier than in the case of zero dispersion.

In Figure 3.2 breakthrough curves for $A = 1$ yr$^{1/2}$ (strong matrix diffusion) are illustrated. By comparison of zero-dispersion curves in Figures 3.1 and 3.2, we can observe the effects of matrix diffusion such as retardation of the first arrival of the contaminant, disappearance of a band shape, and the reduction of concentration. From the curves for $Pe = 100$ in the both graphs, it is observed that matrix diffusion weakens influence of longitudinal dispersion; the difference between the curves for infinite Pechlet number and $Pe = 100$ is smaller in Figure 3.2 than in Figure 3.1. But matrix diffusion becomes less effective for $Pe = 1$ than for $Pe = 100$. This comparison implies that, regardless of its strength as measured by $1/A$, matrix diffusion has negligible effect on the early-time behaviour of radionuclides if Pe is as small as unity.

On the profiles after the leach time, longitudinal dispersion becomes less important because the principal process is back diffusion from the rock matrix as we see in the next chapter.

Next two figures are given for discussion on conservativeness of the model. Figures 3.3 and 3.4 show the profiles of concentration in the fracture as a function of the distance along the fracture at $t = 100$ yr and 10,000 yr, respectively. In each figure, three curves are compared: (1) zero longitudinal dispersion, a relatively large velocity ($v = 10$ m/yr) and a large fracture aperture ($2b = 1$ cm), (2) large longitudinal dispersion ($D = 1{,}000$ m^2/yr), a smaller, but more likely velocity ($v = 1$ m/yr) and a large aperture ($2b = 1$ cm), and (3) the same values as (2) for D and v, and a smaller but more likely value for a fracture aperture ($2b = 0.1$ mm). Thus, case (3) can be considered to be the most likely case in actual rock.

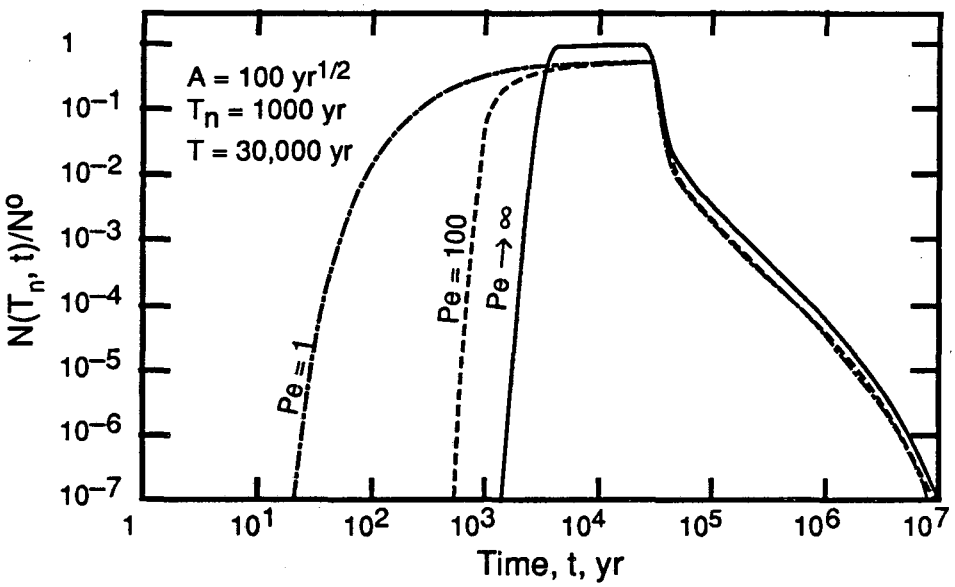

Figure 3.1 Effect of Pechlet number on breakthrough curves at $T_n = 1000$ yr for a band release. ^{237}Np is assumed. Concentration is normalized by the initial boundary concentration N^o.

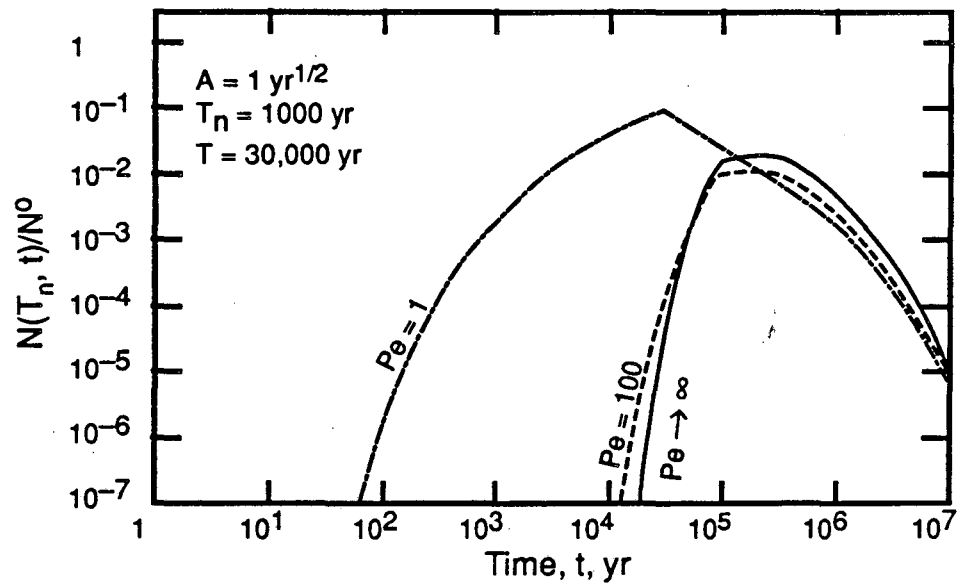

Figure 3.2 Same as Figure 3.1 except that stronger matrix diffusion is assumed here.

In many observations [3] a fracture aperture is about 1 mm or less. If we assume the cubic law for hydraulic conductivity [4], velocity in the fracture can be expressed as:

$$v = \frac{\rho g}{\eta} \frac{1}{2(S+b)} \frac{(2b)^3}{12} i, \qquad (3.13)$$

where

ρ : density of water (= 1,000 kg/m^3),

g : gravitational constant (= 9.807 m/s^2),

η : viscosity of water (= 0.001 Ns/m^2),

$2S$: fracture spacing (= 50 m), and

i : hydraulic gradient (= 3×10^{-3} m/m).

Using the values inside the brackets, obtained from [3], and $2b$ = 1 mm gives velocity as v = 1.55 m/yr. We can consider this value as a reasonable estimate for crystalline rock in many locations.

By cases (1) and (2) we can observe the effects of Pechlet number. Pechlet numbers for cases (1) and (2) become infinity and 1 at z = 1,000 m, respectively. We can see from Figures 3.3 and 3.4 that in early times due to longitudinal dispersion the contaminant reaches twice as farther in case (2) than in case (1), so that case (1) looks no longer conservative. In later times (Figure 3.4) because of matrix diffusion longitudinal dispersion becomes less predominant, and case (1) becomes conservative. If we use a more realistic value for a fracture aperture, the conservativeness of case (1) is reserved even for early times. The profiles for case (3) are far behind the profiles for case (1). Thus, if we choose the large values for velocity and fracture aperture, zero dispersion could be a conservative assumption.

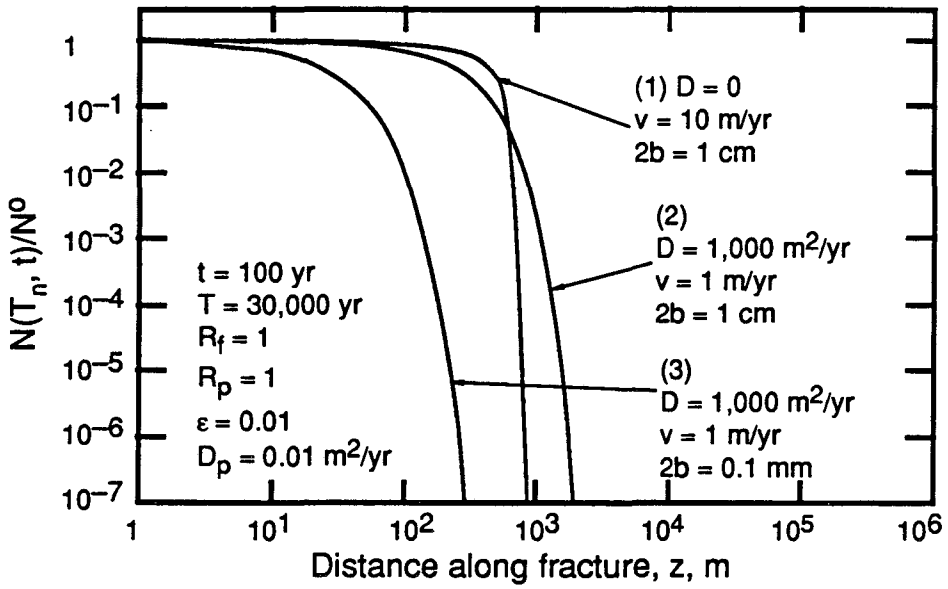

Figure 3.3 Conservativeness of zero dispersion against the case with high dispersion and low velocity. At time as early as 100 yr zero-dispersion model cannot be conservative. But compared with a realistic fracture aperture, $2b$ = 0.1 mm, zero dispersion is still a conservative assumption.

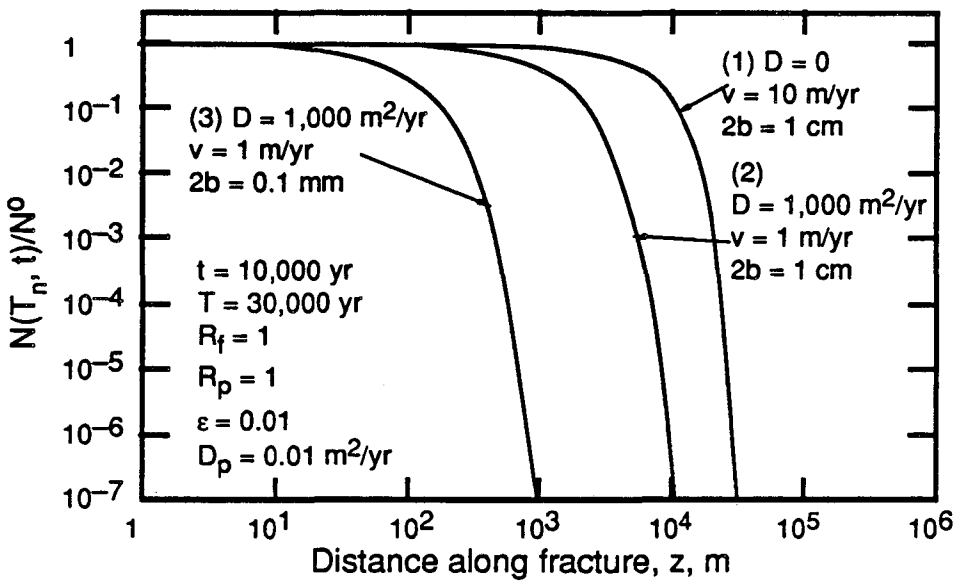

Figure 3.4 Same as Figure 3.3 except that t = 10,000 yr. In this time region high velocity and zero dispersion is a conservative assumption.

3.4 Conclusions

In early times longitudinal dispersion has a predominant effect on transport in the fracture. At about $Pe = 1$ matrix diffusion has little influence on longitudinal dispersion. The effect of matrix diffusion becomes significant as Pechlet number increases.

In later times longitudinal dispersion has less effect on transport in the fracture. Especially after the leach time longitudinal dispersion is negligible.

The case of $v = 10$ m/yr, $2b = 1$ cm, and $D = 0$ is conservative against more realistic cases, and so is used in the later chapters.

References

[1] Rasmuson, A., and I. Neretnieks, Migration of Radionuclides in Fissured Rock: The Influence of Micropore Diffusion and Longitudinal Dispersion, *J. Geophys. Res., 86,* 3749, 1981,

[2] Tang, D. H., E. O. Frind, and E. A. Sudicky, Contaminant Transport in Fractured Porous Media: Analytical Solution for a Single Fracture, *Water Resources Res., 17,* 555, 1981,

[3] Neretnieks, I., Diffusion in the Rock Matrix: An Important Factor in Radionuclide Retardation?, *J. Geophys. Res., 85,* 4379, 1980,

[4] Snow, D. T., *A Parallel Plate Model of Fractured Permeable Media,* Ph. D. Thesis, University of California, Berkeley, 1965.

Chapter 4

Analysis of Back Diffusion in Fracture-Flow Transport

4.1 Introduction

Transport of radionuclide through a planar fracture after the source at the fracture entrance ceases emitting the nuclide is of principal interest in this chapter. In fracture-flow transport we have very different transport path of the contaminant between before and after the source ceases emitting the contaminant (see Figure 4.1). During the leach time the contaminant in the fracture is diffusing into the rock matrix throughout the fracture. After the leach time, uncontaminated water begins to enter the fracture. In the region near the fracture entrance, it is expected that the concentration in the fracture is smaller than that in the rock matrix, so the contaminant is coming out of the rock matrix. We call this back diffusion. Because of back diffusion, non-zero concentration is expected to be observed in the near-region even long after the source ceased emitting the contaminant, which is not observed in the case without matrix diffusion.

To investigate, we first consider a model which is based on a physically hypothetical situation. The entire rock matrix is initially contaminated uniformly while there is no nuclide in the fracture. Then, uncontaminated water begins to enter the fracture,

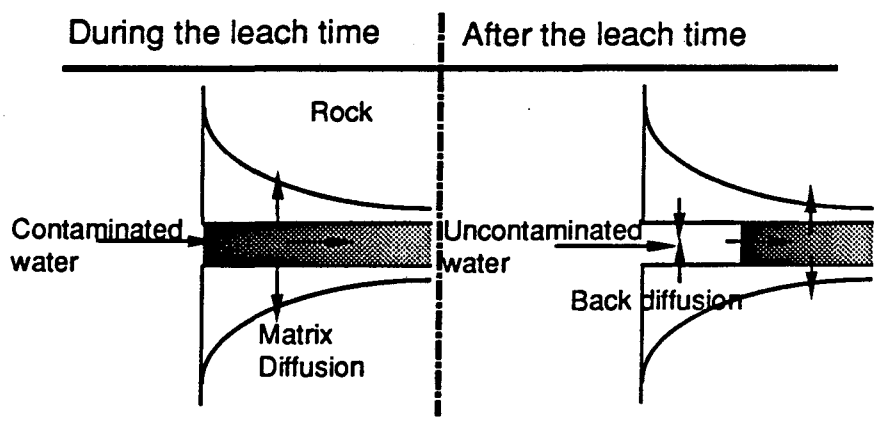

Figure 4.1 Illustration of back diffusion

and due to the concentration gradient between the fracture and the rock matrix, nuclide in the rock matrix diffuses out to the fracture.

4.2 Formulation of Problem

Except that the longitudinal dispersion in the fracture is not included based on the argument in the previous chapter, we make the same assumptions made in Chapter 2 for deriving the governing equations (2.5) and (2.9). Then we have the following governing equations as:

$$R_f \frac{\partial N}{\partial t} + v \frac{\partial N}{\partial z} + R_f \lambda N + \frac{q}{b} = 0, \quad t > 0, z > 0, \tag{4.1}$$

and

$$R_p \frac{\partial M}{\partial t} - D_p \frac{\partial^2 M}{\partial y^2} + R_p \lambda M = 0, \quad t > 0, y > b, z > 0. \tag{4.2}$$

Refer to Chapter 2 for nomenclature. These two governing equations are coupled by (2.11). We cite again here for further reference:

$$q(z, t) = -\varepsilon D_p \left. \frac{\partial M}{\partial y} \right|_{y=b}, \quad z > 0, t > 0. \tag{4.3}$$

We solve (4.1) and (4.2) subject to the following side conditions:

Initial Conditions:

$$N(z, 0) = \Phi(z), \quad z > 0, \tag{4.4}$$

$$M(y, z, 0) = \Psi(y, z), \quad y > b, \quad z > 0, \tag{4.5}$$

Boundary Conditions:

$$N(0, t) = \psi(t), \quad t > 0, \tag{4.6}$$

$$M(b, z, t) = N(z, t), \quad t > 0, z > 0, \tag{4.7}$$

$$M(\infty, z, t) < \infty, \quad t > 0, z > 0. \tag{4.8}$$

(4.4) and (4.5) characterize the present problem. In Chapter 2, we solved the problem with $\Phi(z) = \Psi(y, z) = 0$. Note that initially $N(z, 0)$ is not necessarily identical to $M(b, z, 0)$ by the initial conditions (4.4) and (4.5). As shown later the inhomogeneity on the initial con-

ditions requires a more complex procedure to solve the problem.

4.3 Derivation of Analytical Solutions

We will develop the solution to the coupled system of (4.1), (4.2), and (4.3) subject to the side conditions (4.4) through (4.8). The method is basically as follows: First apply the Laplace transform on (4.2) and solve the subsidiary second-order ordinary differential equation. Second express the concentration gradient at the interface $q(z,t)$ in terms of Laplace transform, substitute the Laplace-transformed concentration gradient into the Laplace-transformed (4.1), and solve the subsidiary first-order ordinary differential equation. Finally, invert the solutions of the subsidiary problems to the real time domain.

Applying the Laplace transform to (4.2) yields

$$\frac{d\tilde{M}}{dy^2} - B^2(p+\lambda)\tilde{M} + B^2\Psi(y,z) = 0, \quad y > b, \quad z > 0, \tag{4.9}$$

subject to

$$\tilde{M}(b,z,p) = \tilde{N}(z,p), \quad z > 0, \tag{4.10}$$

$$\tilde{M}(\infty,z,p) < \infty, \quad z > 0, \tag{4.11}$$

where

$$B = \sqrt{\frac{R_p}{D_p}}, \tag{4.12}$$

and the tilde, ~, stands for the image function of the Laplace transform of a function and p a Laplace variable, complex. When we obtained (4.9), we used the identity [1]:

$$\mathcal{L}\left[\frac{\partial M}{\partial t}\right] = p\tilde{M} - M(y,z,+0), \tag{4.13}$$

where $\mathcal{L}[\cdot]$ represents the Laplace transform, with the help of the initial condition (4.5). The ordinary differential equation (4.9) can be solved with the help of the Green's function method. The derivation of the Green's function is shown in Appendix B. We write only the result here. The Green's function for (4.9) is written as:

$$G(y, s) = \begin{cases} \frac{1}{\beta} \sinh\{\beta(y-b)\}\, e^{-\beta(s-b)}, & b \le y \le s \\ \frac{1}{\beta} \sinh\{\beta(s-b)\}\, e^{-\beta(y-b)}, & s \le y < \infty \end{cases} \qquad (4.14)$$

where

$$\beta = B\sqrt{p+\lambda}\,. \qquad (4.15)$$

Knowing the Green's function, we can write the solution to (4.9) subject to (4.10) and (4.11) in terms of the Green's function and the inhomogeneity function as:

$$\tilde{M}(y, z, p) = \int_b^\infty G(y, s) B^2 \Psi(s, z) ds - \left[\tilde{M}(s, z, p) \frac{\partial}{\partial s} G(y, s) \right]_b^\infty . \qquad (4.16)$$

Differentiating (4.14) with respect to s, substituting the resultant expression into (4.16) together with (4.10) and (4.11), and considering that the derivative of $G(y, s)$ with respect to s vanishes if s tends to infinity, we obtain the solution to the subsidiary problem (4.9):

$$\tilde{M}(y, z, p) = \tilde{N}(z, p)\, e^{-\beta(y-b)} + \frac{B^2}{\beta} \sinh\{\beta(y-b)\} \int_y^\infty e^{-\beta(s-b)} \Psi(s, z)\, ds$$

$$+ \frac{B^2}{\beta} e^{-\beta(y-b)} \int_b^y \sinh\{\beta(s-b)\}\, \Psi(s, z)\, ds. \qquad (4.17)$$

Next, we apply the Laplace transfom on (4.11), obtaining

$$\frac{d\tilde{N}}{dz} + \frac{R_f}{v}(p+\lambda)\tilde{N} - \frac{R_f}{v}\Phi(z) + \frac{\tilde{q}}{bv} = 0, \qquad z > 0, \qquad (4.18)$$

subject to

$$\tilde{N}(0, p) = \tilde{\psi}(p). \qquad (4.19)$$

Differentiating (4.17) with respect to y and substituting $y = b$, we obtain

$$\tilde{q}(z, p) = \varepsilon\sqrt{D_p R_p}\sqrt{p+\lambda}\,\tilde{N}(z, p) - \varepsilon R_p \int_b^\infty e^{-\beta(s-b)} \Psi(s, z)\, ds. \qquad (4.20)$$

Upon substitution of (4.20), (4.18) becomes

$$\frac{d\tilde{N}}{dz} + \eta\tilde{N} - \Lambda(z,p) = 0, \qquad z > 0, \tag{4.21}$$

where

$$\eta \equiv \frac{R_f}{v}\left(p + \lambda + \frac{\sqrt{p+\lambda}}{A}\right), \qquad A \equiv \frac{bR_f}{\varepsilon\sqrt{D_p R_p}}, \text{ and} \tag{4.22}$$

$$\Lambda(z,p) \equiv \frac{R_f}{v}\left\{ \Phi(z) + \frac{B}{A}\int_b^\infty e^{-\beta(s-b)}\Psi(s,z)\,ds \right\}. \tag{4.23}$$

Equation (4.21) is a first-order ordinary differential equation which has a solution of the form:

$$\tilde{N}(z,p) = \tilde{\psi}(p)\, e^{-\eta z} + \int_0^z \Lambda(\xi,p)\, e^{-\eta(z-\xi)} d\xi. \tag{4.24}$$

Here we used the boundary condition (4.19).

Now we make inverse Laplace transforms of (4.24) and (4.17) to a real time domain. On inversion we make use of the shift property of Laplace transform [1], (2.32), (2.33), and, from Reference [2],

$$\mathcal{L}^{-1}\left[\frac{1}{\sqrt{p}} e^{-k\sqrt{p}}\right] = \frac{1}{\sqrt{\pi t}} e^{-\frac{k^2}{4t}}, \qquad k \geq 0,\ t > 0, \tag{4.25}$$

and the convolution theorem:

$$\mathcal{L}^{-1}\left[\tilde{f}_1(p)\tilde{f}_2(p)\right] = \int_0^t f_1(t-\tau) f_2(\tau) d\tau. \tag{4.26}$$

Notice that (2.33) becomes a Dirac's delta function as k goes to zero. At $k = 0$,

$$\lim_{k\to 0} \mathcal{L}^{-1}\left[e^{-k\sqrt{p}}\right] = \delta(t). \tag{4.27}$$

Applying these identities, we can finally obtain the solution to the problem (4.1) and (4.2), coupled by (4.3), subject to the initial and boundary conditions (4.4) through (4.8) as follows:

$$N(z, t) = P(b, z, t), \qquad z \geq 0,\ t \geq 0, \tag{4.28}$$

$$M(y, z, t) = P(y, z, t) + \int_b^y Be^{-\lambda t}\Psi(s, z)\kappa(t; B(y-s))ds + \int_y^\infty Be^{-\lambda t}\Psi(s, z)\kappa(t; B(s-y))ds$$

$$- \int_b^\infty B\, e^{-\lambda t}\Psi(s, z)\kappa(t; B(y+s-2b))ds. \qquad y \geq b,\ z > 0,\ t \geq 0, \tag{4.29}$$

where

$$P(y, z, t) = e^{-\lambda t}\int_0^z \frac{R_f}{v}\Phi(z-\xi)K\left(t - \frac{R_f\xi}{v}; \frac{R_f\xi}{vA} + B(y-b)\right)d\xi + \frac{\varepsilon R_p}{bv}e^{-\lambda t}$$

$$\times \int_0^z \int_b^\infty \Psi(s, z-\xi)K\left(t - \frac{R_f\xi}{v}; \frac{R_f\xi}{vA} + B(y+s-2b)\right)ds\, d\xi$$

$$+ \int_0^t \psi(t-\tau)\, e^{-\lambda\tau}\, K\left(\tau - \frac{R_f z}{v}; \frac{R_f z}{vA} + B(y-b)\right)d\tau, \tag{4.30}$$

$$K(\alpha; \mu) = h(\alpha)\frac{\mu}{2\sqrt{\pi\alpha^3}}\, e^{-\frac{\mu^2}{4\alpha}}, \tag{4.31}$$

and

$$\kappa(t; \theta) = \frac{1}{2\sqrt{\pi t}}\, e^{-\frac{\theta^2}{4t}}. \tag{4.32}$$

4.4 Analysis of Back Diffusion

4.4.1 Assumptions and Analytical Solutions for Hypothetical Model

To simplify, we will observe the back diffusion under the following assumptions (see Figure 4.2):

(1) The same physical processes related to nuclide transport as mentioned in Chapter 2 except longitudinal dispersion in the fracture are considered here. Thus, the governing

equations (4.1) and (4.2) hold.

(2) Initially, the uniform concentration M^o is loaded in the pore water throughout the rock matrix ($y > b$, $z > 0$), whereas the initial concentration is zero in the entire fracture ($z > 0$).

(3) After $t = 0$, uncontaminated water enters the fracture.

With these assumptions, the present problem can be described by the governing equations (4.1) and (4.2) subject to the following side conditions:

$$N(z, 0) = \Phi(z) \equiv 0, \quad z > 0, \tag{4.33}$$

$$M(y, z, 0) = \Psi(y, z) \equiv M^o, \quad y > b, z > 0, \tag{4.34}$$

$$N(0, t) = \psi(t) \equiv 0, \quad t > 0, \tag{4.35}$$

$$M(b, z, t) = N(z, t), \quad t > 0, \ z > 0, \tag{4.36}$$

$$M(\infty, z, t) = M^o e^{-\lambda t}, \quad t > 0, \ z > 0. \tag{4.37}$$

Assumption (2) provides the initial conditions (4.33) and (4.34). Boundary condition (4.35) is based on assumption (3). (4.37) comes from physical consideration.

We can obtain the solutions on substitution of these side conditions into (4.28) and (4.29), resulting in

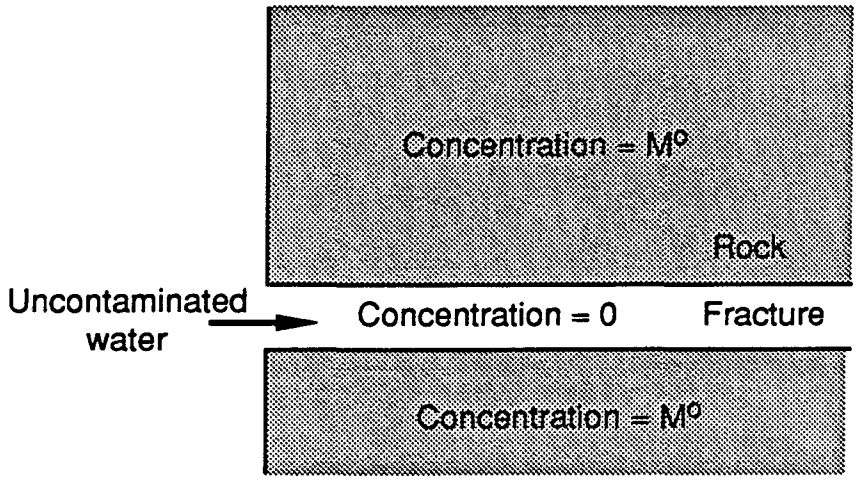

Figure 4.2 Illustration of initial conditions for the hypothetical model.

$$N(z, t) = M^o e^{-\lambda t}\left[F_t(b, t) - F_z(b, z, t)\right], \qquad z \geq 0,\ t \geq 0, \tag{4.38}$$

$$M(y, z, t) = M^o e^{-\lambda t}\left[F_t(y, t) - F_z(y, z, t)\right], \qquad y \geq b,\ z > 0,\ t \geq 0, \tag{4.39}$$

where

$$F_t(y, t) = 1 - exp\left(-\frac{B^2(y-b)^2}{4t}\right) H\left(\frac{\sqrt{t}}{A} + \frac{B(y-b)}{2\sqrt{t}}\right), \tag{4.40}$$

$$F_z(y, z, t) = h(t - ZA)\, exp\left(-\frac{\{Z + B(y-b)\}^2}{4(t-ZA)}\right)\left\{H\left(\frac{Z + B(y-b)}{2\sqrt{t-ZA}}\right)\right.$$

$$\left. - H\left(\frac{Z + B(y-b)}{2\sqrt{t-ZA}} + \frac{\sqrt{t-ZA}}{A}\right)\right\}, \tag{4.41}$$

$$H(x) = e^{x^2} erfc(x), \quad Z = \frac{R_f z}{vA}, \quad A = \frac{bR_f}{\varepsilon\sqrt{D_p R_p}}. \tag{4.42}$$

We derive here the concentration gradient at the interface $y = b$ for further observation. Differentiating (4.39) with respect to y and substituting $y = b$ into the resultant expression yields:

$$\theta(z, t) \equiv -\frac{q(z, t)}{\varepsilon D_p} = \left.\frac{\partial M}{\partial y}\right|_{y=b} = \frac{B}{A} M^o e^{-\lambda t}\left\{\frac{A}{\sqrt{\pi t}} - H\left(\frac{\sqrt{t}}{A}\right) + g(z, t)\right\}, \quad z > 0,\ t > 0, \tag{4.43}$$

where

$$g(z, t) = h(t - ZA)\, exp\left(-\frac{Z^2}{4(t-ZA)}\right) H\left(\frac{\sqrt{t-ZA}}{A} + \frac{Z}{2\sqrt{t-ZA}}\right). \tag{4.44}$$

4.4.2 Numerical Illustrations and Observations

For illustration, we take a stable nuclide ($\lambda = 0$), and assume that the nuclide is not sorbed either on the fracture walls or on the rock-pore surfaces (R_f=1 and $R_p = 1$). The porosity ε of the rock matrix, the fracture width, $2b$, water velocity v in the fracture, and the molecular diffusion coefficient D_p are chosen based on the argument in Chapter 3, and shown in Figure 4.3.

Figure 4.3 shows the relative nuclide concentration in the fracture as a function of the downstream distance z, for six values of time. In each curve we can see two apparent regions; the concentration increases with the downstream distance z up to a certain point, and beyond that point the concentration becomes independent of z. We can also observe that the location of the point dividing the two regions proceeds with time along the fracture, and that the concentration of the plateau region in each curve increases with time.

The analytical solution (4.38) implies that because of the existence of the Heaviside step function $h(t - ZA)$, $F_z(b, z, t)$, (4.41), vanishes in the region ahead of the point $z_a = \frac{vt}{R_f}$, so that the concentration becomes only dependent on time. We call the point $z_a = \frac{vt}{R_f}$ the advection front. We denote the region $z \leq z_a$ as region A, and the region $z > z_a$ region B.

Let us take the curve for $t = 10$ yr for example. Water which entered the fracture at $t = 0$ reaches the location $z = 100$ m. The region between $z = 0$ and $z = 100$ m, i.e., region A has already been washed by water which is uncontaminated at the entrance. Uncontaminated water entering the fracture receives nuclide from the rock matrix as being transported along the fracture because the concentration in the fracture is lower than the concentration in the rock matrix. And the concentration in region A increases linearly with the distance z although linearity is not clear in this graph because of the semi-log plot. The increase rate, or the slope against the z-axis becomes smaller as time increases. This implies that the mass flux from the rock matrix decreases with time, uniformly with z in the entire region A. We will investigate this fact in a more detailed fashion in the next figure by observing the gradient at the interface. Beyond the advection front located at $z = 100$ m, the fresh water has not arrived yet. The water in region B had already existed in the fracture at $t = 0$. Region B advances in the fracture by advection, receiving nuclide from rock matrix by back diffusion, and so the concentration is independent of z there.

Region B conincides with the plateau region at early times. However, at later times the concentration reaches the plateau value inside region A. For example, at $t = 1{,}000$ yr,

the advection front is advanced as far as z = 10,000 m while the plateau region seems to exist in the region z greater than 5,000 m. This tendency can be observed slightly at t = 100 yr and clearly at t = 1,000 yr or later. This fact is newly discovered in the present study, and because of its importance, we will pursue later the physical mechanism with which the discrepancy between the advection front and the plateau edge occurs. However, from the mathematical point of view, we can say that the discrepancy occurs because the exponential factor,

$$exp\left(-\frac{z^2}{4(t-ZA)}\right), \qquad (4.45)$$

in $F_z(b, z, t)$, (4.41), becomes so small for large z values that $F_z(b, z, t)$ becomes negligible to $F_t(b, t)$. Then the concentration $N(z, t)$ can be approximated as

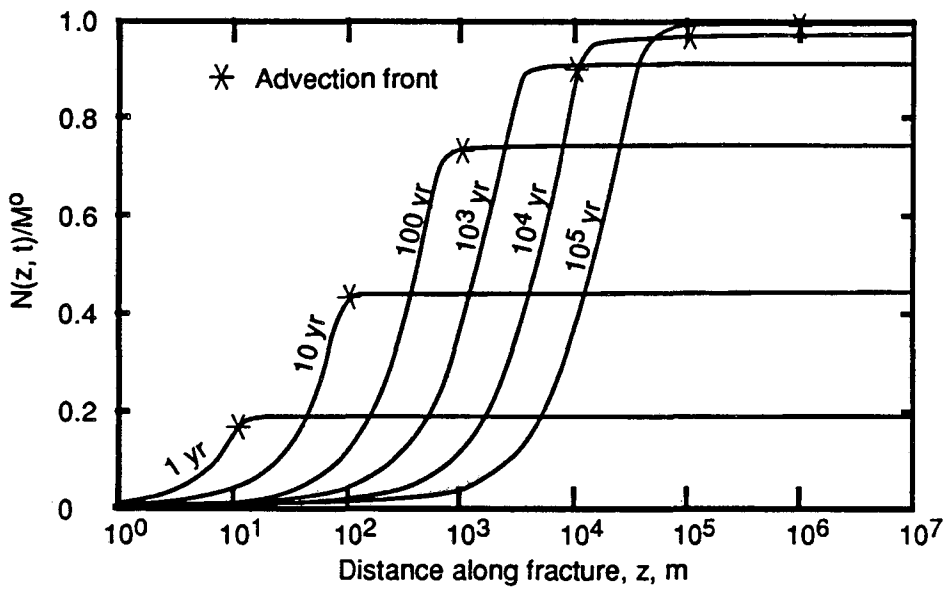

Figure 4.3 Relative concentration in the fracture as a function of distance along fracture. Assumed parameter values are: v = 10 m/yr, b = 0.05 m, D_p = 0.01 m^2/yr, R_f = 1, R_p = 1, λ = 0, ε = 0.01. The asterisk represents the point where the advection front reaches at the corresponding time. Region A and B are located to the left and right of the advection front, respectively, at each time.

$$N(z, t) \approx N^{o} e^{-\lambda t} F_{t}(b, t), \qquad (4.46)$$

which is identical to the functional form that represents the plateau region. Thus, we can point out from the mathematical observation that the argument of the exponential factor (4.45), which is a dimensionless number, acts a very important roll in a fracture-flow transport associated with matrix diffusion.

Figure 4.4 shows the concentration gradient at the interface of the fracture and the rock matrix as a function of the downstream distance z. The gradient is normalized by the initial concentration M^{o} in the rock pores. In each curve there are two distinguishable flat regions. At every time shown in the figure the concentration gradient in the near-region is greater than that in the far-region, and the difference of these two gradients increases with time. The concentration gradient, however, decreases with time in the entire interface.

At a very early time because the concentration in the fracture is very small, the gradient at the interface is large. The gradient in the near-region is slightly greater than that in the far-region because uncontaminated water carries the radionuclide discharged from the rock matrix, so that the concentration is maintained lower than that in the far-region. In the far-region the gradient decreases with time because of the accumulation of nuclides by back diffusion. The gradient in the near-region decreases with time at a smaller rate than in the far-region. Because the concentration in the fracture in the near-region is kept low due to the wash-out by the fresh water, the concentration difference between the fracture and the rock is greater than in the far-region. Therefore, the difference between the gradients in the two regions increases with time. Regions A and B mentioned in the previous figure, i.e., the regions to the left and right of the advection front, respectively, coincide with the near-, and the far-regions, respectively in early times. Later there occurs a region inside region A where the gradient is the same as that in region B. The flat profile in the near-region results in the linear increase of the concentration in region A as shown in Figure 4.3.

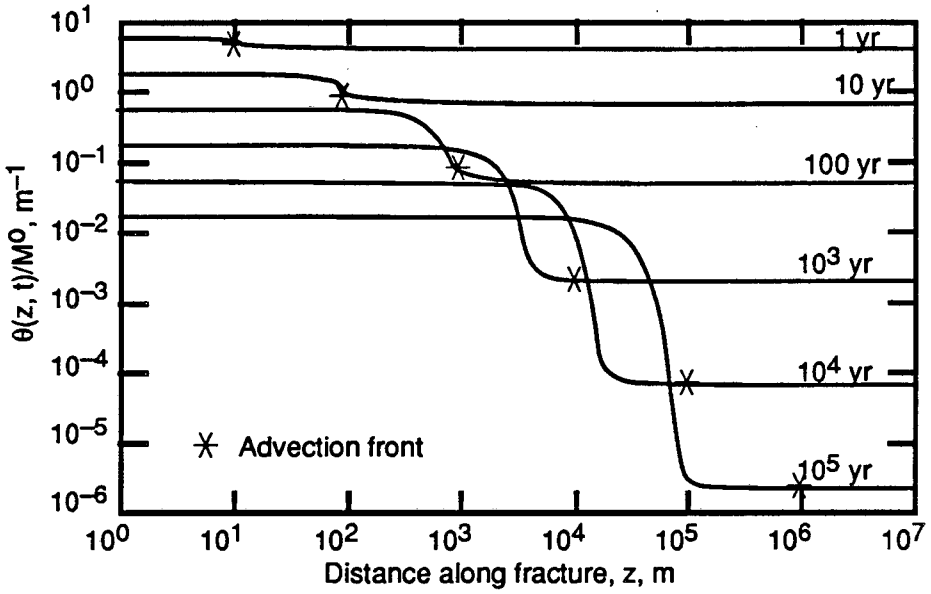

Figure 4.4 Concentration gradient at the interface y = b, normalized by the initial concentration in the rock. The same parameter values as Figure 4.3 apply.

Observing the analytical solution (4.43), one can see that the exponential factor (4.45) is included in *g(z,t)*, (4.44), and again controls the position of the point dividing the near-region and the far-region. As observed in Figure 4.3, the dividing point does not coincide with the advection front, especially for the large-*t* cases. If the argument of the exponential factor approaches zero, *g(z,t)* becomes very close to the *H* function in (4.43) so that the two functions cancel. Thus the value of the concentration gradient in the near-region is expressed as

$$\theta(z,t) = \frac{B}{A} M^o e^{-\lambda t} \frac{A}{\sqrt{\pi t}}, \qquad \textit{for small } z. \tag{4.47}$$

As *z* increases, the exponential factor becomes so small that *g(z, t)* becomes negligible even in the near-region, and the gradient can be expressed as;

$$\theta(z,t) = \frac{B}{A} M^o e^{-\lambda t} \left\{ \frac{A}{\sqrt{\pi t}} - H\left(\frac{\sqrt{t}}{A}\right) \right\}. \tag{4.48}$$

Thus for a large *t* the gradient begins to decrease at the point much to the left of the advection front. This observation coincides with what we have observed in Figure 4.3.

Figure 4.5 shows the time-dependency of the concentration in the fracture and the concentration gradient at the interface observed at two fixed locations, z = 100 m and 100,000 m. The left vertical axis represents the concentration in the fracture and the right vertical axis the gradient at the interface, both normalized by the initial concentration in the rock. The advection front passes the z = 100 m point at t = 10 yr. Before t = 10 yr, the concentration increases with time due to the back diffusion, and the location z = 100 m is situated in region B in Figure 4.3. Water reaching z = 100 m after t = 10 yr is the one which entered the fracture after t = 0. After 10 yr the concentration decreases with time at z = 100 m because of the wash-out by uncontaminated water entering the fracture.

The gradient at z = 100 m decreases with time until the advection front reaches this point because the nuclide coming out of the rock matrix accumulates in the fracture. The gradient increases for a short period of time after the advection front has passed, because

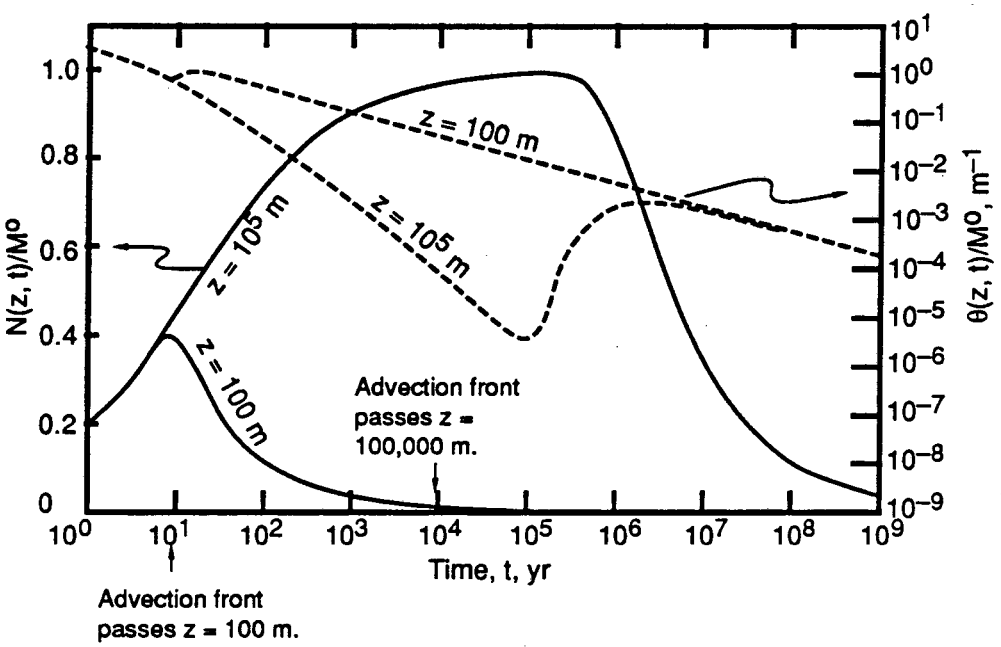

Figure 4.5 Changes in time of the relative concentration in the fracture and the concentration gradient at the interface y = b, normalized by the initial concentration in the rock matrix, at z = 100 m and 100,000 m.

the water of the advection front reaches z = 100 m with very small concentration. However, molecular diffusion soon smooths the steep concentration gradient so that the gradient is eventually controlled by molecular diffusion and decreases with time. Note that before t = 10 yr the gradient obeys the function (4.48) while after t = 10 yr the gradient approaches the value expressed as (4.47).

At z = 100,000 m the concentration keeps increasing after the advection front has passed, and starts decreasing at about t = 300,000 yr. The similar observation can be made for the profile of the gradient at the interface. During the period from 10,000 yr to 300,000 yr, the point $z = 10^5$ m is in the intermediate region which has been observed in region A in case of Figures and 4.3 and 4.4.

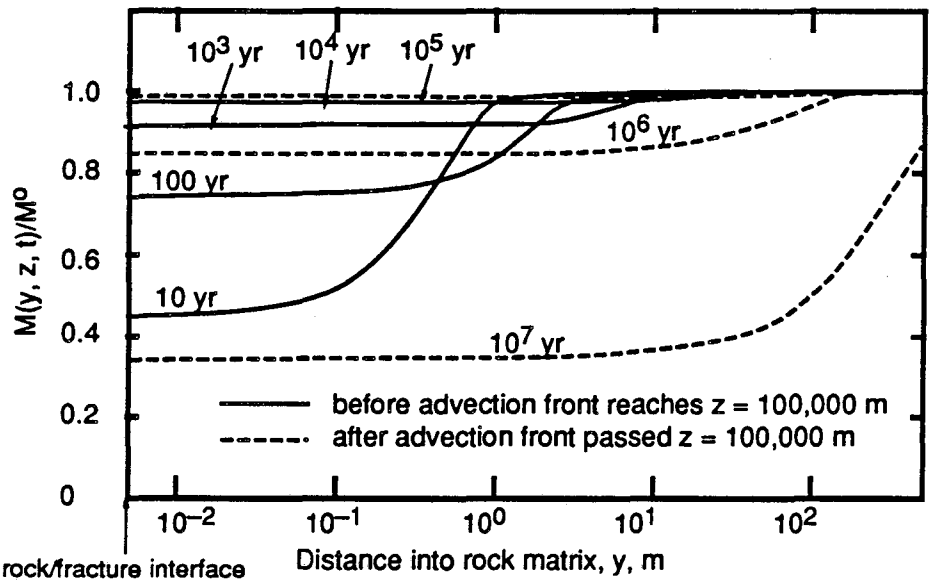

Figure 4.6 Changes in time of the normalized concentration profiles in the rock matrix at z = 100,000 m. The same parameter values as Figure 4.3 apply.

Figure 4.6 depicts the changes in time of the concentration profiles along the y-direction in the rock matrix at z = 100,000 m. The advection front arrives at z = 100,000 m at t = 10,000 yr. At early times including 10 yr and 100 yr the radionuclide existing in the vicinity of the interface diffuses out to the fracture. As time proceeds, the initial steep

gradient becomes gradual, and the effect of back diffusion can be observed in a thicker layer intimate to the interface. By the time when the advection front arrives at z = 100,000 m, the concentration in the rock matrix almost recovers the initial concentration (see the profile for $t = 10^4$ yr). After the advection front passed, the interface concentration keeps increasing (compare the curves for 10^4 yr and 10^5 yr) as observed in Figure 4.5, and then decreases again with time. Note that although the interface concentration increases or decreases with time, the thickness of the layer where the concentration is apparently lower than the initial concentration M^o constantly increases.

We could observe in Figure 4.3 that for the case of a large time the concentration in the water flowing behind the advection front (region A) becomes as much as the concentration of the foregoing advection front, or in Figure 4.5 that for the case of a large z the concentration keeps increasing for a certain time period after the advection front passed that point. These observations imply that the concentration in the water which enters the fracture at later times increases in a different way from the concentration of the water entering at earlier times. To confirm, we will show Figure 4.7, where plotted are the concentration in the fracture and the concentration gradient at the interface expressed in terms of the nuclide travel time T_n and the water entrance time τ:

$$N(T_n, \tau) = M^o e^{-\lambda(\tau + T_n)} \left\{ 1 - H\left(\frac{\sqrt{\tau + T_n}}{A} \right) - exp\left(-\frac{T_n^2}{4A^2\tau} \right) \right.$$

$$\left. \times \left[H\left(\frac{T_n}{2A\sqrt{\tau}} \right) - H\left(\frac{\sqrt{\tau}}{A} + \frac{T_n}{2A\sqrt{\tau}} \right) \right] \right\}, \qquad (4.49)$$

$$\theta(T_n, \tau) = \frac{B}{A} M^o e^{-\lambda(\tau + T_n)} \left\{ \frac{1}{\sqrt{\pi(\tau + T_n)}} - H\left(\frac{\sqrt{\tau + T_n}}{A} \right) \right.$$

$$+ \exp\left(- \frac{T_n^2}{4A^2\tau} \right) H\left(\frac{\sqrt{\tau}}{A} + \frac{T_n}{2A\sqrt{\tau}} \right) \Bigg\}, \qquad (4.50)$$

where

$$\tau = t - T_n, \qquad T_n = \frac{R_f z}{v}. \qquad (4.51)$$

By this variable exchange, we can now observe the concentration and the gradient while moving along the fracture together with the same water volume. The water entrance time is defined as the real time t subtracted by the nuclide travel time. Therefore the water entrance time is considered as the time when the water entered the fracture first. For example, if τ = 10 yr, then the water with which the observer is moving enters the fracture at 10 years after t = 0.

Figure 4.7 illustrates the profiles of the concentration in the fracture and the concentration gradient at the interface as a function of the nuclide travel time for the water entrance time τ = 0 and 10,000 yr. With the curve for τ = 0 we can observe how the concentration and the gradient inside region B (the region to the right of the advection front) change as the water advances in the fracture, whereas the curve for $\tau = 10^4$ yr inside region A. The gradient for the water τ = 10,000 yr shows a quite different profile from that for the advection front; in the region near the entrance the water which enters the fracture at τ = 10,000 yr feels a uniform gradient, and as the water proceeds, the gradient becomes small suddenly at T_n = 2,000 yr. Finally the gradient becomes close to the gradient of the advection front. The flat profile in the region near the entrance occurs because advective transport is much faster than molecular diffusion. Uncontaminated water makes the concentration in the near-region in the fracture small very quickly compared with the speed with which the diffusion process takes place in the rock matrix.

The concentration increases linearly with the distance transported along the fracture, or the nuclide travel time, because of uniform mass flux in this region, and finally becomes as large as the concentration of the advection front. When the water labeled as $\tau = 10^4$ yr

reaches the point of T_n = 2,000 yr, the advection front exists at T_n = 12,000 yr. The concentrations at the points of T_n = 2,000 yr in $\tau = 10^4$ yr and T_n = 12,000 yr in $\tau = 0$ become very close to each other. Thus the concentration in the water that entered the fracture later becomes the same as that of advection front with smaller nuclide travel time. This is the reason why at later times in Figure 4.3 the plateau region extends into region A.

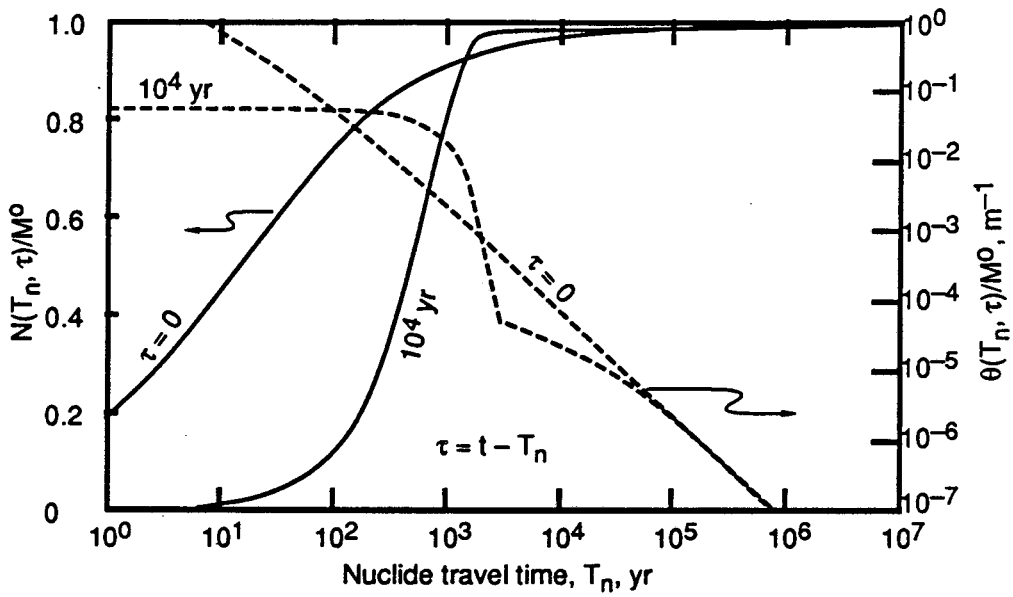

Figure 4.7 Profiles of concentration in the fracture and the concentration gradient at the interface y = b for two sets of the water entrance time. The same parameter values as Figure 4.3 apply. Curves for t = 0 and 104 yr show the changes inside region B (ahead of the advection front) and region A (behind the advection front), respectively.

4.4.3 Observation of Back Diffusion in Fracture-Flow Transport by a Band Release

With the knowledge obtained by the hypothetical model, we now observe transport through a single fracture caused by a band release at the fracture entrance. The model and the mathematical formulation are given in Chapter 2.

Figure 4.8 illustrates the profiles of the concentration of ^{237}Np in the fracture as a function of the downstream distance *z*. Parameter values chosen for this illustration are the

same as in Figure 4.3. The dashed curves stand for the case without matrix diffusion, and the solid curves are for the case with matrix diffusion.

Without matrix diffusion, all the contaminant released into the fracture during the leach time is kept in the fracture except the loss by radioactive decay, and forms a contaminant band in the fracture. This band travels at water velocity because no sorption on the fracture wall is assumed. At 30,000 yr, the front edge of the band reaches 300,000 m, and at 70,000 yr the front edge reaches 700,000 m and the trailing edge at 400,000 m.

With matrix diffusion, at t = 30,000 yr, the concentration in the fracture becomes significantly smaller than that in the case without matrix diffusion as the distance from the origin becomes large. The profile shows that the apparent front of the contaminant moves much more slowly than the advection front. This is because the contaminant is taken away from the fracture to the rock matrix by matrix diffusion.

At t = 30,001 yr, one year after the leach time, uncontaminated water is flowing into the fracture, and the front of the uncontaminated water reaches z = 10 m. What is happening in the fracture is depicted in the bottom diagram of Figure 4.8. Because the concentration in the fracture in region A (the region to the left of the uncontaminated-water front) becomes smaller than the concentration in the rock matrix, the nuclide diffuses out to the fracture. The gradient at the interface of the fracture and the rock matrix, i.e.,

$$\theta(z,\, t) = \frac{B}{\sqrt{\pi}} e^{-\lambda t} \left\{ h(t - ZA - T) \frac{e^{-\frac{z^2}{4(t-ZA-T)}}}{\sqrt{t - ZA - T}} - h(t - ZA) \frac{e^{-\frac{z^2}{4(t-ZA)}}}{\sqrt{t - ZA}} \right\}, \quad (4.52)$$

shows that in the region between z = 0 and z = 10 m the nuclide diffuses out to the fracture while in the region z > 10 m the nuclide diffuses into the rock matrix. At this time, the leading edge of the uncontaminated water, or the edge of region A, coincides with the location where the mass flux reverses its direction. At t = 30,010 yr, the leading eadge is still located at the same point as the reversing point.

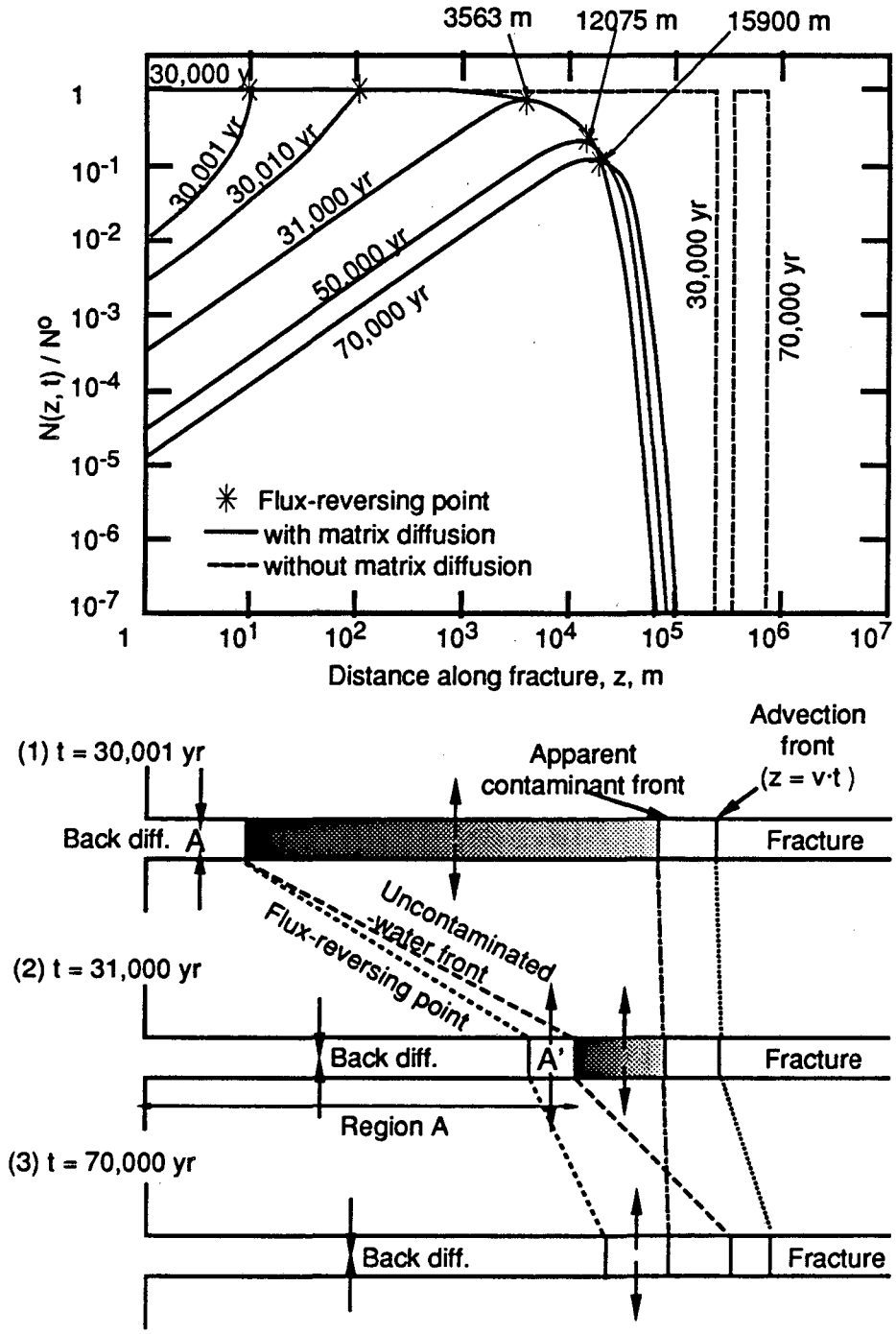

Figure 4.8 Concentration profiles in the fracture for a band release after the leach time, compared with the case without matrix diffusion. The scale of the bottom diagram matches with that of the horizontal axis in the top figure. The same parameter values as Figure 4.3 apply. The regions A and A' in the diagram are explained in the test.

However, at t = 31,000 yr, the region of back diffusion exists in between 0 and 3,563 m, whereas region A extends up to 10,000 m. The discrepancy becomes greater as time proceeds. At t = 50,000 yr, the advection front reaches at $z = 5 \times 10^5$ m while the flux-reversing point is at z = 12,075 m, and at t = 70,000 yr, the advection front is at $z = 7 \times 10^5$ m while the flux-reversing point is at z = 15,900 m.

This discrepancy occurs due to the same mechanism as observed in the hypothetical model, where the advection front does not match the point dividing the plateau region and the increase region in Figure 4.3. Note that in (4.52) there is an exponential factor identical to (4.45), which causes the discrepancy in Figure 4.3. In region A' in the diagram of Figure 4.8 the contaminant is diffusing into the rock although the region is included in region A. This is because the contaminant builds up in the fracture due to back diffusion while being transported along the fracture. For example let us take notice of region A at 30,001 yr in the diagram. The water in region A will be transported to the position near the edge of region A at 31,000 yr. The concentration in region A at 30.001 yr increases by back diffusion, and, by the time when the water in region A reaches about 10,000 m position, becomes larger than the concentration in the adjacent rock. Then, the flux reverses its direction.

At 70,000 yr the advection band of width 300,000 m ranges from 400,000 m to 700,000 m. The apparent contaminated area stays in the region less than 100,000 m. The nuclide in the rock matrix in the small-z region diffuses out to the fracture, flows along the fracture, and then again diffuses into the rock matrix. The nuclide migration along the fracture is, therefore, retarded significantly compared with transport without matrix diffusion, especially at time after the leach time because of this complex transport path.

4.5 Conclusions

To observe back diffusion, we considered a hypothetical model. From the observations of numerical results, we found primarily two regions in the concentration profiles

against the downstream distance z: the near-region where the concentration increases with z and advection is dominant to molecular diffusion, and the far-region where the concentration is independent of z with dominant back diffusion. As time proceeds, we could find an intermediate region between these two regions. Because advective transport is much faster than molecular diffusion by assumption, the sweep-out by the uncontaminated water is predominant against back diffusion in the vicinity of the fracture entrance. However, as the uncontaminated water is transported along the fracture, contamination due to back diffusion accumulates in the fracture water and the concentration becomes the same as that in the far-region. Then, the intermediate region occurs inside the near-region. This region is characterized by the dimensionless factor shown in (4.45)

The intermediate region between the two primary regions could be observed in the single-fracture model with the band release. At time right after the leach time in the entire region of the uncontaminated water the nuclide in the rock matrix diffuses out to the fracture, while beyond the point the nuclides still diffuse into the rock matrix. However as time increases, the point where the gradient at the interface reverses its direction moves much more slowly than the leading edge of the uncontaminated water moves. The discrepancy between the leading edge and the flux-reversing point is also characterized by the dimensionless parameter (4.45). The complex transport path of the nuclide after the leach time retards the nuclide movement significantly.

References

[1] Chambré, P. L., *Notes for Mathematics 220A/B,* Department of Mathematics, University of California, Berkeley, 1984—1985,

[2] Abramowitz, M., and I. A. Stegun, *Handbook of Mathematical Functions with Formulas, Graphs, and Mathematical Tables,* 10th ed., Dover, New York, 1972.

Chapter 5
Radionuclide Migration through a Multiply Fractured Rock

5.1 Introduction

This chapter presents the results of an analytical study of hydrogeological transport of a radioactive contaminant through porous rock with a system of multiple parallel planar fractures. In some instances the contaminant penetrates so deeply into the rock matrix that concentration fields from adjacent fractures overlap, requiring consideration of multiple fractures in predicting contaminant transport.

Sudicky and Frind [1] gave analytical solutions for this problem, assuming zero or non-zero longitudinal dispersion in fractures. Their solutions for concentration in fractures, however, do not satisfy the boundary condition at the fracture entrance, and their solutions for concentration in porous rock do not satisfy the boundary condition at the rock-fracture interface.

Corrected solutions are provided in this chapter. The exact solutions, however, require evaluation of multiple integrals and summation of an infinite series, which converges slowly because of its alternating signs. The convergence of the series becomes slower for strongly sorbing rock, large spacing of two adjacent fractures, and early times. In other words the exact solutions are not suitable for numerical evaluation for the cases of slight overlap of concentration fields from two fractures.

Then, proposed is a simplified analytical method that superposes two single-fracture solutions which have been obtained in Chapter 2. The superposition approximation is valid for the cases of slight overlap. The validity is expressed in terms of Fourier number and the (t, R_p) space. Numerical illustrations are given for the band release.

5.2 Evaluation of Sudicky and Frind's Solutions

The problem of interest in this chapter is the same as what is described in Chapter 2

except that here multiple parallel planar fractures situated in equal spacing are assumed (Figure 5.1). The distance between the centers of two adjacent fractures is assumed to be $2S$. We consider that infinitely many fractures exist so that we can neglect the end effect. Each fracture has the identical property, and the contaminant is released into each fracture in the identical fashion. Then, we may consider a half fracture extending in the region $0 \le y \le b$ and a half rock matrix extending in the region $b \le y \le S$.

The same governing equations as (2.5) and (2.9) linked by (2.11) apply here except that the domain of definition for (2.9) now should be written as $b < y < S$, $z > 0$, and $t > 0$. Also apply the same side conditions as (2.12) to (2.16). Instead of (2.17) we use:

$$\left.\frac{\partial M}{\partial y}\right|_{y=S} = 0, \quad z > 0, t > 0. \tag{5.1}$$

Side condition (5.1) limits the amount of rock surrounding each fracture. For a release mode represented by $\psi(t)$ in (2.14), *Sudicky and Frind* chose a constant concentration boundary condition:

$$N(0, t) = \psi(t) \equiv N^{o} h(t), \qquad t > 0. \tag{5.2}$$

For nomenclature see Chapter 2.

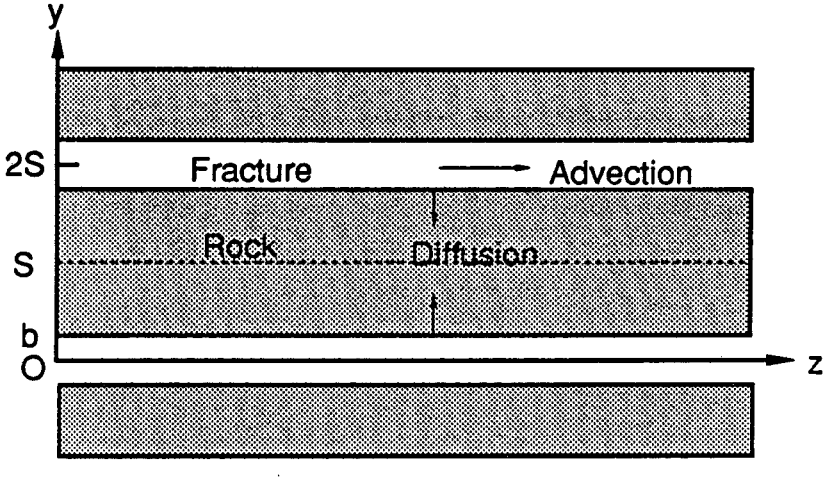

Figure 5.1 Cross-sectional view of system of multiple parallel fractures in porous rock.

They obtained solutions to $N(z, t)$ and $M(y, z, t)$ for zero and non-zero longitudinal dispersion, by making use of Laplace transforms. However, their solutions contain apparently incorrect expressions. We first show the corrected solutions below:

For non-zero D:

$$N(z,\ t)/N^o = \frac{2}{\pi^{3/2}} e^{\alpha z} \int_g^\infty G(\xi;\ z,\ t)\, e^{-\lambda YA} \int_0^\tau e^{-\lambda t'} \int_0^\infty \mu e^{\mu_R} \cos(\mu_g|_{t'}) d\mu dt' d\xi,$$

$$z \geq 0, \qquad t \geq 0, \tag{5.3}$$

$$M(y,\ z,\ t)/N^o = \frac{2}{\pi^{3/2}} e^{\alpha z - \lambda t} \int_g^\infty G(\xi;\ z,\ t) \int_0^\infty \mu e^{\mu_R} \left\{ \frac{\cosh\left(B\sqrt{\lambda}\,(S-y)\right)}{\left(\lambda^2+\mu^4/4\right)\cosh\left(\sigma\sqrt{\lambda}\right)} \right.$$

$$\times \left[\frac{\mu^2}{2} \sin(\mu_g|_\tau) - \lambda \cos(\mu_g|_\tau) + e^{\lambda\tau} \left\{ \frac{\mu^2}{2} \sin(\Omega) + \lambda \cos(\Omega) \right\} \right]$$

$$- 4\pi \sum_{n=0}^\infty \frac{(-1)^n (2n+1)}{(2n+1)^2\pi^2 + 4\lambda\sigma^2} \frac{1}{\omega^2+\mu^4/4} \cos\left(\frac{(2n+1)\pi(S-y)}{2(S-b)} \right) \left[\frac{\mu^2}{2} \sin(\mu_g|_\tau) + \omega \cos(\mu_g|_\tau) \right.$$

$$\left. \left. + e^{-\omega\tau} \left\{ \frac{\mu^2}{2} \sin(\Omega) - \omega \cos(\Omega) \right\} \right] \right\} d\mu d\xi, \qquad b \leq y \leq 2S - b,\ \ z > 0,\ t \geq 0 \tag{5.4}$$

For $D = 0$:

$$N(z,\ t)/N^o = \frac{e^{-\lambda ZA}}{\pi} h(\tau^o) \int_0^{\tau^o} e^{-\lambda t'} \int_0^\infty \mu e^{\mu_R^o} \cos(\mu_g^o|_{t'}) d\mu dt', \quad z \geq 0,\ t \geq 0, \tag{5.5}$$

$$M(y,\ z,\ t)/N^o = \frac{e^{-\lambda ZA}}{\pi} h(\tau^o) \int_0^\infty \mu e^{\mu_R^o} \left\{ \frac{\cosh\left(B\sqrt{\lambda}\,(S-y)\right)}{\left(\lambda^2+\mu^4/4\right)\cosh\left(\sigma\sqrt{\lambda}\right)} \right.$$

$$\times \left[e^{-\lambda\tau^o} \left\{ \frac{\mu^2}{2} \sin(\mu_g^o|_{\tau^o}) - \lambda \cos(\mu_g^o|_{\tau^o}) \right\} + \frac{\mu^2}{2} \sin(\Omega^o) + \lambda \cos(\Omega) \right]$$

$$- 4\pi \sum_{n=0}^\infty \frac{(-1)^n (2n+1)}{(2n+1)^2\pi^2 + 4\lambda\sigma^2} \frac{e^{-\lambda\tau^o}}{\omega^2 + \mu^4/4} \cos\left(\frac{(2n+1)\pi(S-y)}{2(S-b)} \right) \left[\frac{\mu^2}{2} \sin(\mu_g^o|_{\tau^o}) + \omega \cos(\mu_g^o|_{\tau^o}) \right.$$

$$+e^{-\omega\tau^o}\left(\frac{\mu^2}{2}sin(\Omega^o)-\omega cos(\Omega^o)\right)\Bigg]\Bigg\}d\mu,\quad b\le y\le 2S-b,\quad z>0,\ t\ge 0, \qquad (5.6)$$

where

$$\tau = t - YA,\quad \tau^o = t - ZA,$$

$$\mu_R = -\frac{Y}{2}P_1(\mu),\qquad \mu_g = \frac{\mu^2 t}{2}-\frac{Y}{2}P_2(\mu),\qquad \Omega = \frac{Y}{2}P_2(\mu),$$

$$\mu_R^o = -\frac{Z}{2}P_1(\mu),\qquad \mu_g^o = \frac{\mu^2 t}{2}-\frac{Z}{2}P_2(\mu),\qquad \Omega^o = \frac{Z}{2}P_2(\mu),$$

$$P_1(\mu) = \mu\left\{\frac{sinh(\sigma\mu)-sin(\sigma\mu)}{cosh(\sigma\mu)+cos(\sigma\mu)}\right\},\qquad P_2(\mu) = \mu\left\{\frac{sinh(\sigma\mu)+sin(\sigma\mu)}{cosh(\sigma\mu)+cos(\sigma\mu)}\right\},$$

$$\sigma = B(S-b),\qquad g = \frac{z}{2}\sqrt{\frac{R_f}{Dt}},\qquad \omega = \frac{\pi^2(2n+1)^2}{4\sigma^2}. \qquad (5.7)$$

Definitions for A, α, β^2, Y, Z, and B are given in Chapter 2. $G(\xi; z, t)$ is defined by (2.36). The errors committed in *Sudicky and Frind*'s solutions are explained in Appendix C.

In these correct solutions the multiple integrals and the infinite series must be evaluated numerically. The alternating series converges very slowly especially for strongly-sorbing rock (large R_p), large spacing of two fractures and early times. This could be one of the reasons why they have not shown any numerical results for $M(y, z, t)$.

5.3 Superposition Approximation for Parallel Fracture System

5.3.1 Formulation

Solutions for a single fracture have been derived in Chapter 2 based upon the assumption that the fracture spacing is such that there is no overlap of two concentration fields produced by the adjacent fractures. If the contaminant penetrates so deeply into the rock matrix that concentration from adjacent fractures overlap, consideration of multiple

fractures is required. However, the single-fracture solutions are applicable if the overlap is acceptably small.

In Figure 5.2(a), virtually no overlap is observed. This is the situation considered in the single-fracture model. In Figure 5.2(b) moderate overlap is observed inside the rock matrix, but there is no, or negligibly small influence observed at the neighboring fractures. In such a situation the single-fracture solutions still satisfy the boundary condition (2.16) at the rock-fracture interface with negligible errors. The concentration in the fracture may be calculated by the single-fracture solutions exactly in case of Figure 5.2(a) and approximately in case of Figure 5.2(b). For the concentration in the rock matrix we can use the single-fracture solutions for Figure 5.2(a), while we cannot for the case of Figure 5.2(b). However, in the latter case we can approximate the concentration in the rock by superposing two single-fracture solutions. As the overlap develops, significant amount of contaminant penetrates to the adjacent fractures so that superposition approximation fails (Figure 5.2(c)). In this case we must use the exact solutions (5.3) to (5.6). The alternating series converges so fast that using the exact solutions might be affordable. Thus by superposition approximation we can extend the applicability of the single-fracture solution.

Denoting the single-fracture solution for concentration in the rock matrix as $M(y, z, t)$ and the superposed solution as $M_s(y, z, t)$, we can write $M_s(y, z, t)$ as

$$M_s(y, z, t) = M(y, z, t) + M(2S - y, z, t), \quad b \le y \le 2S - b, z > 0, \quad t \ge 0, \qquad (5.8)$$

We impose the condition for a valid superposition based on the argument with Figure 5.2 as

$$\frac{M(2S - b, z, t)}{M(b, z, t)} \le 0.01, \qquad (5.9)$$

so that the influence of the concentration field by the neighboring fracture is less than one percent of the concentration produced by the fracture of interest (Figure 5.3). One percent-criterion is set arbitrarily. Then the boundary condition at the interface can be satisfied by

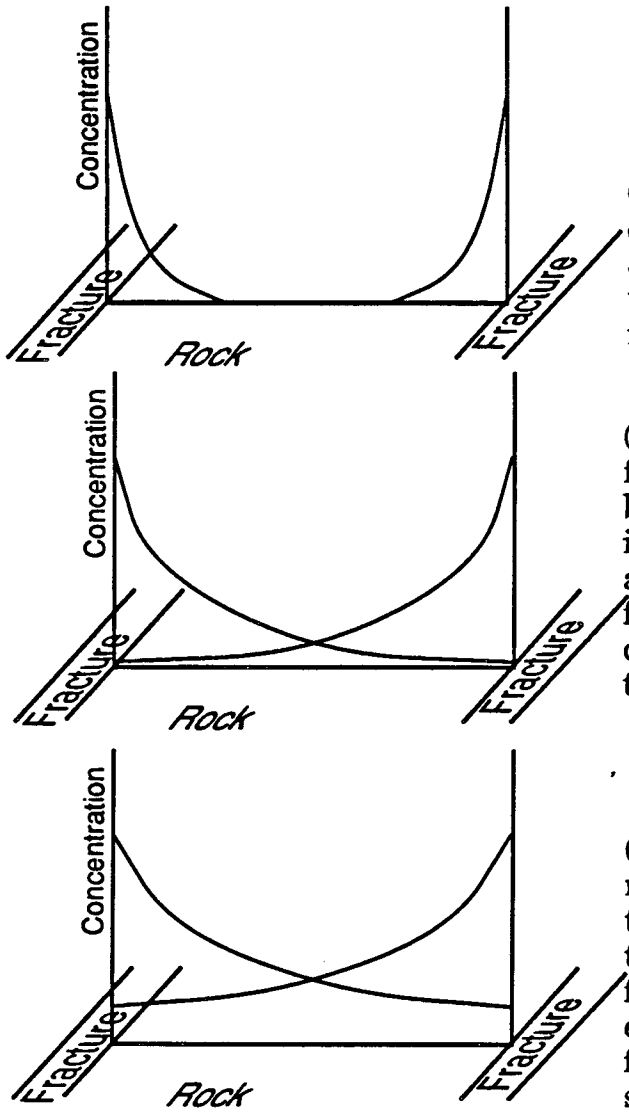

(a) Overlap is negligible. Single-fracture model applies for both concentrations in fractures and rock.

(b) Influence of adjacent fractures is still negligibly small. Concentration in fractures is still well approximated by single-fracture solutions. Concentration in rock is obtained by superposition.

(c) Significant amount of nuclides penetrates to the adjacent fractures so that concentration in fractures is no longer expressed with single-fracture solutions. Exact solutions must be used.

Figure 5.2 Effect of neighboring fractures

the single-fracture solution within one percent accuracy.

Let us consider constraint (5.9) in terms of the Fourier number:

$$F = \frac{D_p}{R_p} \frac{t}{(2S)^2} . \qquad (5.10)$$

The Fourier number measures the time in which the diffusion process is continuing. A large Fourier number means that the long time has passed since the diffusion process started. Hence, the diffusion front has penetrated deeply into the medium. Since the valid

superposition can be interpreted as shallow penetration by diffusion, we should be able to find an upper bound of the Fourier number for a valid superposition. We can survey the range of the Fourier number, where (5.9) is satisfied, by changing t and R_p, fixing the values of D_p and S. The validity domain in (t, R_p) space can be expressed by an inequality for t/R_p:

$$t/R_p \leq C, \tag{5.11}$$

where C is a constant obtained from numerical evaluations. Then the condition for the Fourier number is obtained as:

$$F \leq \frac{D_p}{(2S)^2} C. \tag{5.12}$$

To illustrate, we consider the band release for the boundary concentration at $z = 0$ in each fracture. Based on the argument in Chapter 3 we do not include longitudinal dispersion; instead we take large values for fracture width and velocity. Then the concentration $M(y, z, t)$ is expressed as (2.61).

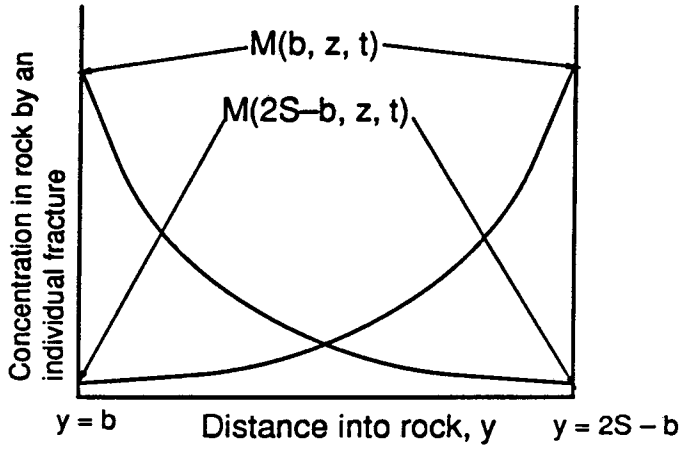

Figure 5.3 Illustration of constraint on valid superposition. Constraint is imposed so that M(2S–b, z, t) becomes one percent of M(b, z, t).

5.3.2 Validity of Superposition Approximation

The inequality (5.9) is checked at z = 1, 100 and 10,000 m for various (t, R_p) points with the common parameter values shown in Figure 5.4. Although ^{237}Np is chosen for illustration, Figure 5.4 would be the same for any radionuclide because the factor $\exp(-\lambda t)$ in the single-fracture solution (2.61) cancels when substituted into (5.9). For different boundary conditions the validity-domain graph would be different from Figure 5.4.

In Figure 5.4 superposition is valid to the left of each line. The dashed line shows the line dividing the valid and invalid regions for the time before the end of the leach time. Here T = 30,000 yr is assumed. After the leach time there is a transition from the dashed line to the solid line; thereafter the constraints on t and R_p are more limited. For large z this change becomes smaller, and at z = 10,000 m the stepwise change disappears. At z = 10,000 m, the leach time does not affect the validity domain. From Figure 5.4 the constant C in (5.11) and the upper bound of the Fourier number are obtained as Table 5.1. Different upper bound of the Fourier number will be obtained for different R_f values. One can see the advantage of the superposition method from this figure. In early time region, where the exact solutions are difficult to evaluate, the approximation is valid regardless of R_p values.

Table 5.1 Constant C and the constraint on the Fourier number for valid superposition

Time	z = 1 m	z = 100 m	z = 10,000 m
t < T	C = 3000 yr → $F \le 0.075$		C=8000yr → $F \le 0.2$
t > T	C = 800 yr → $F \le 0.02$	C = 1300 yr → $F \le 0.033$	C=8000yr → $F \le 0.2$

The reason why there is no stepwise change at the end of the leach time in the region far from the fracture entrance is explained by the observation on back diffusion. After the leach time the contaminant diffuses back to the fractures in the near region including z = 1 and 100 m. In the far region including 10,000 m, however, the concentration in the fractures is still larger than in rock matrix. From Figures 2.7 and 4.8 in case of R_p = 1 and R_f = 1 the direction of mass flux at the rock-fracture interface reverses at z = 12,075 m at

50,000 yr. As the pore retardation increases, the flux reversing point shifts to smaller z. For $R_p = 100$, it is located at 1,616 m. Thus, because the contaminant is always diffusing into the rock matrix, i.e., there is no change in migration behaviour before and after the leach time, there does not occur the stepwise change.

The limit line for 10,000 m is located to the right even before the leach time compared with those for smaller z. Because diffusion starts after the contaminant reaches the location $z = 10{,}000$ m in the fracture, there is larger time lag at large z.

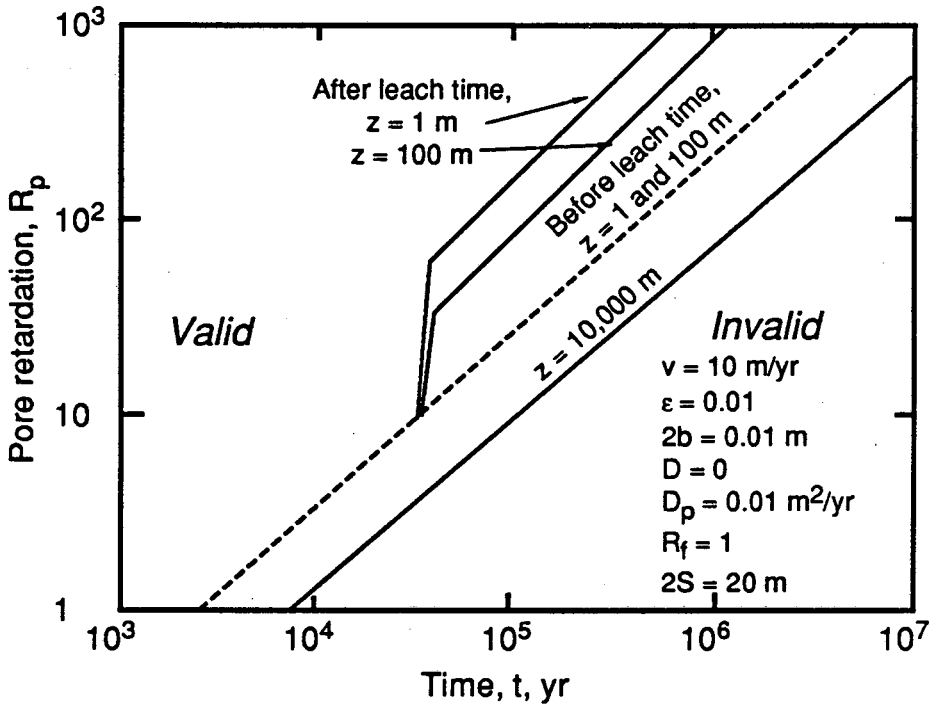

Figure 5.4 Validity domain for superposed solutions. Each line is the divider of the valid and invalid domains. For z = 1 and 100 m, superposition is valid to the left of the dashed line before the leach time. If the leach time is assumed to be 30,000 yr, the divider shifts upward at 30,000 yr. For z = 10,000 m, no shift is observed before and after the leach time.

We can confirm the observation in Figure 5.4 by calculating the actual concentration profiles in the rock matrix for various combinations of t and R_p. In Table 5.2 summarized are the calculation conditions and the validities of the resultant profiles, which are judged by Figure 5.4.

Table 5.2 Calculation conditions and Validity of resultant profiles

Figure	Distance z, m	Leach time T, yr	R_p	Time t, yr	VALID/ NOT VALID
5.5	100	$> 10^6$	100	1×10^4	VALID
				6×10^4	VALID
				2×10^5	VALID*
				1×10^6	NOT VALID
5.6	100	3×10^4	100	1×10^4	VALID
				6×10^4	VALID
				2×10^5	NOT VALID*
				1×10^6	NOT VALID
5.7	100	$3 \times 10^4 / > 1 \times 10^5$	2	2×10^3	VALID
		$3 \times 10^4 / > 1 \times 10^5$		1×10^4	NOT VALID
		$> 1 \times 10^5$		1×10^5	NOT VALID
		3×10^4		1×10^5	NOT VALID

* These two show that the constraint for valid superposition is more limited after the leach time than before the leach time.

Figure 5.5 shows the calculated concentration profiles for $z = 100$ m, provided that the leach time is larger than a million years. Figure 5.4 indicates that for $R_p = 100$, the three early-time profiles yield valid superposition. Actually these three show shallow penetration into rock matrix, while at $t = 10^6$ yr the overlap is considerable, resulting in invalid superposition.

In Figure 5.6 the same time points and the pore retardation factor in the previous figure are assumed, but here the leach time is as small as 30,000 yr. As can be deduced from Figure 5.4, with $R_p = 100$ the superposition is valid if $t = 2 \times 10^5$ yr is before the leach time (Figure 5.5), but invalid if it is after the leach time (Figure 5.6). After the leach time uncontaminated water enters the fractures, and so the concentration profile in the rock originated by each fracture has a maximum along the y-axis. Because the denominator of the condition (5.9) becomes smaller after the leach time, it becomes more difficult to meet the condition, and the upper bound of the Fourier number becomes smaller. Two early time profiles in Figure 5.6 show valid superposition. At 60,000 yr, greater than the leach

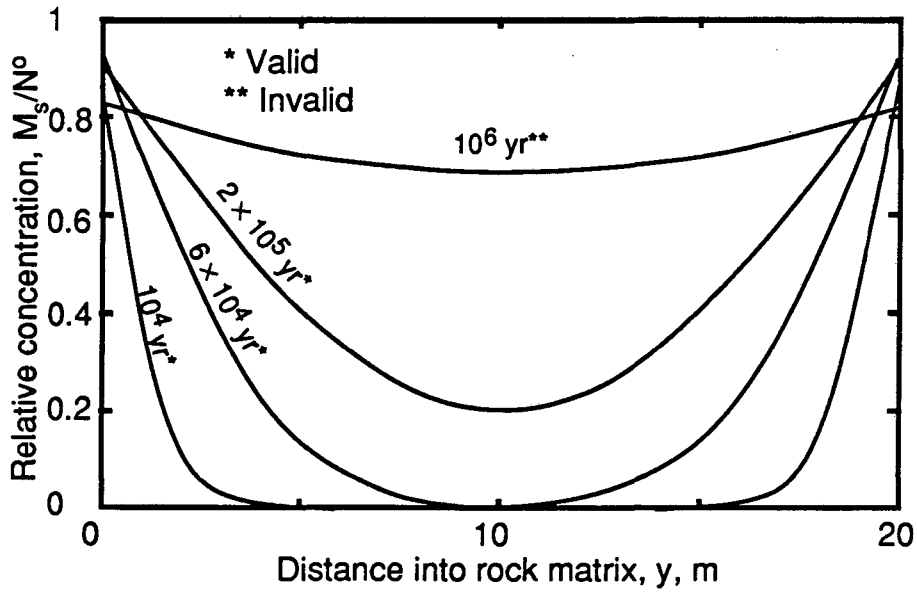

Figure 5.5 Concentration profiles in the rock matrix 100 m far from the source, normalized by the initial concentration at the source, N^o. Pore retardation is assumed to be 100. Leach time is considered to be longer than the times shown in the figure.

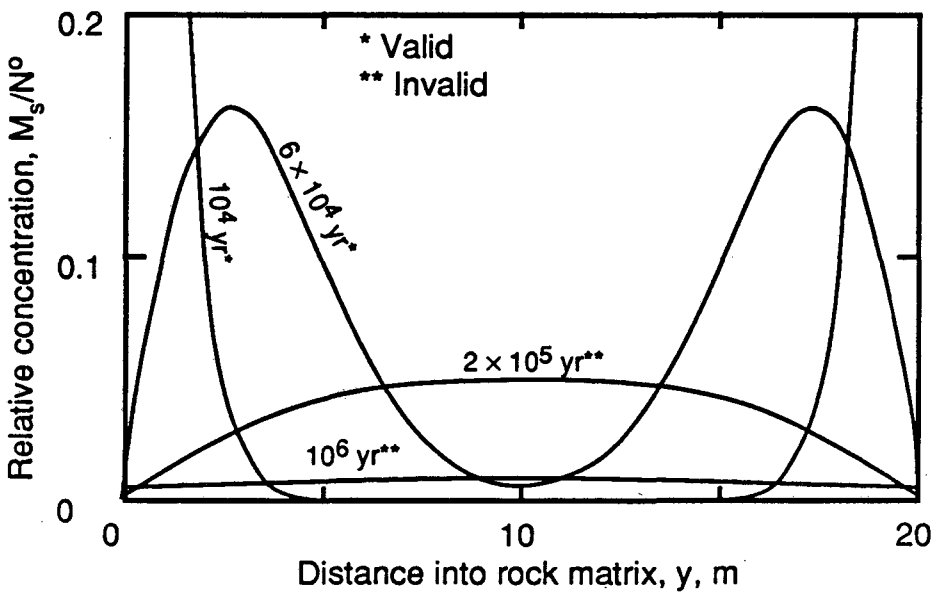

Figure 5.6 Same as Figure 5.5 except that the leach time is assumed to be 30,000 yr.

time, the superposed profile shows two peaks along y-axis. Two concentration fields originated by diffusion from two adjacent fractures are about to overlap at the midpoint, y = 10 m. Two later profiles show invalid superposition, where diffusion from each fracture has continued for such a long time that diffusion front exceeds the adjacent fracture location. As a result we no longer observe two-peak profiles as that observed at 60,000 yr.

Figure 5.7 shows the concentration profiles at z = 100 m for a smaller pore retardation than Figure 5.6. Two leach times are assumed here: T = 30,000 yr and T greater than 100,000 yr. For both leach times two early time profiles are identical, because these times are both before the leach time. The superposition becomes invalid even before the leach time (10,000 yr). At 10,000 yr for the leach time greater than 10,000 yr, the concentration at the interface is significantly higher than unity, meaning immediately invalid superposition because the maximum possible concentration is unity. For the leach time of 30,000 yr, we observe a single peak profile, which means invalid superposition.

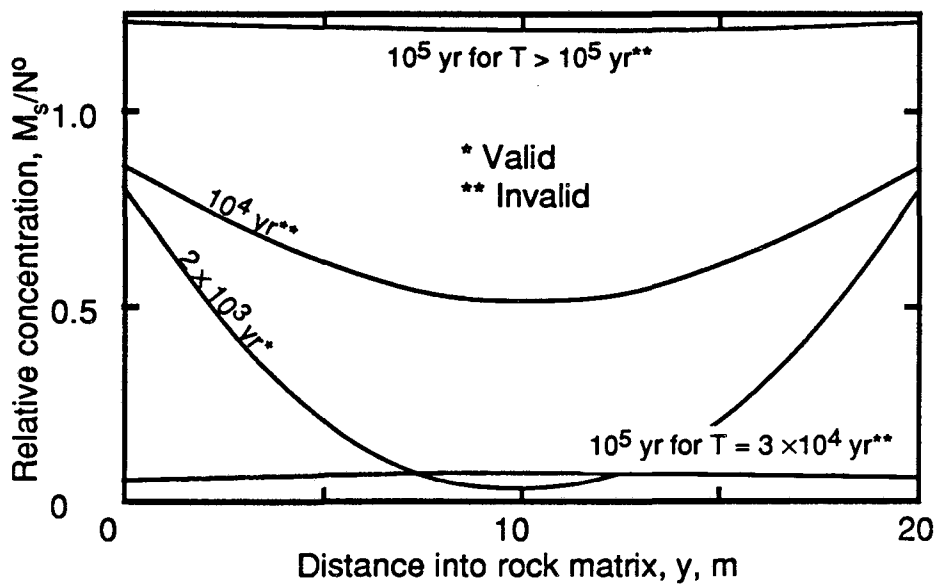

Figure 5.7 Concentration profiles in the rock matrix 100 m far from the source for pore retardation of 2. Two leach times are assumed here: 30,000 yr and > 100,000 yr. Two early-time profiles are identical for both leach times.

5.4 Conclusions

Analytical solutions for a system of multiple planar parallel fractures obtained by Sudicky and Frind have been found incorrect. The corrected solutions have been given. The exact solutions, however, require multiple integrations and a summation of infinite series, whose convergence is slow in case of shallow penetration into rock matrix by diffusion. Approximate solution by superposing two single-fracture solutions have been proposed, and found to give fairly good approximation in case of shallow penetration. Validity of approximation has been expressed by showing the upper bound of the Fourier number for the band release.

Validity is affected by whether the observation time is before or after the leach time and how far the observation point is from the source. Validity becomes more limited after the leach time than before and in the near region than in the far region. Radioactive decay does not affect the validity because of a band release and the chosen constraint for the validity.

From the present analysis it is found that the single-fracture solution is still applicable for the case that the neighboring fractures affect each other moderately.

Reference

[1] Sudicky, E. A., and E. O. Frind, Contaminant Transport in Fractured Porous Media: Analytical Solution for a System of Parallel Fractures, *Water Resources Res., 18,* 1634, 1982.

Chapter 6
Transport of a Two-Member Decay Chain Through Fractured Porous Rock

6.1 Introduction

Neglecting radioactive-decay precursors affects in two ways. First, total amount of a daughter radionuclide in the source and in the medium would be underestimated, which results in underestimate of maximum concentration. Second, if the daughter nuclide is strongly sorbed in the medium and the mother nuclide is assumed not to be present, one might expect that the contaminated area is limited in the region near the source. However, if the mother is transported faster, the daughter would exist in a more extended region than expected because the daughter is generated in the medium.

Transport of a multiple-member chain through a single fracture has been considered by *Chambré et al.* [1] and *Sudicky and Frind* [2]. In [1] an analytical solution is given for a decay chain of arbitrary length in a recursive form. An analytical solution in a recursive form is not suitable for numerical evaluation because it requires increasingly intensive computation for higher members in a chain. They, instead, introduced an approximation that neglects decay in the rock matrix to obtain a non-recursive solution, and showed numerical illustrations for $^{237}Np \rightarrow {}^{233}U \rightarrow {}^{229}Th \rightarrow$ and $^{234}U \rightarrow {}^{230}Th \rightarrow {}^{226}Ra \rightarrow$ chains. This approximation is not tested for the concentration of the daughter nuclides, however. *Sudicky and Frind* obtained non-recursive analytical solutions for a two-member chain with an instantaneous release at the fracture entrance. Although their solutions contain several incorrect expressions, we can utilize their solutions as the Green's functions for the boundary conditions prescribed by an arbitrary function of time after correction of these errors. We can write a corresponding analytical solution by a form of a convolution integral of the Green's function and the prescribed function for the boundary condition.

In this chapter the Green's function obtained from the Sudicky and Frind's solution is given. Numerical results are shown for the band-release boundary condition, and compared with the numerical results from [1]. Approximation of neglecting radioactive decay in rock matrix will be tested by this comparison. In the previous chapters ^{237}Np is considered as a mother nuclide. Actually this radionuclide is also a daughter of ^{241}Am. Effect of the presence of ^{241}Am in the initial inventory in the source is illuistrated by comparison of results from a two-member calculation with results from a single-member calculation.

6.2 Theoretical Development

We will extend the model described in Chapter 2 to a two-member chain. Longitudinal dispersion in a fracture is neglected. The governing equations are:

$$R_{f_1}\frac{\partial N_1}{\partial t} + v\frac{\partial N_1}{\partial z} + \lambda_1 R_{f_1} N_1 + \frac{q_1}{b} = 0, \qquad z > 0,\ t > 0, \tag{6.1}$$

$$R_{f_2}\frac{\partial N_2}{\partial t} + v\frac{\partial N_2}{\partial z} + \lambda_2 R_{f_2} N_2 - \lambda_1 R_{f_1} N_1 + \frac{q_2}{b} = 0, \quad z > 0,\ t > 0, \tag{6.2}$$

$$R_{p_1}\frac{\partial M_1}{\partial t} - D_{p_1}\frac{\partial^2 M_1}{\partial y^2} + \lambda_1 R_{p_1} M_1 = 0, \quad y > b, z > 0,\ t > 0, \tag{6.3}$$

$$R_{p_2}\frac{\partial M_2}{\partial t} - D_{p_2}\frac{\partial^2 M_2}{\partial y^2} + \lambda_2 R_{p_2} M_2 - \lambda_1 R_{p_1} M_1 = 0, \quad y > b, z > 0,\ t > 0. \tag{6.4}$$

Nomenclatures are given in Chapter 2. Subscripts 1 and 2 stand for mother and daughter nuclides, respectively. $q_i(z, t), i = 1, 2$ are defined as:

$$q_i(z, t) = -\varepsilon D_{p_i}\left.\frac{\partial M_i}{\partial y}\right|_{y=b}, \quad z > 0,\ t > 0,\ i = 1, 2. \tag{6.5}$$

Side conditions are given as follows:

$$N_i(z, 0) = 0, \qquad z > 0, \tag{6.6}$$

$$M_i(y, z, 0) = 0, \qquad y > b, z > 0, \tag{6.7}$$

$$N_i(0, t) = \psi_i(t), \qquad t > 0, \tag{6.8}$$

$$N_i(\infty, t) = 0, \qquad t > 0, \tag{6.9}$$

$$M_i(b, z, t) = N_i(z, t), \qquad z > 0, t > 0, \tag{6.10}$$

$$M_i(\infty, z, t) = 0, \qquad z > 0, t > 0, \tag{6.11}$$

where $i = 1, 2$.

Sudicky and Frind [2] solved the problem by taking

$$N_i(0, t) = \psi_i(t) = S_i^o \, \delta(t - 0), \qquad t > 0, \tag{6.12}$$

where S_i^o, $i = 1, 2$ are the strengths of the impulse for nuclide i at the repository at $t = 0$ and $\delta(t)$ is a Dirac's delta function. The solution is written as follows:

$$N_1(z, t) = S_1^o \, W_1(b, z, t), \quad z \geq 0, \; t \geq 0, \tag{6.13}$$

$$M_1(y, z, t) = S_1^o \, W_1(y, z, t), \quad z > 0, \; y \geq b, \; t \geq 0, \tag{6.14}$$

$$N_2(z, t) = S_1^o \, U_2(b, z, t) + S_2^o \, W_2(b, z, t), \quad z \geq 0, \; t \geq 0, \tag{6.15}$$

$$M_2(y, z, t) = S_1^o \left\{ U_1(y, z, t) + U_2(y, z, t) \right\} + S_2^o \, W_2(y, z, t), \quad z > 0, \; y \geq b, \; t \geq 0, \tag{6.16}$$

where

$$W_i(y, z, t) = h(t - Z_i A_i) \left\{ Z_i + B_i(y-b) \right\} E_i(t - Z_i A_i, \, Z_i + B_i(y-b)) \, e^{-\lambda_i Z_i A_i}, \; i = 1, 2 \tag{6.17}$$

$U_1(y, z, t)$ has three different forms depending on the parameter values:

$$U_1(y, z, t) = \frac{\lambda_1 R_{p_1}}{2 D_{p_2} (B_2^2 - B_1^2)} \left\{ h(t - Z_1 A_1) e^{-\lambda_1 t + \sigma(t - Z_1 A_1)} \right.$$

$$\left[e^{-\sqrt{\sigma}\{Z_1 + B_1(y-b)\}} \, erfc\left(\frac{Z_1 + B_1(y-b)}{2\sqrt{t - Z_1 A_1}} - \sqrt{\sigma(t - Z_1 A_1)} \right) + e^{\sqrt{\sigma}\{Z_1 + B_1(y-b)\}} \, erfc\left(\frac{Z_1 + B_1(y-b)}{2\sqrt{t - Z_1 A_1}} \right. \right.$$

$$\left. \left. + \sqrt{\sigma(t - Z_1 A_1)} \right) \right] - \frac{B_2(y-b)}{2} \, h(t - Z_1 A_1) \int_0^{t - Z_1 A_1} E_2(u, B_2(y-b)) \, e^{-\lambda_1 (t-u) + \sigma(t - Z_1 A_1 - u)}$$

$$\left[e^{-\sqrt{\sigma} Z_1} \, erfc\left(\frac{Z_1}{2\sqrt{t - Z_1 A_1 - u}} - \sqrt{\sigma(t - Z_1 A_1 - u)} \right) + e^{\sqrt{\sigma} Z_1} \, erfc\left(\frac{Z_1}{2\sqrt{t - Z_1 A_1 - u}} \right. \right.$$

$$+\sqrt{\sigma(t-Z_1A_1-u)}\Big)\Big]du\Big\},\ y \geq b, for\ B_1^2 \neq B_2^2, \qquad (6.18)$$

$$U_1(y,z,t) = \frac{\lambda_1 D_{p_1}}{D_{p_2}(\lambda_2-\lambda_1)}\Big[W_1(y,z,t) - Z_1B_1(y-b)\,h(t-Z_1A_1)\int_0^{t-Z_1A_1} E_2(u, B_1(y-b))$$

$$E_1(t-Z_1A_1-u, Z_1)\,e^{-\lambda_1 Z_1 A_1}du\Big],\ y \geq b,\ for\ B_1^2 = B_2^2\ and\ \lambda_1 \neq \lambda_2, \qquad (6.19)$$

$$U_1(y,z,t) = \lambda_1 B_1(y-b)\frac{D_{p_1}}{D_{p_2}}h(t-Z_1A_1)\,(t-Z_1A_1)E_1(t-Z_1A_1, Z_1+B_1(y-b))e^{-\lambda_1 Z_1 A_1},$$

$$y \geq b, for\ B_1^2 = B_2^2\ and\ \lambda_1 = \lambda_2, \qquad (6.20)$$

and

$$U_2(y,z,t) = \lambda_1\gamma_2\int_0^z exp\left(-\frac{\lambda_1 R_{f_1}(z-\xi)}{v} - \frac{\lambda_2 R_{f_2}\xi}{v}\right)h(t-\zeta)\int_0^{t-\zeta} E_1(u, \gamma_1(z-\xi))$$

$$E_2(t-u-\zeta, \gamma_2\xi+B_2(y-b))\,F(\xi,u;y,z,t)dud\xi. \qquad (6.21)$$

Here the parameters and functions used in $U_i(y, z, t)$ and $W_i(y, z, t)$ are defined as follows:

$$E_i(u,k) = \frac{1}{2\sqrt{\pi u^3}}e^{-\frac{k^2}{4u}-\lambda_i u},\ i = 1, 2 \qquad (6.22)$$

$$F(\xi,u;y,z,t) = \frac{R_{f_1}\gamma_1\{\gamma_2\xi+B_2(y-b)\}(z-\xi)}{v\gamma_2} + \frac{R_{p_1}}{\sqrt{R_{p_2}D_{p_2}}}$$

$$\left[\frac{\gamma_2 B_2(z-\xi) + B_1\{\gamma_2\xi+B_2(y-b)\}}{2\Phi} - \frac{B_1B_2\Theta}{4\Phi^2} + \sqrt{\frac{\pi}{\Phi}}\,e^{\frac{\Theta^2}{4\Phi}}erfc\left(\frac{\Theta}{2\sqrt{\Phi}}\right)\right.$$

$$\left.\left\{\frac{\gamma_1\{\gamma_2\xi+B_2(y-b)\}(z-\xi)}{2} - \frac{\Theta\left[\gamma_1 B_2(z-\xi)+B_1\{\gamma_2\xi+B_2(y-b)\}\right]}{4\Phi} + \frac{B_1B_2\left(\frac{\Theta^2}{2}+\Phi\right)}{4\Phi^2}\right\}\right] \qquad (6.23)$$

$$\gamma_i = \frac{\varepsilon}{bv}\sqrt{D_{p_i}R_{p_i}}, \quad Z_i = \frac{R_{f_i}z}{vA_i}, \quad A_i = \frac{bR_{f_i}}{\varepsilon\sqrt{D_{p_i}R_{p_i}}}, \quad B_i = \sqrt{\frac{R_{p_i}}{D_{p_i}}}, \; i = 1, 2 \tag{6.24}$$

$$\zeta = \frac{R_{f_1}(z-\xi)}{v} + \frac{R_{f_2}\xi}{v}, \quad \Theta = \frac{\gamma_1 B_1(z-\xi)}{2u} + \frac{\left[\gamma_2\xi + B_2(y-b)\right]B_2}{2(t-u-\zeta)}, \tag{6.25}$$

$$\Phi = \frac{B_1^2}{4u} + \frac{B_2^2}{4(t-u-\zeta)}, \quad \sigma = \lambda_1 + \frac{B_1^2\lambda_1 - B_2^2\lambda_2}{B_2^2 - B_1^2}. \tag{6.26}$$

If the boundary condition at $z = 0$ is prescribed by a function $\psi_i(t)$, $t > 0$ as (6.8), the corresponding analytical solution can be written by applying the convolution theorem with respect to time as:

$$N_1(z, t) = \int_0^t \psi_1(t-\tau)W_1(b, z, \tau)d\tau, \quad z \geq 0, \; t \geq 0, \tag{6.27}$$

$$M_1(y, z, t) = \int_0^t \psi_1(t-\tau)\, W_1(y, z, \tau)d\tau, \quad y \geq b, \; z \geq 0, \; t \geq 0, \tag{6.28}$$

$$N_2(z, t) = \int_0^t \psi_1(t-\tau)U_2(b, z, \tau)d\tau + \int_0^t \psi_2(t-\tau)W_2(b, z, \tau)d\tau, \; z \geq 0, \quad t \geq 0, \tag{6.29}$$

$$M_2(y, z, t) = \int_0^t \psi_1(t-\tau)\Big\{U_1(y, z, \tau) + U_2(y, z, \tau)\Big\}d\tau + \int_0^t \psi_2(t-\tau)W_2(y, z, \tau)d\tau,$$

$$y \geq b, \; z \geq 0, \; t \geq 0 \tag{6.30}$$

To illustrate, we take the band release for a two-member chain. The prescribed functions $\psi_i(t)$, $i = 1, 2$, are obtained from the Bateman equation [3] as follows:

$$\psi_1(t) = N_1^o e^{-\lambda_1 t}\big\{h(t) - h(t-T)\big\}, \quad t \geq 0, \tag{6.31}$$

$$\psi_2(t) = \left[N_2^o e^{-\lambda_2 t} + \frac{N_1^o\lambda_1}{\lambda_2 - \lambda_1}\left(e^{-\lambda_1 t} - e^{-\lambda_2 t}\right)\right]\big\{h(t) - h(t-T)\big\}, \quad t \geq 0, \tag{6.32}$$

where N_i^o, $i = 1, 2$ are the initial concentrations in the water at $z = 0$.

From the standpoint of numerical evaluation there are two major difficulties in the above solutions: to evaluate the triple integral in $N_2(z, t)$ and to evaluate the complementary error function for a complex argument, which occurs in $U_1(y, z, t)$ in case of $\lambda_1 < \lambda_2$. In the next section numerical evaluations are given for the concentration in the fracture because of its primary importance. So the latter difficulty is avoided. For the former difficulty two package subroutines from NAG library [4] are used: D01DAF for two-dimensional integration and D01AJF for one-dimensional integration. D01DAF is used for the evaluation of the U_2 function.

6.3 Numerical Illustrations

6.3.1 Effect of Radioactive Decay Chain in Rock Matrix

We compare the results obtained by approximation in [1] with the results from the exact solutions obtained from (6.1) to (6.5). In the approximation, radioactive decay in the rock matrix is neglected; the third term in (6.3) and the third and fourth terms in (6.4) are not included.

Figures 6.1 and 6.2 compare the both models. In Figure 6.1 profiles of concentration in the fracture for a chain, $^{237}Np \rightarrow {}^{233}U \rightarrow$, at 10,000 yr and 50,000 yr are plotted. The dashed curves stand for approximated solution. It is assumed that initially only ^{237}Np exists in the repository. Retardation factors due to sorption on the fracture surfaces are unity for both nuclides. Pore retardation for ^{233}U is set 150 times greater than that for ^{237}Np. Therefore, the mother is transported faster than the daughter.

For the mother, the approximate solution shows good agreement with the exact solution both at 10,000 yr and 50,000 yr. For the daughter, however, the approximate solution underestimates the concentration in the fracture. Especially in the ranges of 100 to 1,000 m at 10,000 yr and 600 to 3,000 m at 50,000 yr, the difference is more than two

orders of magnitude. The neglected terms in (6.4), $\lambda_2 R_{p2} M_2 - \lambda_1 R_{p1} M_1$, would have given the negative contribution to the governing equation (6.4) at the far field for the parameter values shown in the caption of Figure 6.1. The orders of M_1 and M_2 can be roughly estimated from those of N_1 and N_2 in the figure. M_1 is about 10^4 times larger

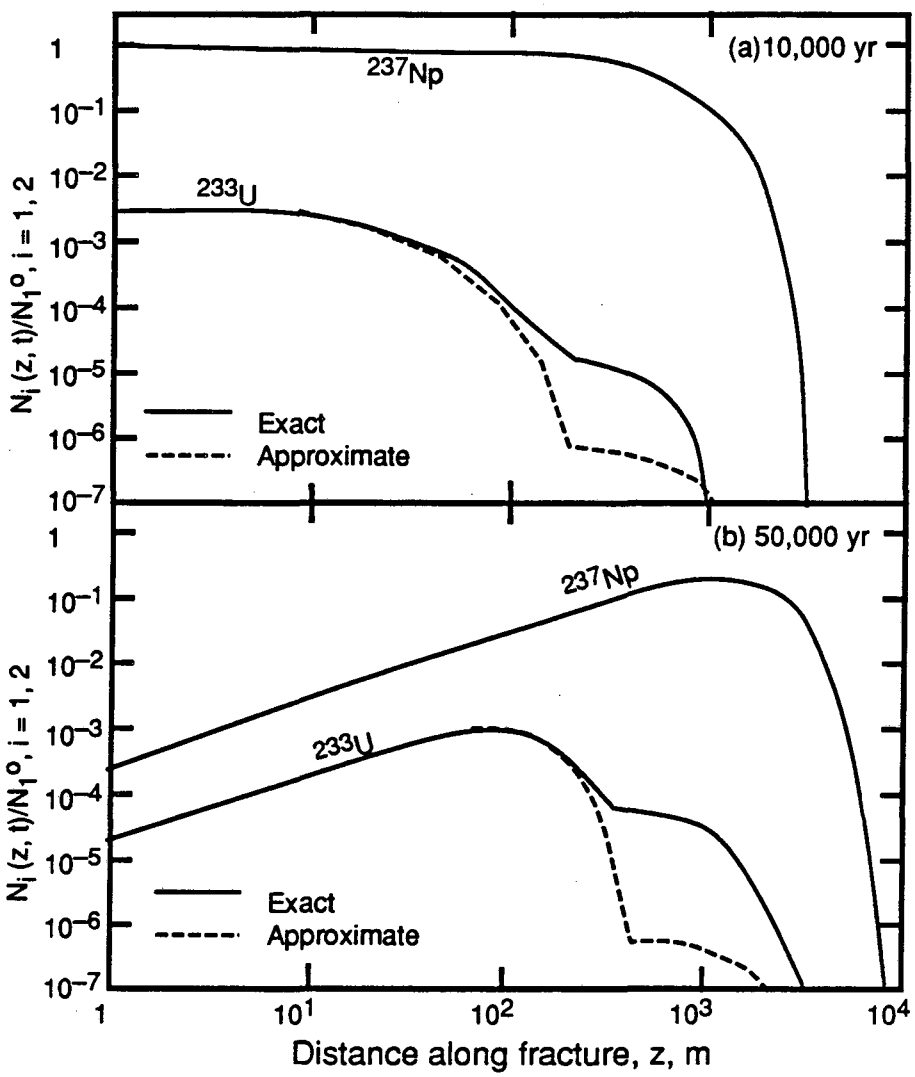

Figure 6.1 Concentration profiles of a $^{237}Np \rightarrow {}^{233}U \rightarrow$ chain. Approximate solution from Ref. [1] is compared with the exact solution. Assumed parameter values are the following: $v = 10$ m/yr, $\varepsilon = 0.01$, $2b = 1$ cm, $N^o_{237} = 1$, $N^o_{233} = 0$, $R_{f237} = R_{f233} = 1$, $R_{p237} = 100$, $R_{p233} = 15{,}000$, $D_{p237} = D_{p233} = 0.01$ m^2/yr.

than M_2 in the ranges of 300 to 1,000 m for 10,000 yr and 600 to 3,000 m for 50,000 yr. Therefore, neglecting the decay chain in the rock matrix makes the concentration in the rock matrix lower, resulting in the overestimate of concentration gradient and diffusive flux at the rock-fracture interface. Thus the uranium concentration in the fracture becomes underestimated.

There observed are two regions in the profiles of uranium concentration. Because there is no uranium in the source initially by assumption, two regions in the ^{233}U profile are originated from uranium generated from ^{237}Np in the source and in the medium. The plateau situated in the near-field region is formed by the contribution from the source, and the plateau in the range of 300 to 1,000 m is by the generation in the medium.

Figure 6.2 shows the concentration profiles in the fracture for a chain of $^{234}U \rightarrow {}^{230}Th \rightarrow$ at 50,000 yr. Assumed parameter values are shown in the figure. Again the approximation introduces considerable error for the daughter nuclide. In this case because close values are assumed for pore retardation for the both members of the chain, the second plateau due to the generation of ^{230}Th in the medium is not observed. This is because the more dominant plateau caused by the ^{230}Th generated in the source travels nearly as fast as the uranium plateau so that the second region is covered.

6.3.2 Effect of Precursors

Radionuclides such as ^{230}Th and ^{226}Ra must be considered in the context of a decay chain because there is very small initial inventory in the waste solid or spent fuels, and most of those nuclides are generated from their mother nuclides ^{234}U. On the other hand for the evaluation of ^{234}U concentration we can use the single-member model desicribed in Chapter 2.

There is a third category of radionuclides. ^{237}Np is included in that category. ^{237}Np has a considerable initial inventory in spent fuel, so it can be considered as a mother nuclide. However, there coexists a comparable amount of ^{241}Am initially in spent fuel,

which decays to ^{237}Np with a half-life of 433 yr. Because ^{241}Am has a much shorter half-life than ^{237}Np, initial inventory of ^{241}Am may be included in that of ^{237}Np for the long-term estimate of ^{237}Np concentration, but for the time span up to tens of thousands of years we cannot neglect the effect of chain transport.

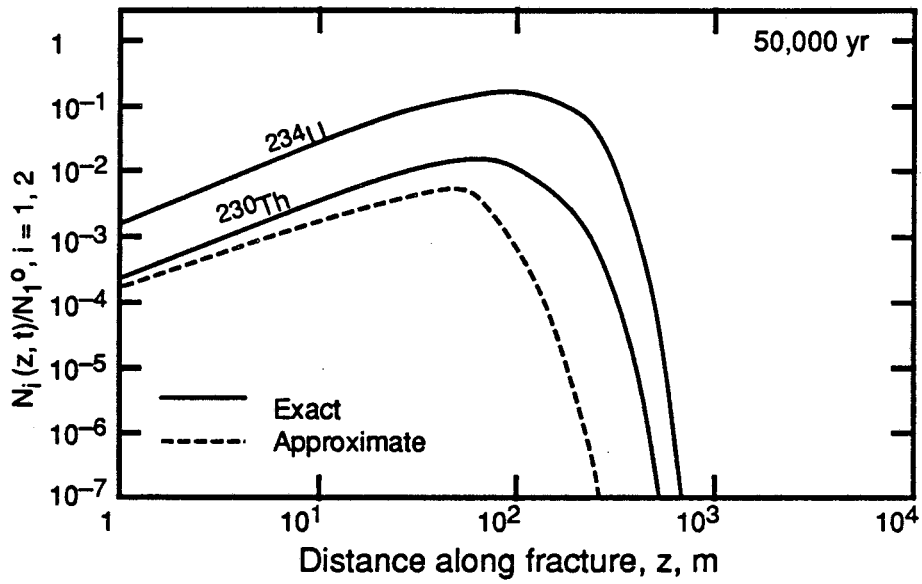

Figure 6.2 Concentration profiles of a $^{234}U \rightarrow {}^{230}Th \rightarrow$ chain. Approximate solution from Ref. [1] is compared with the exact solution. Assumed parameter values are the following: $v = 10$ m/yr, $\varepsilon = 0.01$, $2b = 1$ cm, $N^o_{234} = 1$, $N^o_{230} = 0$, $R_{f234} = R_{f230} = 1$, $R_{p234} = 15{,}000$, $R_{p230} = 50{,}000$, $D_{p234} = D_{p230} = 0.01$ m^2/yr.

In Figure 6.3, two breakthrough curves for ^{237}Np at 1,000 m far from the source are compared. Concentration is normalized by the initial concentration of ^{237}Np in the water at $z = 0$. The solid line is obtained by assuming a decay chain of $^{241}\text{Am} \rightarrow {}^{237}\text{Np} \rightarrow$ and the dashed line is by assuming that ^{237}Np is the mother nuclide. For the chain calculation the initial concentrations for both nuclides are assumed to satisfy

$$N_1^o = 1.095\, N_2^o, \qquad (6.33)$$

based on the fact that the initial inventories of ^{241}Am and ^{237}Np in 1.8 Mg of spent fuel from the pressurized water reactor are 230 g and 210 g, respectively [5].

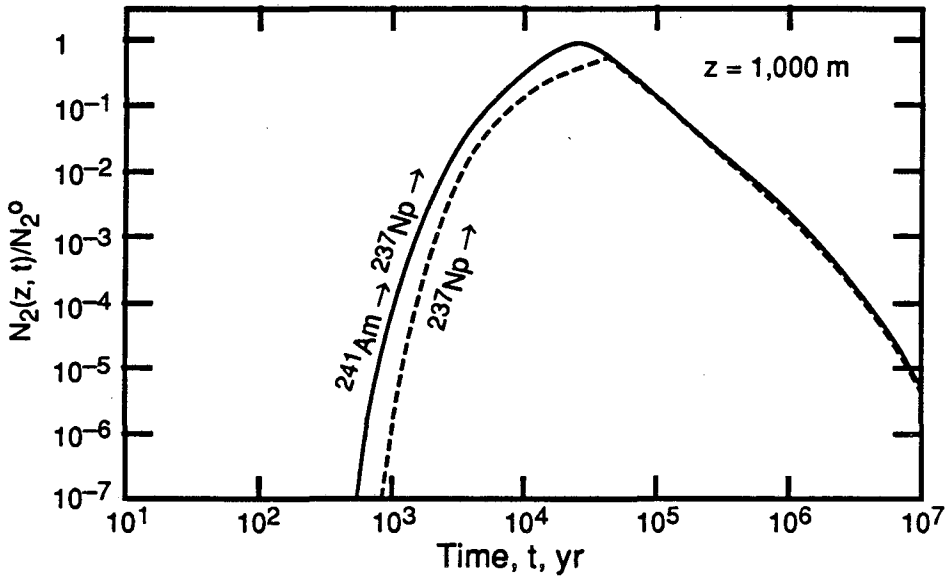

Figure 6.3 Breakthrough curves of ^{237}Np at z = 1,000 m in the fracture. The solid curve is obtained by assuming that ^{237}Np is the daughter of ^{241}Am. The dashed curve is based on the assumption that ^{237}Np has no precursors. Parameter values are summarized below.

	Chain calculations		Single calculation
	241–Am	237–Np	237–Np
half-life	433 yr	2,140,000 yr	
Initial inventory in waste	230 g /1.8 Mg of SF	210 g/1.8 Mg of SF	
Initial conc. at $z = 0$	$\hat{N}_1 = 1.095$	$\hat{N}_2 = 1$	$\hat{N}_{237} = 1$
R_f	1	1	
R_p	50	100	
D_p	0.01 m^2/yr	0.01 m^2/yr	

$T = 30{,}000$ yr, $2b = 1$ cm, $v = 10$ m/yr, $\varepsilon = 0.01$

Because smaller pore retardation is assumed for ^{241}Am than for ^{237}Np, the first arrival of Np is faster in case of a chain than in case of a single nuclide. The peak concentration is larger for the chain case than for a single-nuclide case. The reason for the higher maximum concentration for the chain case is the following. Because ^{241}Am is transported faster than ^{237}Np, there already exists neptunium in the rock matrix when the neptunium released from the source catches up, resulting in smaller concentration gradient

and diffusion flux at the rock-fracture interface. Consequently, concentration in the fracture becomes larger than in case of a single nuclide. In later times, effect of the precursor is negligible.

6.4 Conclusions

Analytical solutions for a two-member chain and an arbitrary release mode are obtained by utilizing corrected Sudicky and Frind's solutions for an impulse release. Numerical illustrations have been given for the band release.

It has been known by comparison with the exact solution that approximation by neglecting radioactive decay in the rock matrix introduces significant error even for the concentration of the second member of a chain. Although by approximation we can have non-recursive analytical solutions for a chain of arbitrary length, we should not use the approximate solutions.

Assuming that a nuclide does not have a precursor although it does results in unsafe estimate of the first arrival of the nuclide at a certain point in the fracture. A precursor, which is transported faster, decays to the daughter in rock matrix so that the diffusion flux of the daughter at the rock-fracture interface becomes smaller in the chain case than for the single-nuclide case. Therefore, the concentration in the fracture becomes larger with a precursor than without a precursor.

References

[1] Chambré, P. L., T. H. Pigford, A. Fujita, T. Kanki, A. Kobayashi, H. Lung, D. Ting, Y. Sato and S. J. Zavoshy, *Analytical Performance Models for Geological Repositories*, Chapter 5, LBL–14842, Lawrence Berkeley Laboratory, 1982,

[2] Sudicky, E. A., and E. O. Frind, Contaminant Transport in Fractured Porous Media: Analytical Solution for a Two-Member Decay Chain in a Single Fracture, *Water Resources Res., 20,* 2021, 1984,

[3] Benedict, M., T. H. Pigford, and H. M. Levi, *Nuclear Chemical Engineering,* Second ed., McGraw-Hill, New York, 1981,

[4] NAG Library Mark 10, Numerical Algorithm Group,

[5] Waste Isolation Systems Panel, Board on Radioactive Waste Management, National Research Council, *A Study of the Isolation System for Geological Disposal of Radioactive Wastes,* National Academy Press, Washington D. C., 1983.

Chapter 7
Radionuclide Dispersion from Multiple Patch Sources into a Rock Fracture

7.1 Introduction

In Chapter 2 the analytical solutions for concentrations of a radionuclide released from a source of infinite extent with zero and non-zero longitudinal dispersion in a fracture have been presented. In a real waste repository waste packages will be arranged in an array, and thus we need to investigate how local transverse dispersion affects the radionuclide plumes produced from multiple sources of finite areal extent, and under what conditions we can use the infinite-source solution.

The solutions for the concentration of a radionuclide released from multiple-patch sources with transverse dispersion, similar to the current problem, were given by *Kanki* [1]. Kanki's solutions, however, do not include sorption on the fracture wall. In the present chapter the effect of sorption on the fracture walls is included.

We shall compare the results for radionuclides released into a planar fracture from a multiple-patch source to the results for radionuclides released into continuous porous media from multiple point sources [2].

7.2 Conceptual Configuration of a Geological Repository

We consider a geologic repository with an array of point sources. The repository configuration is shown in Figure 7.1. We assume:

(1) The waste canisters are arranged in a square planar array of overall dimensions A^2.

(2) The waste consists of 10-year old waste from the pressurized water reactor, with heat generation rate of:

Spent fuel: 550 W/assembly, with one assembly per canister,

High level reprocessing waste: 1740 W/canister.

(3) The areal loading of the repository is 20 W/m^2.

(4) From assumptions 2 and 3 we will adopt for the present analysis typical container separation distance d of 10 m and 5 m. The approximate overall dimension A of the repository is 900 m.

This repository is assumed to intersect a planar fracture of infinite extent and of width $2b$. To establish a nuclide-transport problem, we make the following further assumptions:

(5) The fracture intersects with the repository so that the width of the cross-section of the repository becomes A.

(6) Each waste container is exposed only to the fracture water and can be approximated as a planar patch source; the rest of the waste canister imbedded in the rock matrix is sound, so no nuclide is released directly to the rock matrix. The dimensions of an individual plane patch source are $2a \times 2b$, where $2a$ is the width of a patch source which is assumed to be equal to the diameter of the waste canister and $2b$ is the fracture width.

By assumptions 5 and 6 multiple-patch sources are located within the width A with a separation or pitch d. The number of patch sources is, therefore, calculated as $m = A/d$.

In Figure 7.2 physical processes considered in the model are shown. Difference between the model in Chapter 2 and here is that hydrodynamic dispersion transverse to the direction of water flow in the fracture is assumed instead of longitudinal dispersion. Geometry of the source is also different from that in Chapter 2. Here m patches are located at $z = 0$, while in Chpater 2 the source has an infinite extent along the x axis.

7.3 The Transport Equations, Initial and Boundary Conditions

The transport processes in the system described above can be written in terms of two coupled differential equations very similar to those given in Chapter 2. The governing equation for the concentration in the water in the fracture is written as:

$$R_f \frac{\partial N}{\partial t} + v \frac{\partial N}{\partial z} - D_T \frac{\partial^2 N}{\partial x^2} + R_f \lambda N + \frac{q}{b} = 0, \quad t > 0,\ z > 0,\ -\infty < x < \infty, \tag{7.1}$$

where D_T is the transverse dispersion coefficient. The governing equation for the porous rock matrix is identical to (2.9):

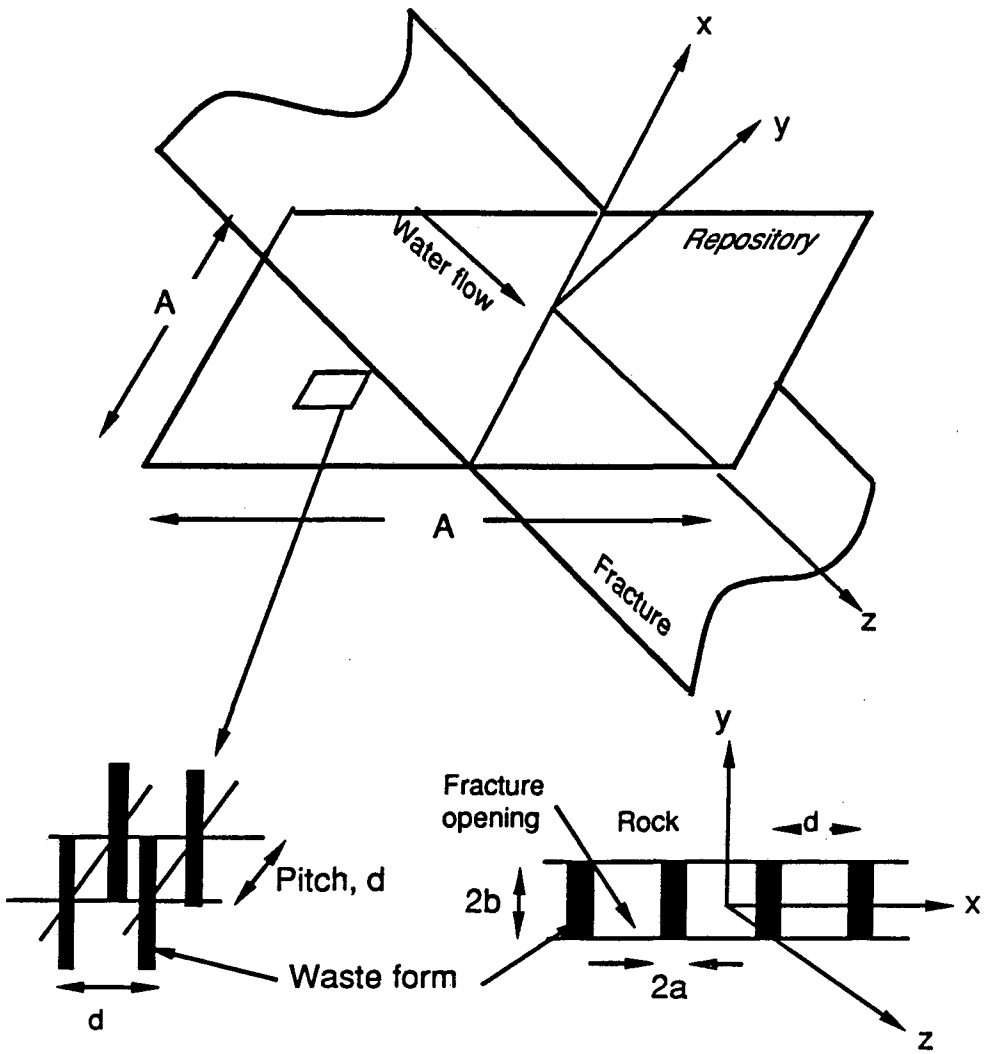

Figure 7.1 Conceptual configuration of a geologic repository and a plane fracture of infinite extent. In the right-bottom figure waste forms are assumed to be plane patch sources of dimensions $2a \times 2b$.

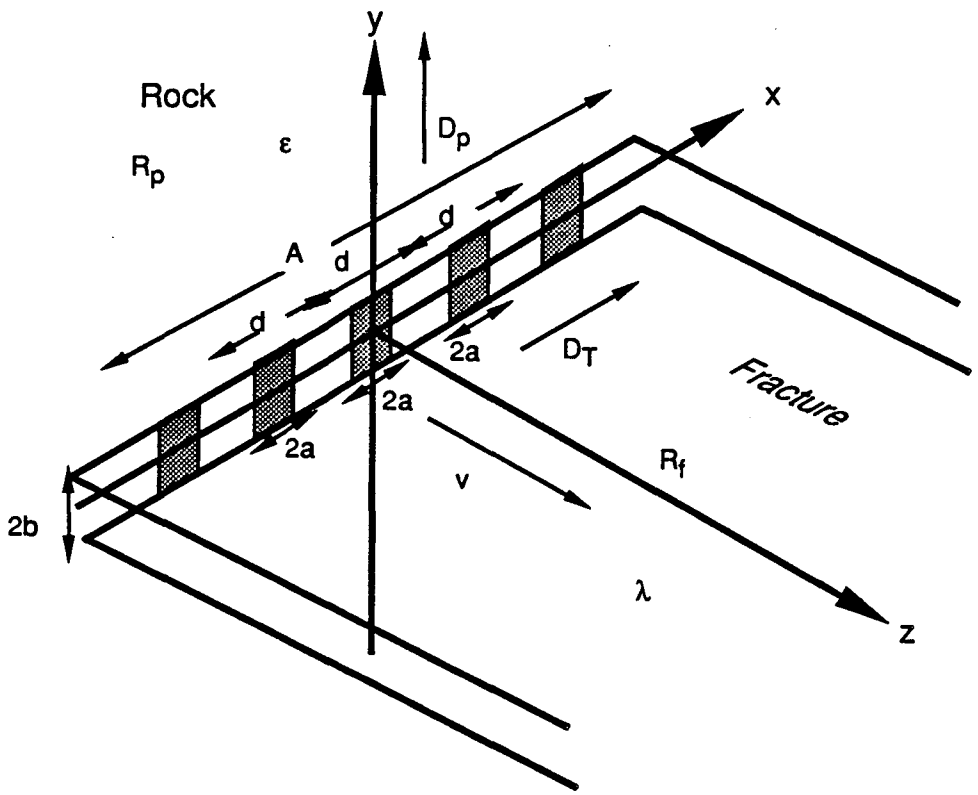

Figure 7.2 Geometry and physical processes to be considered in mathematical formulation.

$$R_p \frac{\partial M}{\partial t} - D_p \frac{\partial^2 M}{dy^2} + R_p \lambda M = 0,\ y > b, z > 0, -\infty < x < \infty, t > 0. \qquad (7.2)$$

Diffusion flux at the rock-fracture interface is given by (2.11). See Chapter 2 for nomenclatures.

We solve these governing equations subject to the following initial and boundary conditions:

Initial Conditions:

$$N(x, z, 0) = 0, -\infty < x < \infty, \quad z > 0, \qquad (7.3)$$

$$M(x, y, z, 0) = 0, \quad -\infty < x < \infty, \quad y > b, \quad z > 0, \qquad (7.4)$$

Boundary Conditions:

$$N(x, 0, t) = \psi(t)\{h(x+a) - h(x-a)\}, \quad -\infty < x < \infty, \quad t > 0, \qquad (7.5)$$

$$N(x, \infty, t) = 0, \quad -\infty < x < \infty, \quad t > 0, \qquad (7.6)$$

$$N(\pm\infty, z, t) = 0, \quad z > 0, \quad t > 0, \tag{7.7}$$

$$M(x, b, z, t) = N(x, z, t), \quad -\infty < x < \infty, \quad z > 0, \quad t > 0, \tag{7.8}$$

$$M(x, +\infty, z, t) = 0, \quad -\infty < x < \infty, \quad z > 0, \quad t > 0, \tag{7.9}$$

where $\psi(t)$ represents a time-dependent strength of a single-patch source and $h(\cdot)$ the Heaviside step function. (7.5) assumes that the center of a single patch source of dimensions $2a \times 2b$ is located at the origin of the system. For multiple-patch sources we can superpose the solution for a single-patch source. Also assumed is that within each patch source the time-dependency is uniform. To illustrate, we consider the band release mode for $\psi(t)$ (see Figure 2.3 and equation (2.49) for definition.).

7.4 Transport of Radionuclide Released from a Single Patch Source

7.4.1 The Analytical Solution for a Single Patch Source

We obtain the solution to the governing equations by taking Laplace transforms of (7.1) and (7.2) with respect to t and Fourier transform of the Laplace-transformed (7.1) with respect to x, with the aid of the initial and boundary conditions. The analytical solutions for $N(x, z, t)$ and $M(x, y, z, t)$, subject to side conditions (7.3) through (7.9), are:

$$N(x, z, t; m=1) = N^{o}F^{\infty}(b, z, t)X(x; \theta, a, 0), \quad -\infty < x < \infty, z \geq 0, t \geq 0, \tag{7.10}$$

$$M(x, y, z, t;, m=1) = N^{o}F^{\infty}(y, z, t)X(x; \theta, a, 0), \quad -\infty < x < \infty, y \geq b, z \geq 0, t \geq 0, \tag{7.11}$$

where

$$F^{\infty}(y, z, t) = F_4(y, z, t) - e^{-\lambda T}F_4(y, z, t - T), \tag{7.12}$$

$$X(x; \theta, z, x_1) = \frac{1}{2}\left[erf\left(\frac{x - x_1 + a}{2\theta}\right) - erf\left(\frac{x - x_1 - a}{2\theta}\right)\right], \tag{7.13}$$

$$\theta = \sqrt{\frac{zD_T}{v}}, \tag{7.14}$$

m the number of patch sources, and x_1 the coordinate of the transverse axis of the center of the patch source. The function $F_4(y, z, t)$ is defined in (2.64). The parameter θ is called a distance parameter, whose dimension is [m]. The distance parameter is a key parameter in evaluating the effect of the transverse dispersion, as will be shown in the next section. Because the center of the patch source is located at the origin of the system, we set $x_1 = 0$ in (7.10) and (7.11). Since the solutions to $N(x, z, t; m)$ and $M(x, y, z, t; m)$ have the same structure, any observation made for $M(x, y, z, t; m)$ can be applied to $N(x, z, t; m)$, and thus we will make use of the solution to $M(x, y, z, t; m)$ for further analysis.

In the analytical solutions we find that the effect of transverse dispersion appears in the function $X(x; \theta, a, x_1)$. The rest of the solution, i.e., $N^o F^\infty(y, z, t)$ in (7.11), is identical to the solution for an infinite-plane source, (2.61):

$$M^\infty(y, z, t) = N^o F^\infty(y, z, t). \qquad (7.15)$$

As a approaches infinity, $X(x; \theta, a, x_1)$ becomes unity. If we take D_T to zero, or θ to zero, $X(x; \theta, a, x_1)$ also becomes unity. In the latter case the function $M^\infty(x, y, z, t)$ can be considered as a solution to zero transverse dispersion.

In numerical evaluation of the analytical solutions (7.10) and (7.11), if we make a computer program in such a way that (7.13) is calculated by subtracting two error functions, which is apparently done in Kanki's program, for a large x value and a comparably small a value, the two error functions in (7.13) yield very close values, and on the subtraction a numerical error occurs because a digital computer can handle only a limited number of significant digits. To avoid this, we return to the original definition of an error function expressed with an integral, and combine the two error functions in (7.13) into one integral, which is now evaluated numerically with the Gaussian quadrature method. For numerical integration we use the NAG [3] subroutine D01AJF, which is a general-purpose integrator.

7.4.2 Numerical Illustrations and Observations

With analytical solutions (7.10) and (7.11), we now observe the time-dependency of concentrations and the effect of transverse dispersion on concentration profiles. To illustrate, we consider ^{237}Np released from a single-patch source with the band release. We conservatively assume that there is no sorption on the fracture walls (R_f=1), but that in a porous rock matrix sorption is moderate (R_p = 100). Other parameters are set equal to the previous chapters, and listed in each figure shown later in this chapter.

The concentration profiles of ^{237}Np released from a single-patch source along the transverse direction x at various values of the downstream distance z are shown in Figure 7.3. These concentrations are normalized to the initial concentration at the source. The transverse hydrodynamic dispersion coefficient D_T is assumed to be 0.05 m^2/yr. Considering the value for molecular diffusion coefficient in the rock matrix (D_p = 0.01 m^2/yr)

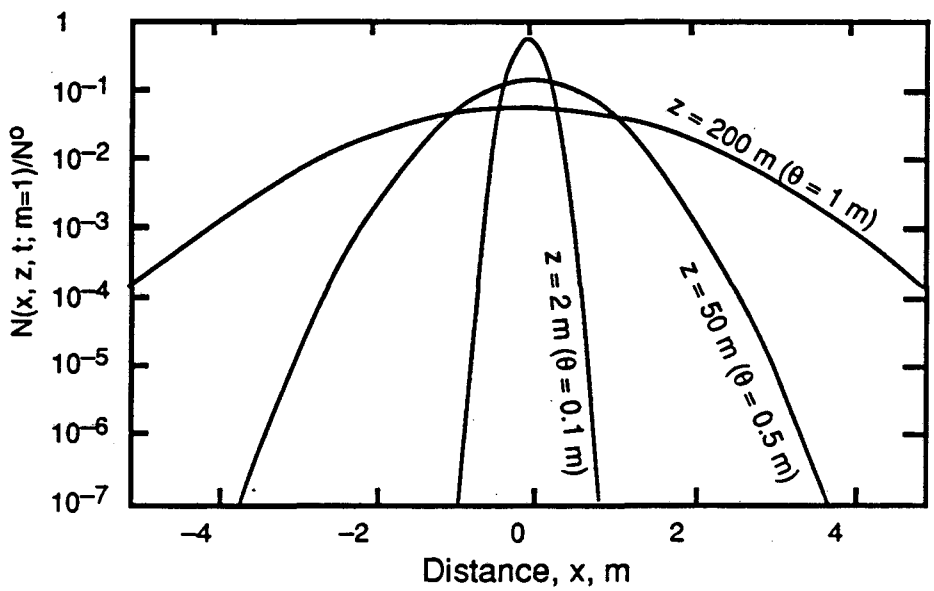

Figure 7.3 Concentration profiles of ^{237}Np in the fracture in transverse direction, at t = 10,000 yr, a band release. Parameter assumed here are: T = 30,000 yr, a = 0.14 m, x_1 = 0, v = 10 m/yr, $\lambda = 3.24 \times 10^{-7}$/yr, $2b$ = 0.01 m, ε = 0.01, D_p = 0.01 m^2/yr, D_T = 0.05m^2/yr, R_p = 100, R_f = 1.

and the tortuosity in the rock matrix, we may say that the value chosen for D_T here neglects mechanical dispersion which is usually included in hydrodynamic dispersion together with molecular diffusion. By neglecting mechanical dispersion, we underestimate the effect of transverse hydrodynamic dispersion on fracture-flow transport, but by Figure 7.3 we see remarkable influence of the transverse dispersion even with the small value of $D_T = 0.05$ m^2/yr.

For a small downstream distance z the concentration profiles in Figure 7.3 show a smaller dispersion path length and a steeper concentration gradient along the transverse axis x, and a larger peak value at $x = 0$. As pointed out in [1], this dispersion behaviour is quite different from the diffusion behaviour into the rock matrix in the y-direction. In the case of molecular diffusion into the rock matrix, a smaller diffusion path length in the y-direction is observed at a larger downstream distance z. This difference is explained by introducing the concept of an effective diffusion or dispersion time t_e (see Figure 7.4). Since the dispersion field in the x-direction moves with the water at the velocity v/R_f, the effective time for the transverse dispersion at a location z can be determined by:

$$t_e = \frac{z R_f}{v}, \tag{7.16}$$

while the effective time for diffusion in the y-direction is given by:

$$t_e = t - \frac{z R_f}{v}, \tag{7.17}$$

since the diffusion field in the rock pore is at rest.

The peak value shown in each profile of Figure 7.3 is attenuated by both the transverse dispersion in the x-direction and the molecular diffusion in the y-direction. To contrast these effects, plotted in Figure 7.5 are the concentrations of ^{237}Np along the $x = 0$ line in the fracture at $t = 10{,}000$ yr (before the end of the leaching period) for the following three cases: the concentrations with both the dispersion in the x-direction and the molecular diffusion in the y-direction (solid lines), the concentrations with the molecular

diffusion but without the transverse dispersion (a dashed line), and the concentrations without them (a dotted line).

Without transverse dispersion or matrix penetration the leading edge travels as a square wave at the velocity v/R_f. If matrix penetration in the y-direction is considered,

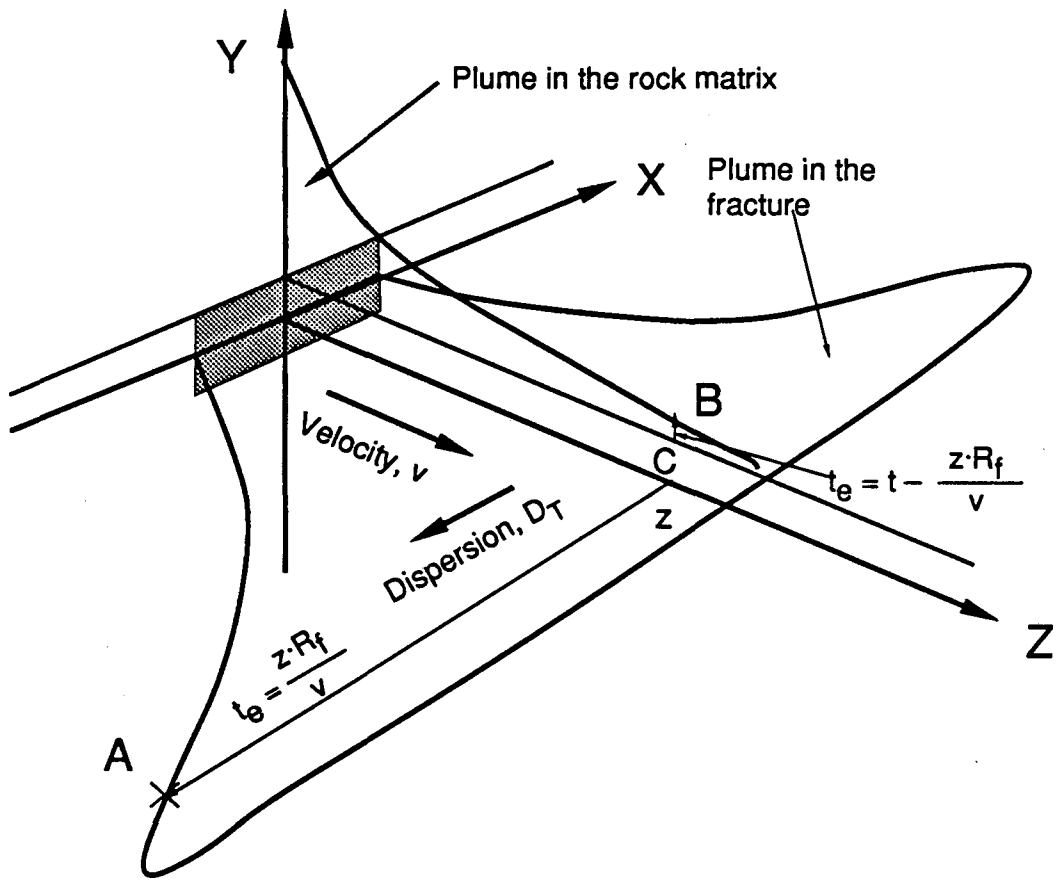

Figure 7.4 Difference in transverse dispersion along the x-axis and molecular diffusion in the rock matrix along the y-axis. Radionuclides take time $t_e = z \cdot R_f / v$ to reach point A in the fracture by advection and transverse dispersion. Since advection and transverse dispersion take place together, the plume in the fracture shows a diverging shape. On the other hand, in order for radionuclides to reach point B in the rock matrix, they must first reach point C in the fracture, and then by molecular diffusion radionuclides reach point B for time $t_e = t - z \cdot R_f / v$. Thus, at more distant points from the source, the region affected by molecular diffusion becomes small.

some of the radionuclide is removed from the fracture by matrix penetration, resulting in the retardation of nuclide movement along the fracture. If we consider both matrix penetration and transverse dispersion in the fracture, the concentrations are further attenuated along z. This combined effect is more pronounced for larger values of D_T. For instance, the concentration at z = 1,000 m for D_T = 0.05 m^2/yr is only about 1 percent of that without transverse dispersion. However, transverse dispersion has no significant effect in retarding the movement of the leading contamination edge in the fracture even for a large value of the dispersion coefficient. This is explained by the fact that around the leading edge the gradient due to transverse dispersion becomes quite low.

These observations can also be made for the profiles after the end of leaching period. Figure 7.6 shows the concentration profiles of ^{237}Np at x = 0 in the fracture for D_T = 0.05 m^2/yr and D_T = 0. As was observed at a time before the leach time in Figure 7.5, the loci of the leading edge and the maximum are not retarded by transverse dispersion although the concentrations are attenuated by several orders of magnitude due to the transverse dispersion.

Without molecular diffusion into the rock pores, the band-shaped concentration profile moves along the z-direction after the leach time (the dotted curve). On the other hand, with molecular diffusion and without transverse dispersion in the fracture, a trailing tail in the near-field from the source in the dashed curve in Figure 7.6 results from uncontaminated water flowing into the fracture after the leach time as observed in Chapter 4. The observations on back diffusion made in Figure 4.8 all hold here, because from (7.11) influence of transverse dispersion is completely separated from back diffusion.

In Figure 7.7 we can confirm that the nuclide diffuses out to the fracture at z = 10 m. The profiles for zero transverse dispersion and for non-zero transverse dispersion seem parallel to each other, which means that the ratio of the two concentration is independent of y, and even of time. If we take the ratio of the analytical solution for the

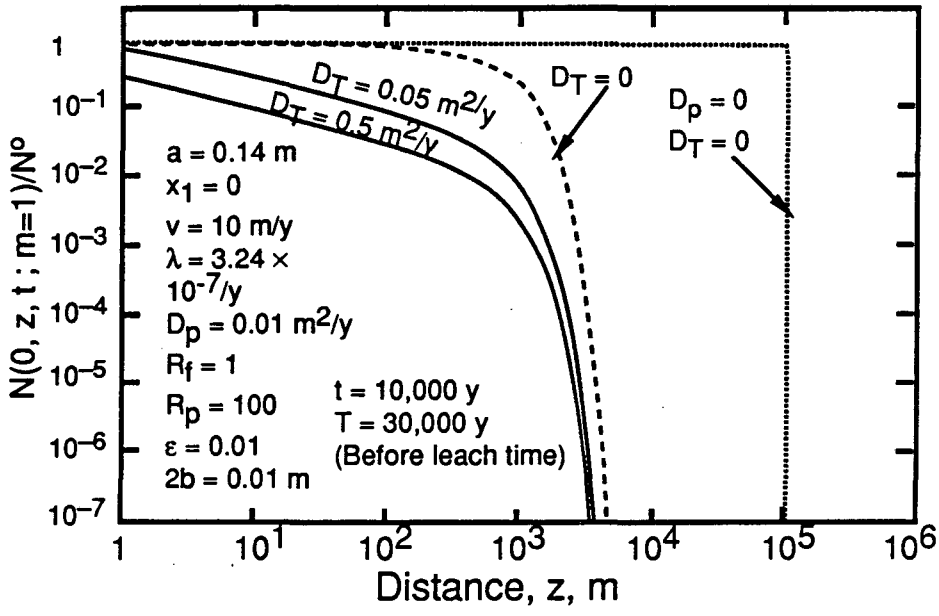

Figure 7.5 Effect of transverse dispersion on fracture flow transport, concentration profile of ^{237}Np at x = 0 in the fracture at t = 10,000 yr (before the leach time T = 30,000yr) with three different transverse dispersion coefficients.

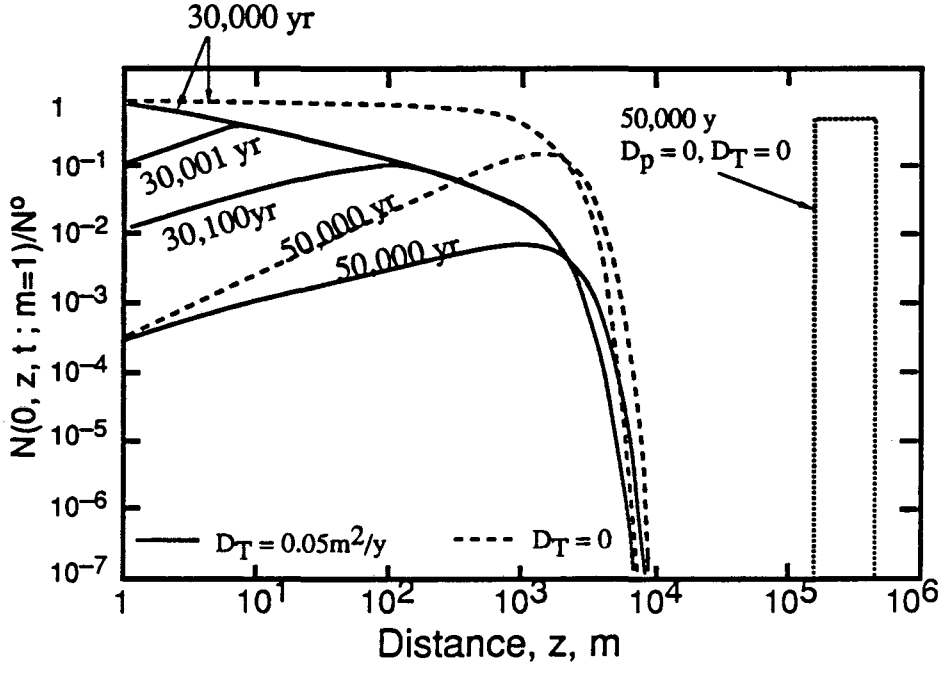

Figure 7.6 Concentration profiles of ^{237}Np at x = 0 in the fracture at times after the leach time T = 30,000 yr. Assumed parameter values are the same as in Figure 7.5.

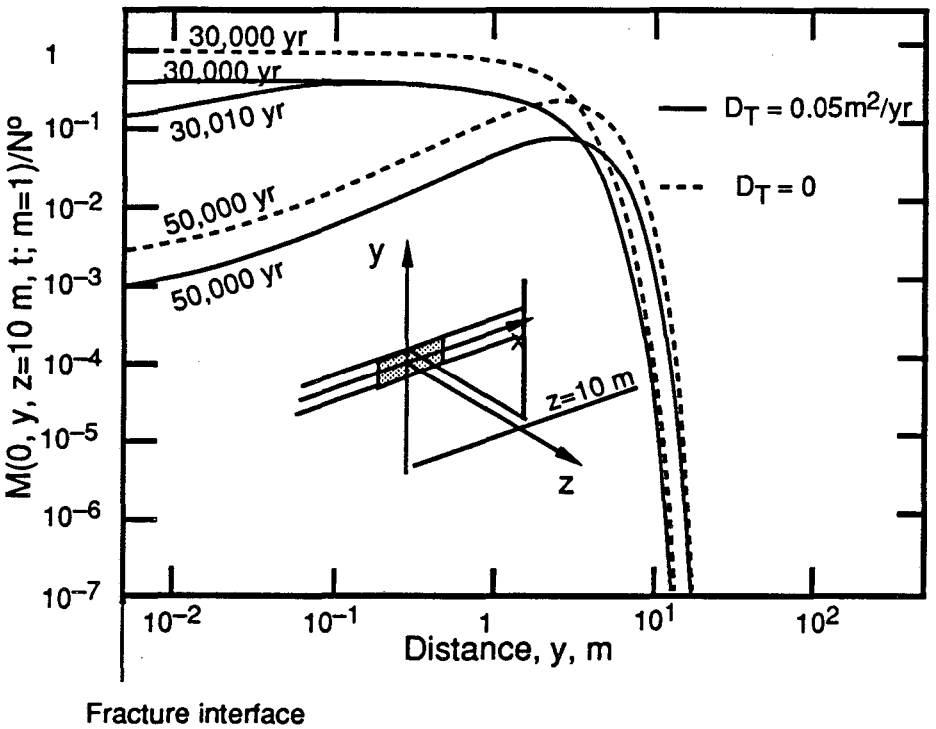

Figure 7.7 Time-dependent concentration profiles at (x, z) = (0, 10m) in the rock matrix. The same parameter values as Figure 7.5 apply.

case of non-zero transverse dispersion with that for the case of zero-dispersion, the ratio becomes independent of time, nuclide, the distance into the rock matrix, and other rock-related parameters. We will observe the behaviour of multiple-patch sources by using this ratio with an appropriate definition of equivalent source strength in the following sections.

7.5 Transport of Radionuclides Released from Multiple-Patch Sources

For multiple-patch sources, we would expect to see the effects of individual sources near the sources. At some distance away, local dispersion would merge individual plumes so that an equivalent infinite plane source might give equally satisfactory results. At still larger distances the effect of transverse dispersion causes multiple-patch sources to behave like a single, large patch source. To quantify these regions, we first derive the analytical solutions for multiple-patch sources by superposition of the single-patch-source solutions shown in the previous section. We take the ratio of the concentration resulting from

multiple-patch sources to the concentration resulting from an infinite source and the ratio of the concentration resulting from multiple-patch sources to the concentration resulting from a single patch of equivalent source strength. These ratios would predict the three regions.

7.5.1 Formulation for Analysis

The analytical solutions for multiple-patch sources are obtained by superposing the solutions for a single-patch source. The geometry studied was described in Section 7.2. Each patch source has an identical width $2a$ with the same initial concentration N° at $z = 0$, the same release characteristics, e.g., the band release, and is separated by a pitch d. All sources begin to release radionuclides at the same time. Then the solutions for m patch sources are:

$$M(x, t, z, t; m) = N^o F^\infty(y, z, t) \sum_{k=1}^{m} X(x; \theta, a, x_k), \qquad (7.18)$$

where x_k is the location of the center of the k-th patch on the transverse axis x, and can be expressed as:

$$x_k = d\left(k - \frac{m+1}{2}\right), \quad k = 1, 2, \ldots, m \qquad (7.19)$$

To compare the solution (7.18) with the solution for an infinite source, we must define the source strength of each patch source properly. For a patch source of initial total mass w^o [kg], distributed uniformly over the patch cross-sectional area $2a \times 2b$, and a leach time T [yr], the rate of dissolution of total mass from the patch is w^o/T [kg/yr]. From (2.50) the initial concentration in the water phase at $z = 0$ for the patch source is:

$$N^o = \frac{w^o}{vT\,(2a)\,(2b)} n^o, \qquad \left[\frac{kg}{m^2 \cdot yr}\right], \qquad (7.20)$$

where n^o is the initial mass fraction of the nuclide in the waste (dimensionless). On the other hand, if we assume that the same amount of waste w^o [kg] is distributed over a patch of cross-sectional area $d \times 2b$, then we obtain the initial concentration N^o_{eq} for the patch

source of dimensions $d \times 2b$ as:

$$N_{eq}^{o} = \frac{w^{o}}{vT\,(2b)\,d} n^{o}, \quad \left[\frac{kg}{m^{2} \cdot yr}\right]. \tag{7.21}$$

From (7.20) and (7.21), we can obtain a simple relation between N^o and N_{eq}^o in terms of the dimensions of the both sources:

$$\frac{N^{o}}{N_{eq}^{o}} = \frac{d}{2a}. \tag{7.22}$$

We can now write the solution for an infinite source of strength equivalent to the multiple-patch sources located in a pitch d by connecting infinitely many patch sources of width d which produce initially the concentration N_{eq}^o at $z = 0$:

$$M^{\infty}(y, z, t) = N_{eq}^{o} F^{\infty}(y, z, t). \tag{7.23}$$

Similarly the solution for an equivalent single patch source which should be compared with the multiple-patch sources consisting of m patches located in a pitch d can be written as:

$$M^{eq}(x, y, z, t) = N_{eq}^{o} F^{\infty}(y, z, t)\, X(x; \theta, \frac{md}{2}, 0). \tag{7.24}$$

In the following we will observe the effect of transverse dispersion with the help of the ratio of (7.18) to (7.23) and the ratio of (7.18) to (7.24):

$$\frac{M(x, y, z, t; m)}{M^{\infty}(y, z, t)} = \frac{d}{2a} \sum_{k=1}^{m} X(x; \theta, a, x_k), \tag{7.25}$$

$$\frac{M(x, y, z, t; m)}{M^{eq}(x, y, z, t)} = \frac{d}{2a} \frac{\sum_{k=1}^{m} X(x; \theta, a, x_k)}{X(x; \theta, \frac{md}{2}, 0)}. \tag{7.26}$$

7.5.2 Comparison for Multiple-Patch Sources with an Infinite Source

Figure 7.8 shows the relative nuclide concentration along the transverse coordinate, x, normal to the direction of the water flow, for the values of θ = 0.2, 0.4, 1 and 10 m.

The radionuclide source consists of 10 waste packages intersected by a fracture. The width of the overall source with 10 waste packages separated on 10 m centers is 100 m. The centers of the patch sources are located at $\pm x = d/2, 3d/2, ...,$ etc. For constant values of D_T and v, θ is a downstream distance parameter. Figure 7.8 shows that for small values of θ, the concentration profile along the transverse coordinate predicted by the muliple-patch-source model is quite different from that predicted by the infinite-source model. Near the sources, the local plumes are evident. At θ = 10 m, local transverse dispersion has smeared the plumes together so that the two models give identical results.

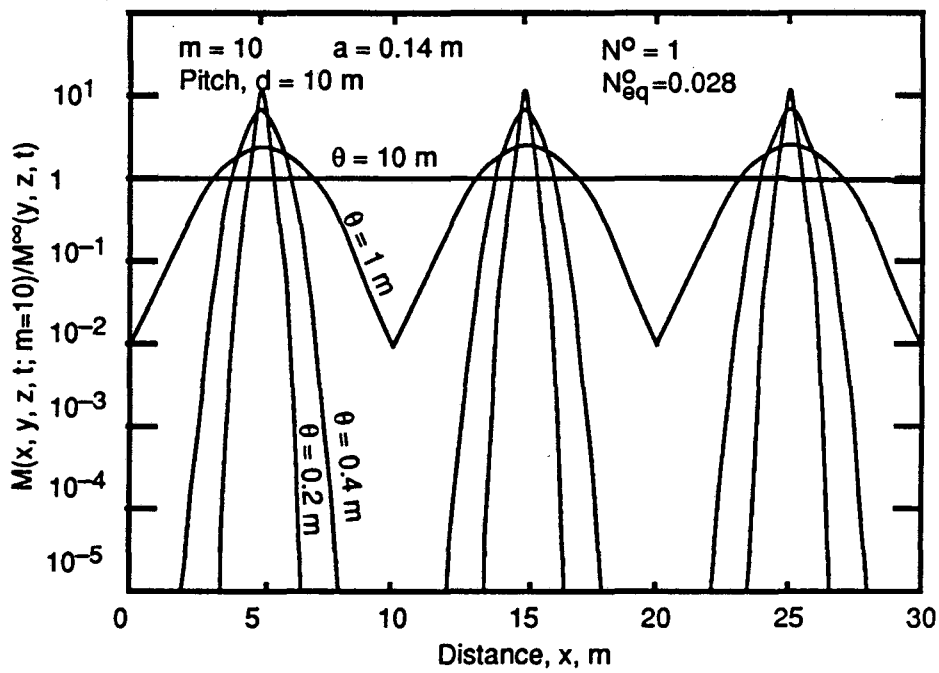

Figure 7.8 Distribution of the relative concentration (multiple-patch sources/ an infinite source) for four values of the distance parameter along the transverse coordinate x.

The deviation from the infinite-source solution can be observed more clearly in Figure 7.9, which shows the relative nuclide concentration as a function of the distance parameter θ for a series of patch sources, with a source spacing of d = 10 m and for the number of patch sources varying 10 to 80. The "peaks" are clearly seen in Figure 7.8, and

the "valleys" can be seen for the θ = 1 m curve in Figure 7.8. The near-field concentration ratios, for less than θ = 3 m, are shown for two branches. The peaks occur opposite the patch locations ($x = d/2$) and the valleys occur at the midpoint between adjacent sources ($x = 0$). These two branches coincide at greater than about θ = 3 m, where the multiple-patch concentration becomes identical to that from the infinite-source model. The concentration ratio remains at unity until a larger value of the distance parameter is reached, depending upon the number of patches. The multiple-patch concentration then becomes less than the infinite-source concentration, because of overall transverse dispersion.

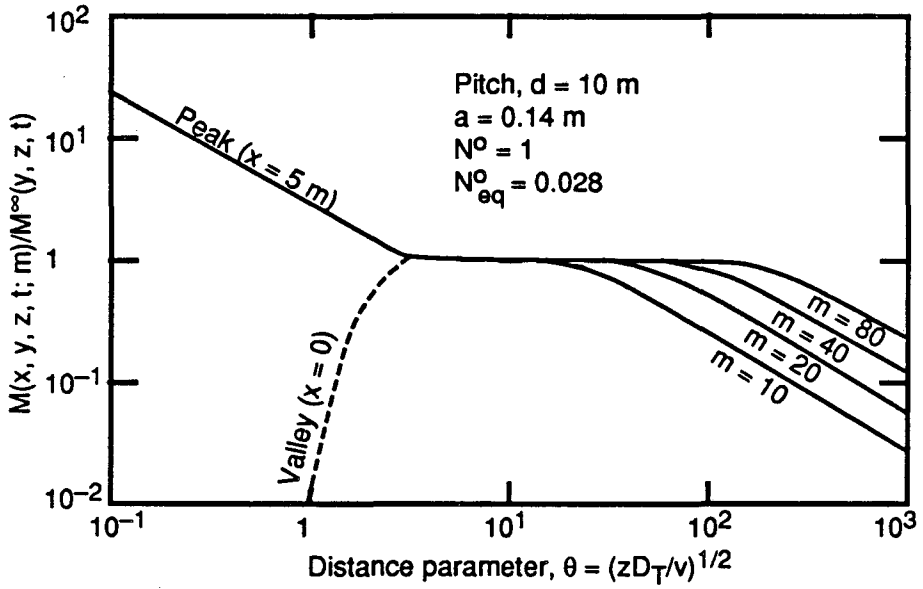

Figure 7.9 Effect of the size of multiple-patch sources on relative concentration profiles as a function of the distance parameter. For physical meanings of the peak and valley, refer to Figure 7.8.

From Figure 7.9, we can observe three regions according to the distance parameter θ: (1) For θ less than about 3 m, the multiple-patch concentration departs significantly from the infinite-source concentration due to discontinuities between discrete patch sources. (2) For θ between 3 m to 10 or 100 m, depending upon the number of patches, these two concentrations become identical because of local transverse dispersion. (3) For larger θ

values, the multiple-patch concentration becomes less than the infinite-source concentration because of transverse dispersion into the region outside the projected *m*-patch area. These observations are independent of radionuclide, time and rock.

In Figure 7.10 we observe the effect of patch-source separation. By decreasing the source separation the plumes merge at a shorter downstream distance, as might be expected. The effect of overall transverse dispersion also occurs a shorter distance downstream.

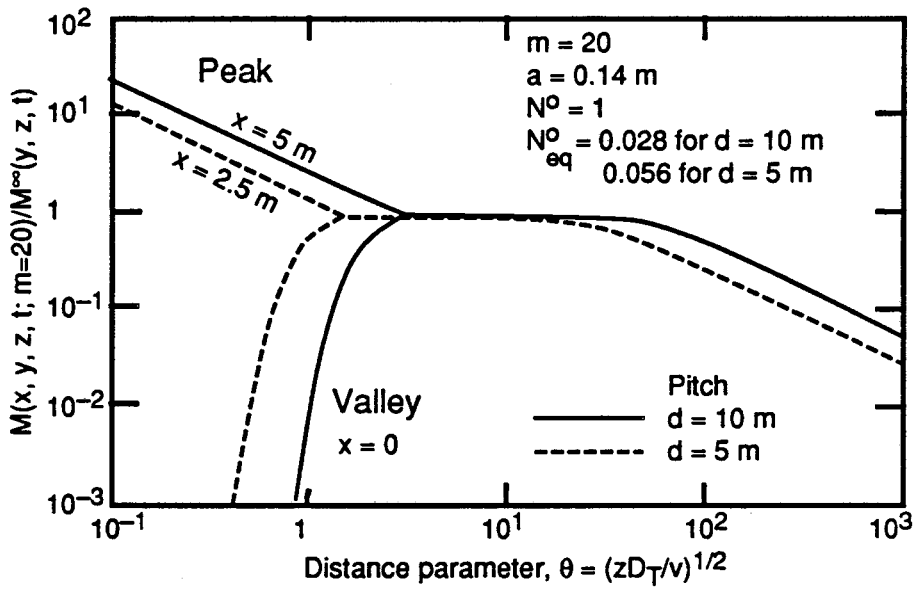

Figure 7.10 Effect of source separation on relative concentration profiles as a function of the distance parameter.

7.5.3 Comparison for Multiple-Patch Sources with a Single Equivalent Source

In this section we compare the nuclide concentration fields predicted by a multiple-patch source and a single equivalent-strength source. Figure 7.11 shows the relative nuclide concentration as a function of the distance parameter θ for 10 to 80 patch sources, spaced 5 m or 10 m apart. In Figure 7.11 the plumes-merge points are identical to those in Figure 7.10. However, there is no third region where transverse dispersion reduces the

concentrations at the edge of the merged plume. This is because an equivalent patch source is created depending on the number of patch sources. The single equivalent patch source predicts identical concentrations as the multiple-patch source for θ greater than about 3 m.

Figure 7.11 implies that for estimation of far-field concentrations we can consider the repository which actually consists of *m* patch-sources as a large single-patch source of width *A* (see Figure 7.1 for definition). The strength of that large single-patch source can be calculated by (7.22), as shown in Section 7.5.1. Thus we can investigate the effect of the size of the repository with the aid of an equivalent-single-patch-source solution.

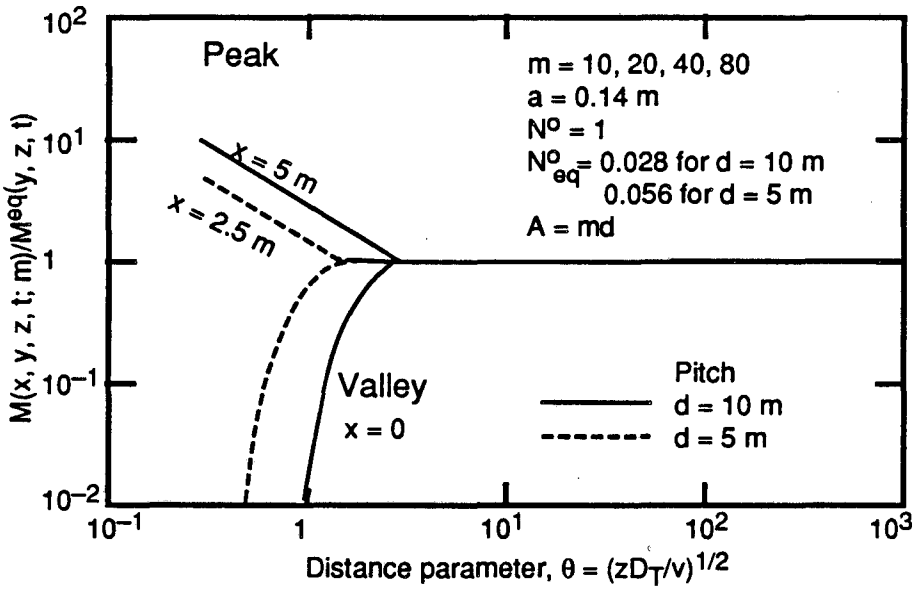

Figure 7.11 Relative concentration (multiple-patch sources/ an equivalent patch source) as a function of the distance parameter.

Figure 7.12 shows the relative concentration at $x = 0$ as a function of the variable θ for three widths of the repository. Note that, as long as we follow the procedure for definig the equivalent source strength as shown in Section 7.5.1, this graph is valid for any set of source separation distance and dimension of waste packages. In the case of a relatively small repository of $A = 200$ m, the relative concentration at $x = 0$ begins to decrease at $\theta > 30$ m. For example, if $v = 10$ m/y and $D_T = 0.05$ m^2/y, the effect of the

transverse dispersion becomes important at $z > 1.8 \times 10^5$ m. For the larger repository of $A = 800$ m, the concentration profile in a normal plane through the center of the patch ($x = 0$) is identical with the concentration profile resulting from an infinite source up to $\theta = 100$ m.

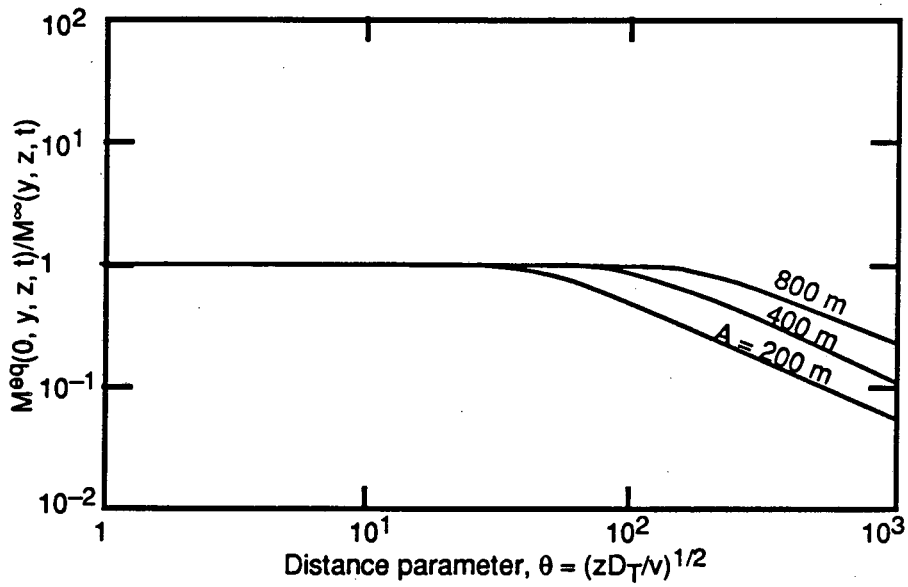

Figure 7.12 Effect of a repository size on the far-field concentration evaluated by the equivalent-single-solution.

7.5.4 Comparison for Transport in Fractured Media with Transport in Porous Media with Arrayed Point Sources

In Reference [4] presented is an analytical study of the effect of transverse dispersion on migration behaviour in one-dimensional flow in a porous rock. The analyses were performed for the geometry shown in Figure 7.13. A two-dimensional repository of dimensions A^2 consists of an array of point sources in a pitch d. The porosity of the rock is ε. Water flows at pore velocity v in the direction perpendicular to the repository plane. Linear sorption equilibrium is assumed in the porous rock, so nuclide movement is retarded. Dispersion transverse to the water flow is then two-dimensional, and transverse dispersion coefficient for each direction is assumed to be equal.

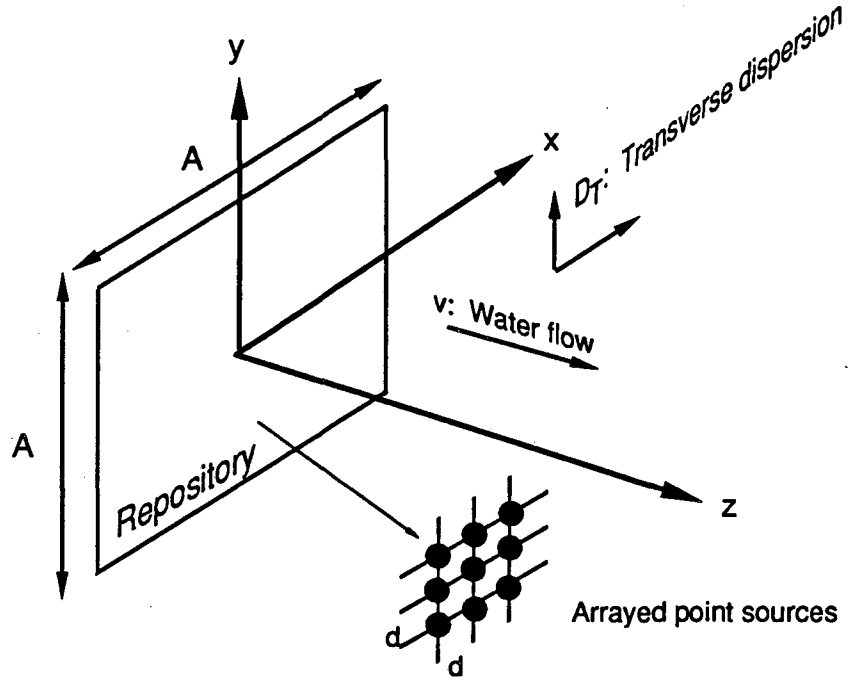

Figure 7.13 Geometry for the problem of the porous-media transport.

The analytical solution for a point source with transverse dispersion was first obtained. This solution was used for obtaining the solution for an array of point sources with transverse dispersion by superposition. The plane source of dimensions d^2 which has an equivalent strength to a point source was obtained in a similar way to that described in Section 7.5.1. By connecting infinitely many plane sources of equivalent strength, an infinite plane source of equivalent strength was defined. Then the ratio of the concentration resulting from an array of point sources to the concentration resulting from an infinite-plane source of an equivalent strength was taken to clarify the effect of transverse dispersion. The ratio has the form of:

$$\frac{N^a(x, y, z, t)}{N^\infty(z, t)} = \frac{\varepsilon d^2}{4\pi\theta^2} \sum_{k=1}^{m} \sum_{j=1}^{n} exp\left[-\frac{(x - x_k)^2 + (y - y_j)^2}{4\theta^2} \right], \qquad (7.27)$$

where $N^a(x, y, z, t)$ is the concentration resulting from an array of point sources, $N^\infty(z, t)$ the concentration resulting from an infinite-plane source, θ the distance parameter. (x_k, y_j) are the coordinates of point source location. There are m point sources on the x-coordinate

and n point sources on the y-coordinate. The factor consisting of ε, d, and θ ahead of the double summation comes from the ratio of the initial concentration at $z = 0$ resulting from a point source to the initial concentration at $z = 0$ resulting from an infinite-plane source.

Equation (7.27) can be compared with (7.25), which is for transport in a fractured medium. Both formula have a very similar structure; (7.27) contains an exponential function under the summation while (7.25) contains two error functions. This is because the ratio (7.27) is taken for point sources while the ratio (7.25) for patch sources, which can be rewritten in integral form:

$$\frac{M(x, y, z, t; m)}{M^{\infty}(y, z, t)} = \frac{d}{2a\sqrt{\pi}} \sum_{k=1}^{m} \int_{\xi-\alpha}^{\xi+\alpha} e^{-t^2} dt, \quad \text{where } \xi = \frac{x - x_k}{2\theta} \quad \text{and } \alpha = \frac{a}{2\theta}. \quad (7.28)$$

Figure 7.14, taken from Reference [4], shows results for the porous-media analyses. Comparing Figure 7.14 with Figure 7.9, we can make several observations. First, there are three regions for the distance parameter θ. Second, the θ values dividing the three regions are almost equal. In fact in Figure 7.9, the peak and valley branches coincide at $\theta = 3$ m, the same as in Figure 7.14. The m = 10, 20, 40, and 80 cases in Figure 7.9 correspond to the arrays 10×10, 20×20, 40×40 and 80×80 in Figure 7.14, respectively. For each pair the ratio starts to deviate from unity at approximately the same θ values. For example, in Figure 7.9, for $m = 10$ the curve starts to deviate from unity at θ slightly larger than 10. In Figure 7.14, the 10×10 array case shows that the curve also becomes smaller than unity at θ approximately equal to 10 m.

This observation implies that multiple-patch sources which we have investigated in the preceding sections have a behaviour very similar to multiple-*point* sources. In the analytical solution (7.28) this can be explained as follows. Since the width $2a$ of a patch source is very small compared with the pitch d (we took $a = 0.14$ m and $d = 10$ m), for a relatively large θ the integration interval in (7.28) becomes very small so that we can approximate the integral as follows:

$$\int_{\xi-\alpha}^{\xi+\alpha} e^{-t^2}\,dt \approx \frac{a}{\theta}\, e^{-\xi^2}, \quad \text{where } \xi = \frac{x - x_k}{2\theta} \text{ and } \alpha = \frac{a}{2\theta}. \tag{7.29}$$

Substituting (7.29) into (7.28) and comparing with (7.27), we can immediately see the similarity between (7.27) and (7.28) for a relatively large θ.

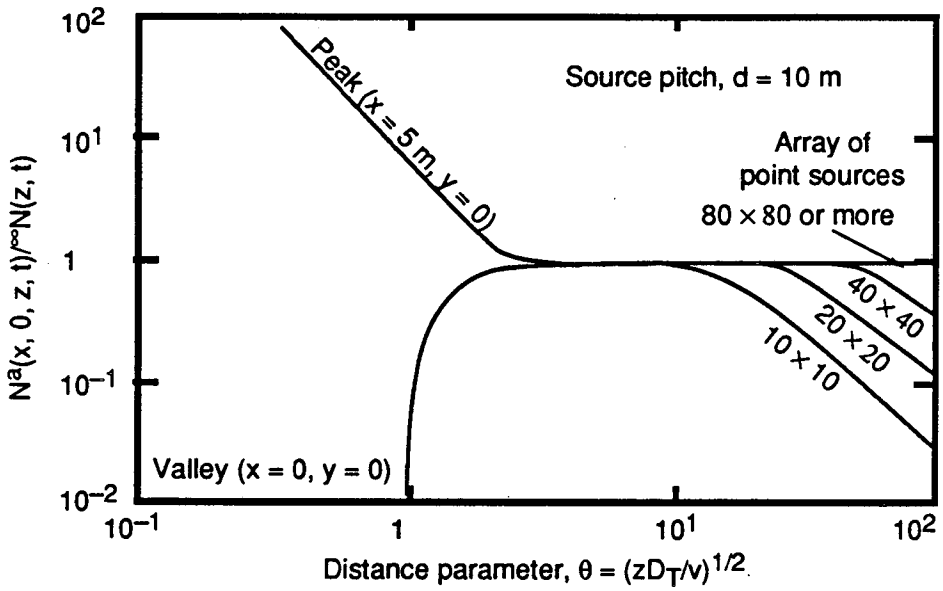

Figure 7.14 Relative concentration as a function of the distance parameter for an array of point sources at y = 0 for a porous medium.

7.6 Conclusions

From analyses on the single-patch solution, we can obtain the following insights:

(i) At a large downstream distance the concentration in the fracture shows a broad profile along the transverse direction. This is quite different from the behaviour of molecular diffusion into the rock matrix. At a large downstream distance matrix penetration by molecular diffusion is yet very shallow.

(ii) Transverse dispersion attenuates the concentrations significantly both in the fracture and in the rock matrix, but has no significant effect in retarding the movement of the

leading advection edge. This is also quite different from molecular diffusion into the rock matrix, which retards the movement of the advection edge significantly.

Comparing the multiple-patch concentration with the infinite-source or the equivalent-single-patch concentration, we can distinguish three regions using the distance parameter $\theta = (z\, D_T / v)^{1/2}$:

	Applicable Solutions		
Patch separation	multiple-patch	infinite-source	equivalent patch
10 m	$\theta \leq 3$ m	$3 \leq \theta \leq \theta_c$	$\theta_c \leq \theta$
5 m	$\theta \leq 1.5$ m	$1.5 \leq \theta \leq \theta_c$	$\theta_c \leq \theta$

where θ_c depends upon the number of patches. This table is valid for any nuclides, rock, time, and transverse distance in the region projected *m*-patch area. Close to the individual patch sources, plumes produced from multiple-patch sources are isolated from each other, and we must use the multiple-patch solution for evaluation of the concentration field. In a mid-region due to local transverse dispersion the plumes merged to one overall plume, and both the infinite-source and the equivalent-source approximation give identical results. At large distances downstream region the overall plume spreads out due to overall transverse dispersion. In the far field we can consider a repository as a single patch source for prediction of the resulting radionuclide concentration field.

The results presented here are similar to results for point-source arrays in porous media, because the size of patch sources used in the current analysis is small compared to the separation between patches.

References

[1] Chambré, P. L., T. H. Pigford, A. Fujita, T. Kanki, A. Kobayashi, H. Lung, D. Ting, Y. Sato, and S. J. Zavoshy, *Analytical Performance Models For Geologic Repositories,* Chapter 5, LBL-14842, 1982.

[2] Pigford, T. H., P. L. Chambré, M. Albert, M. Foglia, M. Harada, F. Iwamoto, T. Kanki, D. Leung, S. Masuda, S. Muraoka, and D. Ting, *Migration of*

Radionuclides Through Sorbing Media: Analytical Solutions — II, Chapter 4, LBL-11616, 1980.

[3] NAG library Mark 10, Numerical Algorithm Group

[4] Pigford, T. H., P. L. Chambré, M. Foglia, M. Harada, F. Iwamoto, T. Kanki, D. Leung, S. Masuda, S. Muraoka, and D Ting, *Migration of Radionuclides Through Sorbing Media: Analytical Solutions — II,* Chapter 4, LBL-11616, Lawrence Berkeley Laboratory, 1980.

Chapter 8

Transient Diffusion of Radionuclide from a Cylindrical Waste Solid into Fractured Porous Rock

8.1 Introduction

Analytical studies of the advective transport of dissolved contaminants through fractured rock in the previous chapters have emphasized the effect of molecular diffusion in the rock matrix in affecting the space-time-dependent concentration of the contaminant as it moves along the fracture. Matrix diffusion only in the direction normal to the fracture surface was assumed (see Figure 2.1). Such studies illustrate the far-field transport features of fractured media. To predict the time-dependent mass transfer from a long waste cylinder surrounded by porous rock and intersected by a fracture, a study to be shown in the present chapter includes diffusion from the waste-solid surface directly into porous rock, as well as the more realistic geometry shown in Figure 8.1.

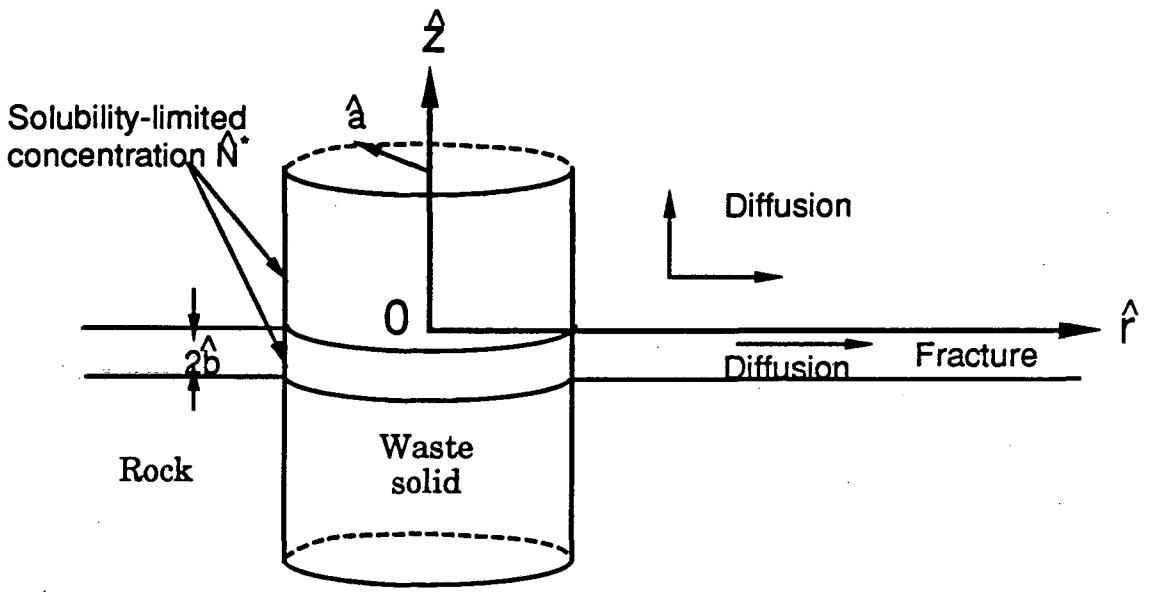

Figure 8.1 Cylindrical geometry and three dimensional diffusion in rock matrix and two dimensional diffusion in fracture. Angular symmetry is assumed.

In the following presented are the derivation of an analytical solution for the time-dependent mass transfer from the cylinder for the low-flow conditions wherein near-field mass transfer is expected to be controlled by molecular diffusion [1], and then description on computer-code implementation and numerical results obtained from the computer codes. The problem was first proposed and solved analytically by Chambré. The derivation is discussed below.

8.2 Assumptions and Mathematical Formulation

We consider a cylindrical waste solid of infinite length and constant radius $\hat{a}$ [m], intersected by a planar fracture (Figure 8.1). To make the model conservative, we assume that no waste container is present. An infinitely long cylinder is a good approximation for a long cylinder with negligible end effects. A constant concentration $\hat{N}^*$ [kg/m^3] of low-solubility dissolved species is prescribed in the water at the waste surface. The contaminant is transfered by molecular diffusion both in the fracture and in the rock matrix. The porosities of fracture and rock are ε_1 and ε_2, and water in pores is at rest. Notice that we assume that in some cases the fracture is filled with a certain material. If ε_1 is unity, then the fracture is completely open. Width of the fracture, $2\hat{b}$ [m], is considered to be much smaller than other dimensions such as the cylinder radius, so we assume that complete mixing across the width is achieved. Then, the concentrations in the fracture and in the rock matrix are described in two-, and three-dimensional cylindrical coordinate systems, respectively. Different properties are assumed for the local sorption equilibrium in the fracture and in the rock matrix. Radioactive decay is included without any precursors. If we assume angular symmetry, the governing equations for the space-time-dependent concentrations in the fracture and in the rock matrix are written as:

$$\hat{K}_1 \frac{\partial \hat{N}_1}{\partial \hat{t}} = \frac{\hat{D}_1}{\hat{r}} \frac{\partial}{\partial \hat{r}} \left(\hat{r} \frac{\partial \hat{N}_1}{\partial \hat{r}} \right) - \hat{\lambda} \hat{K}_1 \hat{N}_1 - \frac{\hat{q}(\hat{r}, \hat{t})}{\hat{b}}, \quad \hat{r} > \hat{a}, \quad \hat{t} > 0, \quad (8.1)$$

$$\hat{K}_2 \frac{\partial \hat{N}_2}{\partial \hat{t}} = \frac{\hat{D}_2}{\hat{r}} \frac{\partial}{\partial \hat{r}} \left(\hat{r} \frac{\partial \hat{N}_2}{\partial \hat{r}} \right) + \hat{D}_2 \frac{\partial^2 \hat{N}_2}{\partial \hat{z}^2} - \hat{\lambda} \hat{K}_2 \hat{N}_2 ,$$

$$\hat{t} > 0, \ \hat{r} > \hat{a}, \ \hat{z} > 0, \qquad (8.2)$$

where

$$\hat{q}(\hat{r}, \hat{t}) = -\varepsilon_2 \hat{D}_2 \left. \frac{\partial \hat{N}_2}{\partial \hat{z}} \right|_{\hat{z}=0}, \quad \hat{t} > 0, \ \hat{r} > \hat{a}, \qquad (8.3)$$

$\hat{N}_i$: contaminant concentration in water in region i [kg/m^3],

$\hat{D}_i$: diffusion coefficient of the nuclide in region i [m^2/yr],

$\hat{q}$: diffusive flux from the fracture to rock matrix at the interface between rock and fracture [kg/m^2·yr].

$\hat{K}_i$: retardation factor for region i, dimensionless, defined as

$$\hat{K}_i = 1 + \frac{1 - \varepsilon_i}{\varepsilon_i} \hat{K}d_i , \qquad (8.4)$$

$\hat{\lambda}$: radioactive decay constant [yr^{-1}],

ε_i : porosity of region i, dimensionless,

$\hat{r}$: distance from the center of the waste cylinder [m],

$\hat{z}$: distance from the interface between fracture and rock [m],

$\hat{t}$: time [yr], and

$\hat{K}d_i$: sorption distribution coefficients in region i between concentration in water phase and concentration in solid phase, dimensionless.

Subscripts 1 and 2 stand for fracture and rock, respectively. The symbol ^ is put to indicate that these quantities have actual physical dimensions; later we will introduce non-dimensionalization.

From the assumptions, we can set the side conditions as follows:

$$\hat{N}_1(\hat{r}, 0) = 0, \qquad \hat{r} > \hat{a}, \tag{8.5}$$

$$\hat{N}_2(\hat{r}, \hat{z}, 0) = 0, \qquad \hat{r} > \hat{a}, \quad \hat{z} > 0, \tag{8.6}$$

$$\hat{N}_1(\hat{a}, \hat{t}) = \hat{N}^*, \qquad \hat{t} > 0, \tag{8.7}$$

$$\hat{N}_1(\infty, \hat{t}) = 0, \qquad \hat{t} > 0, \tag{8.8}$$

$$\hat{N}_2(\hat{a}, \hat{z}, \hat{t}) = \hat{N}^*, \qquad \hat{z} > 0, \quad \hat{t} > 0, \tag{8.9}$$

$$\hat{N}_2(\infty, \hat{z}, \hat{t}) = 0, \qquad \hat{z} > 0, \quad \hat{t} > 0, \tag{8.10}$$

$$\hat{N}_2(\hat{r}, 0, \hat{t}) = \hat{N}_1(\hat{r}, \hat{t}), \qquad \hat{r} > \hat{a}, \quad \hat{t} > 0, \tag{8.11}$$

$$\left.\frac{\partial \hat{N}_2}{\partial \hat{z}}\right|_{\hat{z}\to\infty} = 0, \qquad \hat{r} > \hat{a}, \quad \hat{t} > 0. \tag{8.12}$$

(8.3) and (8.11) provide the coupling of the governing equations.

To simplify further mathematical manipulations, we introduce the following non-dimensionalization:

$$r \equiv \frac{\hat{r}}{\hat{a}}, \quad z \equiv \frac{\hat{z}}{\hat{a}}, \quad t \equiv \frac{\hat{D}_2 \hat{t}}{\hat{K}_2 \hat{a}^2}, \tag{8.13}$$

$$\Delta \equiv \frac{\hat{D}_1 \hat{K}_2}{\hat{D}_2 \hat{K}_1}, \quad b \equiv \frac{\hat{b}\hat{K}_1}{\varepsilon_2 \hat{a} \hat{K}_2}, \quad \lambda \equiv \frac{\hat{a}^2 \hat{\lambda} \hat{K}_2}{\hat{D}_2}, \tag{8.14}$$

and

$$N_1(r, t) \equiv \frac{\hat{N}_1(\hat{r}, \hat{t})}{\hat{N}^*}, \quad N_2(r, z, t) \equiv \frac{\hat{N}_2(\hat{r}, \hat{z}, \hat{t})}{\hat{N}^*}, \quad q \equiv \frac{\hat{a}}{\varepsilon_2 \hat{D}_2 \hat{N}^*} \hat{q}. \tag{8.15}$$

The variable t is called Fourier number, which measures the time of diffusion process. λ is called Thiele modulus. Then, the system of equations (8.1) to (8.3) and (8.5) to (8.12) can be rewritten as:

$$\frac{\partial N_1}{\partial t} = \frac{\Delta}{r}\frac{\partial}{\partial r}\left(r\frac{\partial N_1}{\partial r}\right) - \lambda N_1 - \frac{q}{b}, \qquad r > 1, \qquad t > 0, \tag{8.16}$$

$$\frac{\partial N_2}{\partial t} = \frac{1}{r}\frac{\partial}{\partial r}\left(r\frac{\partial N_2}{\partial r}\right) + \frac{\partial^2 N_2}{\partial z^2} - \lambda N_2, \qquad r > 1, \qquad z > 0, \qquad t > 0, \tag{8.17}$$

where

$$q(r, t) = -\left.\frac{\partial N_2}{\partial z}\right|_{z=0}, \qquad r > 1, \; t > 0, \tag{8.18}$$

subject to

$$N_1(r, 0) = 0, \qquad r > 1, \tag{8.19}$$

$$N_2(r, z, 0) = 0, \qquad r > 1, \qquad z > 0, \tag{8.20}$$

$$N_1(1, t) = 1, \qquad t > 0, \tag{8.21}$$

$$N_1(\infty, t) = 0, \qquad t > 0, \tag{8.22}$$

$$N_2(1, z, t) = 1, \qquad z > 0, \qquad t > 0, \tag{8.23}$$

$$N_2(\infty, z, t) = 0, \qquad z > 0, \qquad t > 0, \tag{8.24}$$

$$N_2(r, 0, t) = N_1(r, t), \qquad r > 1, \qquad t > 0, \tag{8.25}$$

$$\left.\frac{\partial N_2}{\partial z}\right|_{z \to \infty} = 0, \qquad r > 1, \qquad t > 0. \tag{8.26}$$

We will solve the problem (8.16) — (8.26). Since one of our major concerns here is mass transfer from the waste solid, we will derive the following auxiliary functions:

$$\hat{j}_1(\hat{a}, \hat{t}) \equiv -\varepsilon_1 \hat{D}_1 \left.\frac{\partial \hat{N}_1}{\partial \hat{r}}\right|_{\hat{r}=\hat{a}} = -\frac{\varepsilon_1 \hat{D}_1 \hat{N}^*}{\hat{a}} \left.\frac{\partial N_1}{\partial r}\right|_{r=1} = \frac{\varepsilon_1 \hat{D}_1 \hat{N}^*}{\hat{a}} j_1(t) \tag{8.27a}$$

where

$$j_1(t) \equiv -\left.\frac{\partial N_1}{\partial r}\right|_{r=1}, \tag{8.27b}$$

and

$$\hat{j}_2(\hat{a}, \hat{z}, \hat{t}) \equiv -\hat{\varepsilon}_2 \hat{D}_2 \left.\frac{\partial \hat{N}_2}{\partial \hat{r}}\right|_{\hat{r}=\hat{a}} = \frac{\hat{\varepsilon}_2 \hat{D}_2 \hat{N}^*}{\hat{a}} j_2(z, t) \qquad (8.28a)$$

where

$$j_2(z, t) \equiv -\left.\frac{\partial N_2}{\partial r}\right|_{r=1}. \qquad (8.28b)$$

(8.27a, b) and (8.28a, b) are considered as the diffusive fluxes of the nuclide at the waste surface from the waste to the fracture and to the porous rock, respectively. In the following sections analytical forms are obtained and numerical evaluations are shown for (8.18), (8.27b), and (8.28b) as well as for the concentrations $N_1(r, t)$ and $N_2(r, z, t)$.

8.3 Derivation of Analytical Solutions

The outline of the solution method is the following: First, apply Weber transform [2] with respect to r and Laplace transform with respect to t for (8.16) to (8.18). Second, solve the second-order ordinary differential equation resulting from (8.17) and obtain the double-transformed $q(z, t)$. Third, substitute the transformed q into the algebraic equation resulting from (8.16) and solve the resultant equation. Finally make the inverse transforms twice to obtain the solutions. Important steps to the solution are discussed below.

8.3.1 Application of Integral Transforms

The Weber transform of a function $f(r)$ for the domain $r > 1$ is defined as:

$$\bar{f}(s) \equiv \int_1^\infty f(r)\, \Phi(r, s)\, r dr, \quad s > 0, \qquad (8.29)$$

where s is a Weber variable, real, and

$$\Phi(r, s) \equiv J_0(rs)Y_0(s) - Y_0(rs)J_0(s), \qquad (8.30)$$

The overbar symbol stands for a Weber-transform of $f(r)$. With the following formula (see

Appendix E for derivation):

$$\int_1^\infty \frac{1}{r}\frac{\partial}{\partial r}\left(r\frac{\partial f}{\partial r}\right)\Phi(r,s)\,r dr = -\frac{2}{\pi}f(1) - s^2\bar{f}(s), \qquad s>0, \tag{8.31}$$

(8.16) and (8.17) can be transformed as

$$\frac{d\bar{N}_1}{dt} + \mu_1^2\bar{N}_1 + \frac{\bar{q}}{b} + \frac{2}{\pi}\Delta = 0, \qquad s>0, \qquad t>0, \tag{8.32}$$

$$\frac{\partial\bar{N}_2}{\partial t} + \mu_2^2\bar{N}_2 - \frac{\partial^2\bar{N}_2}{\partial z^2} + \frac{2}{\pi} = 0, \qquad s>0, \qquad z>0, \qquad t>0, \tag{8.33}$$

where

$$\mu_1^2 = s^2\Delta + \lambda, \qquad \mu_2^2 = s^2 + \lambda, \tag{8.34}$$

and the boundary conditions (8.21) and (8.23) have been used.

Next, we apply Laplace transform on (8.32) and (8.33) with the help of (4.13), obtaining

$$(\mu_1^2 + p)\tilde{\bar{N}}_1 + \frac{\tilde{\bar{q}}}{b} + \frac{2\Delta}{\pi}\frac{1}{p} = 0, \qquad s>0, \tag{8.35}$$

$$\frac{d^2\tilde{\bar{N}}_2}{dz^2} - (\mu_2^2 + p)\tilde{\bar{N}}_2 - \frac{2}{\pi}\frac{1}{p} = 0, \qquad s>0, \qquad z>0, \tag{8.36}$$

where p is a Laplace variable, complex, and the tilde, ~, stands for a resultant of Laplace transform. We will solve (8.36) subject to the boundary conditions:

$$\tilde{\bar{N}}_2(s,0,p) = \tilde{\bar{N}}_1(s,p), \qquad s>0, \tag{8.37a}$$

$$\left.\frac{d\tilde{\bar{N}}_2}{dz}\right|_{z\to\infty} = 0, \qquad s>0. \tag{8.37b}$$

The solution to (8.36) satisfying (8.37a,b) is written as

$$\tilde{\tilde{N}}_2(s,z,p) = \left\{\tilde{\tilde{N}}_1(s,p) + \frac{1}{p(p+\mu_2^2)}\frac{2}{\pi}\right\} e^{-z\sqrt{\mu_2^2+p}} - \frac{2}{\pi}\frac{1}{p(\mu_2^2+p)},$$

$$z \geq 0, \qquad s \geq 0. \tag{8.38}$$

To obtain $\tilde{\tilde{N}}_1(s,p)$, we need the expression for $\tilde{\tilde{q}}(s,p)$. Differentiating (8.38) with respect to z and setting z to be zero in the resultant expression, we obtain:

$$\tilde{\tilde{q}}(s,p) = \sqrt{\mu_2^2+p}\left\{\tilde{\tilde{N}}_1(s,p) + \frac{1}{p(\mu_2^2+p)}\frac{2}{\pi}\right\}. \tag{8.39}$$

Substitution of (8.39) into (8.35) yields

$$\tilde{\tilde{N}}_1(s,p) = -\frac{2}{\pi}\frac{1}{p}\left\{\frac{\Delta}{\tilde{g}(p)} + \frac{1}{b}\frac{1}{\tilde{g}(p)\sqrt{\mu_2^2+p}}\right\}, \quad s \geq 0 \tag{8.40}$$

where

$$\tilde{g}(p) = p + \mu_1^2 + \frac{1}{b}\sqrt{p+\mu_2^2}\,. \tag{8.41}$$

Finally, substituting (8.41) into (8.38) yields:

$$\tilde{\tilde{N}}_2(s,z,p) = \frac{2}{\pi}\frac{1}{p}\left\{-\frac{\Delta}{\tilde{g}(p)}e^{-z\sqrt{p+\mu_2^2}} - \frac{e^{-z\sqrt{p+\mu_2^2}}}{b\,\tilde{g}(p)\sqrt{p+\mu_2^2}} + \frac{e^{-z\sqrt{p+\mu_2^2}}}{p+\mu_2^2} - \frac{1}{p+\mu_2^2}\right\},$$

$$s \geq 0, \qquad z \geq 0. \tag{8.42}$$

8.3.2 Inversion of Integral Transforms

We first make inverse Laplace transforms of (8.40) and (8.42). Considering that

$$\tilde{g}(p-\mu_2^2) = (\sqrt{p}+\alpha)(\sqrt{p}+\beta), \tag{8.43}$$

where

$$\alpha \equiv \frac{1-\Gamma}{2b}, \qquad \beta \equiv \frac{1+\Gamma}{2b}, \qquad \Gamma = \sqrt{1-4b^2(\Delta-1)s^2}\,, \tag{8.44}$$

the reciprocal of $\tilde{g}$ in (8.40) and (8.42) can be reduced to

$$\frac{1}{\tilde{g}(p-\mu_2^2)} = \frac{1}{\beta-\alpha}\left\{\frac{1}{\sqrt{p}+\alpha} - \frac{1}{\sqrt{p}+\beta}\right\}. \tag{8.45}$$

Using (8.45) and the following inversion formulae [3]:

$$\mathcal{L}^{-1}\left[\frac{1}{p}\,\tilde{f}(p)\right] = \int_0^t f(\tau)\,d\tau, \tag{8.46a}$$

$$\mathcal{L}^{-1}\left[\frac{e^{-k\sqrt{p}}}{\sqrt{p}+a}\right] = \frac{1}{\sqrt{\pi t}}e^{-\frac{k^2}{4t}} - ae^{ak}e^{a^2t}erfc\left(a\sqrt{t}+\frac{k}{2\sqrt{t}}\right),\ k \geq 0, \tag{8.46b}$$

$$\mathcal{L}^{-1}\left[\frac{e^{-k\sqrt{p}}}{\sqrt{p}\left(\sqrt{p}+a\right)}\right] = e^{ak}e^{a^2t}erfc\left(a\sqrt{t}+\frac{k}{2\sqrt{t}}\right),\ k \geq 0, \tag{8.46c}$$

$$\mathcal{L}^{-1}\left[\frac{e^{-k\sqrt{p}}}{p}\right] = erfc\left(\frac{k}{2\sqrt{t}}\right),\quad k \geq 0, \tag{8.46d}$$

the Weber-, and Laplace-transformed solutions (8.40) and (8.42) can be inverted to:

$$\overline{N}_1(s,t) = -\frac{2}{\pi}\frac{1}{\beta-\alpha}\left[\left(\beta\Delta-\frac{1}{b}\right)F(\beta;0,t) - \left(\alpha\Delta-\frac{1}{b}\right)F(\alpha;0,t)\right],$$

$$s \geq 0,\qquad t \geq 0, \tag{8.47}$$

$$\overline{N}_2(s,z,t) = -\frac{2}{\pi}\int_0^t e^{-\mu_2^2\tau}erf\left(\frac{z}{2\sqrt{\tau}}\right)d\tau - \frac{2}{\pi}\frac{1}{\beta-\alpha}\left[\left(\beta\Delta-\frac{1}{b}\right)F(\beta;z;t)\right.$$

$$\left. - \left(\alpha\Delta-\frac{1}{b}\right)F(\alpha;z,t)\right],\quad s \geq 0,\ z \geq 0,\ t \geq 0, \tag{8.48}$$

where

$$F(x;z,t) = e^{xz}\int_0^t e^{(x^2-\mu_2^2)\tau}erfc\left(x\sqrt{\tau}+\frac{z}{2\sqrt{\tau}}\right)d\tau. \tag{8.49}$$

The integral $F(x;z,t)$ converges uniformly in s over $\{s \geq 0\}$ for $t \geq 0$ and $z \geq 0$ to

$$F(x;z,t) = \frac{1}{x^2-\mu_2^2}\left\{e^{-\mu_2^2t-\frac{z^2}{4t}}H\left(x\sqrt{t}+\frac{z}{2\sqrt{t}}\right) + \frac{x-\mu_2}{2\mu_2}e^{-\mu_2 z}erfc\left(\frac{z}{2\sqrt{t}}-\mu_2\sqrt{t}\right)\right.$$

$$\left. -\frac{x+\mu_2}{2\mu_2}e^{\mu_2 z}erfc\left(\mu_2\sqrt{t}+\frac{z}{2\sqrt{t}}\right)\right\},\quad t \geq 0,\ z \geq 0,\ s \geq 0, \tag{8.49a}$$

where

$$H(x) = e^{x^2} erfc(x),\ x\ complex. \tag{8.50}$$

The first integral in the right hand side of (8.48) can be obtained by setting $x = 0$ in (8.49a). Then, we obtain the Weber-transformed solutions as:

$$\overline{N}_1(s, t) = -\overline{W}_0(s) - \overline{W}_1(s; 0, t) - \overline{W}_2(s; 0, t) - \overline{W}_4(s; 0, t), \quad s \geq 0,\ t \geq 0, \tag{8.51}$$

$$\overline{N}_2(s, z, t) = -\overline{W}_0(s) - \overline{W}_1(s; z, t) - \overline{W}_2(s; z, t) + \overline{W}_3(s; z, t) - \overline{W}_4(s; z, t),$$

$$s \geq 0, \qquad z \geq 0, \qquad t \geq 0, \tag{8.52}$$

where

$$\overline{W}_0(s) = \frac{2}{\pi}\ \frac{1}{\mu_2^2}, \tag{8.53a}$$

$$\overline{W}_1(s; z, t) = \frac{1}{\pi}\ \frac{(\Delta - 1)\lambda}{\mu_2^2\left(\mu_1^2 - \frac{\mu_2}{b}\right)}\ e^{z\mu_2} erfc\left(\frac{z}{2\sqrt{t}} + \mu_2\sqrt{t}\right), \tag{8.53b}$$

$$\overline{W}_2(s; z, t) = \frac{1}{\pi}\ \frac{(\Delta - 1)\lambda}{\mu_2^2\left(\mu_1^2 + \frac{\mu_2}{b}\right)}\ e^{-z\mu_2} erfc\left(\frac{z}{2\sqrt{t}} - \mu_2\sqrt{t}\right), \tag{8.53c}$$

$$\overline{W}_3(s; z, t) = \frac{2}{\pi}\ \frac{1}{\mu_2^2}\ e^{-\mu_2^2 t} erf\left(\frac{z}{2\sqrt{t}}\right), \tag{8.53d}$$

and

$$\overline{W}_4(s; z, t) = \frac{2}{\pi}\ \frac{e^{-\frac{z^2}{4t} - \mu_2^2 t}}{\beta - \alpha}\left\{\frac{\beta\Delta - \frac{1}{b}}{\beta^2 - \mu_2^2} H\left(\beta\sqrt{t} + \frac{z}{2\sqrt{t}}\right) - \frac{\alpha\Delta - \frac{1}{b}}{\alpha^2 - \mu_2^2} H\left(\alpha\sqrt{t} + \frac{z}{2\sqrt{t}}\right)\right\}. \tag{8.53e}$$

Because of the uniform convergence in (8.49a) with respect to s, we can make inverse Weber transforms on (8.51) and (8.52) without any restriction on s, obtaining

$$N_1(r, t) = \frac{K_0\left(\sqrt{\lambda}\, r\right)}{K_0\left(\sqrt{\lambda}\right)} - \left\{I_1(r, 0, t) + I_2(r, 0, t) + I_4(r, 0, t)\right\}, r \geq 1,\ t \geq 0, \tag{8.54}$$

$$N_2(r, z, t) = \frac{K_0\left(\sqrt{\lambda}\, r\right)}{K_0\left(\sqrt{\lambda}\right)} - \left\{I_1(r, z, t) + I_2(r, z, t) - I_3(r, z, t) + I_4(r, z, t)\right\},$$

$$r \geq 1, \qquad z \geq 0, \qquad t \geq 0, \tag{8.55}$$

where

$$I_i(r, z, t) = \int_0^\infty \overline{W}_i(s; z, t) \frac{\Phi(r, s)\, s\, ds}{\left[M_0(s)\right]^2}, \qquad i = 1, 2, 3, 4, \tag{8.56}$$

$$M_0(s) = \sqrt{\left[J_0(s)\right]^2 + \left[Y_0(s)\right]^2}, \tag{8.57}$$

and $K_0(x)$ modified Bessel function of the zeroth order, $J_0(x)$ and $Y_0(x)$ Bessel functions of the zeroth order, and $\Phi(r, s)$ is defined by (8.30). The first term in the right hand side of (8.54) and (8.55) is obtained by the inverse transform of $\overline{W}_0(s)$ (see Appendix D for derivation).

(8.54) and (8.55) are the final solutions for the problem (8.16) to (8.26). The diffusive fluxes from the waste solid to the fracture and to the rock matrix can be calculated as follows:

$$j_1(t) = \sqrt{\lambda}\, \frac{K_1\left(\sqrt{\lambda}\right)}{K_0\left(\sqrt{\lambda}\right)} - \frac{2}{\pi}\left\{I_1'(0, t) + I_2'(0, t) + I_4'(0, t)\right\}, \; t > 0, \tag{8.58}$$

$$j_2(z, t) = \sqrt{\lambda}\, \frac{K_1\left(\sqrt{\lambda}\right)}{K_0\left(\sqrt{\lambda}\right)} - \frac{2}{\pi}\left\{I_1'(z, t) + I_2'(z, t) - I_3'(z, t) + I_4'(z, t)\right\},$$

$$z \geq 0, \qquad t > 0, \tag{8.59}$$

where

$$I_i'(z, t) = \int_0^\infty \overline{W}_i(s; z, t) \frac{s\, ds}{\left[M_0(s)\right]^2}, \qquad i = 1, 2, 3, 4 \tag{8.60}$$

and the identity [4]:

$$\left.\frac{\partial \Phi(r, s)}{\partial r}\right|_{r=1} = -s\left\{J_1(s)\, Y_0(s) - J_0(s)\, Y_1(s)\right\} = -\frac{2}{\pi} \tag{8.61}$$

is used on the course of the derivation.

By differentiating (8.52) with respect to z and setting z to be zero, we obtain the diffusive mass flux from the fracture to the rock matrix at the interface as:

$$q(r, t) = -I_5''(r, t) + I_6''(r, t), \tag{8.62}$$

where

$$I_i''(r, t) = \int_0^\infty \overline{W}_i(s; t) \frac{\Phi(r, s)}{\left[M_0(s)\right]^2} s\, ds, \quad i = 5, 6, \tag{8.63a}$$

$$\overline{W}_5(s; t) = \frac{2}{\pi}(\Delta - 1)\lambda \frac{-\frac{1}{b} + \frac{\mu_1^2}{\mu_2} erf\left(\mu_2\sqrt{t}\right)}{\mu_1^4 - \frac{\mu_2^2}{b^2}}, \tag{8.63b}$$

$$\overline{W}_6(s; t) = \frac{2}{\pi} \frac{e^{-\mu_2^2 t}}{\beta - \alpha} \left\{ \frac{\beta(\beta\Delta - \frac{1}{b})}{\beta^2 - \mu_2^2} H\left(\beta\sqrt{t}\right) - \frac{\alpha(\alpha\Delta - \frac{1}{b})}{\alpha^2 - \mu_2^2} H\left(\alpha\sqrt{t}\right) \right\}. \tag{8.63c}$$

8.4 Mathematical Preparation for Numerical Evaluation

8.4.1 Classification with Δ

We must consider three cases, $\Delta > 1$, $\Delta = 1$, and $\Delta < 1$, separately. By definition of Δ, (8.14), $\Delta > 1$ means that diffusion is faster in the fracture than in the rock matrix, which can be considered as the most likely case. The case $\Delta < 1$ could happen if the fracture is filled with highly sorbing material such as clay. In the case of $\Delta = 1$, the waste cylinder is surrounded entirely by porous rock. The solution to $N_1(r, t)$, (8.54), becomes identical to that to $N_2(r, z, t)$, (8.55). By setting Δ to be unity, we have:

$$\overline{W}_1(s; z, t) = \overline{W}_2(s; z, t) = 0, \quad z \geq 0, \; t \geq 0, \; s \geq 0,$$

and $\alpha = 0$, $\beta = \frac{1}{b}$. Therefore,

$$\overline{W}_4(s;\, z,\, t) = -\frac{2}{\pi}\,\frac{e^{-\mu_2^2 t}}{\mu_2^2}\; erfc\left(\frac{z}{2\sqrt{t}}\right).$$

Then, (8.54) and (8.55) both reduce to

$$N_1(r,\, t) = N_2(r,\, t) = \frac{K_0\left(\sqrt{\lambda}\, r\right)}{K_0\left(\sqrt{\lambda}\right)} + \frac{2}{\pi}\int_0^{\infty} \frac{e^{-\mu_2^2 t}}{\mu_2^2}\,\frac{\Phi(r,\, s)}{\left[M_0(s)\right]^2}\; s\, ds. \qquad (8.64)$$

Notice that (8.64) is independent of z. For a stable nuclide ($\lambda = 0$), the first term in the right hand side of (8.64) becomes unity, and the solution (8.64) becomes identical to the solution for temperature in the region internally bounded by the circular cylinder with a constant temperature at the boundary, obtained by *Carslaw and Jaeger* [5].

From the standpoint of safety assessment of waste disposal, $\Delta > 1$ can be considered as the most undesirable case. So we assume $\Delta > 1$ below. In the rest of this section we take $N_2(r, z, t)$ and consider mathematical preparation for numerical evaluation. j_1, j_2, and q can be treated in a very similar way.

8.4.2 Evaluation of $I_4(r, z, t)$

Assuming $\Delta > 1$ results in evaluation of complementary error functions of a complex argument in $\overline{W}_4(s; z, t)$, (8.53e). From (8.44) α and β become complex for s in

$$s > s_o \equiv \frac{1}{2b\sqrt{\Delta - 1}}\,. \qquad (8.65)$$

Therefore, we must divide $I_4(r, z, t)$ into two parts:

$$I_4(r,\, z,\, t) = I_{41}(r,\, z,\, t) + I_{42}(r,\, z,\, t), \qquad (8.66)$$

where

$$I_{41}(r,\, z,\, t) = \int_0^{s_o} \overline{W}_4(s;\, z,\, t)\,\frac{\Phi(r.\, s)}{\left[M_0(s)\right]^2}\; s\, ds, \qquad (8.67a)$$

$$I_{42}(r, z, t) = \int_{s_o}^{\infty} \overline{W}_4(s; z, t) \frac{\Phi(r, s)}{\left[M_0(s)\right]^2} \, s \, ds, \qquad (8.67b)$$

$$\overline{W}_4(s; z, t) = \left\{ w(\beta; z, t) - w(\alpha; z, t) \right\} \frac{2}{\pi} e^{-\frac{z^2}{4t} - \lambda t} \qquad (8.67c)$$

and

$$w(x; z, t) = \frac{e^{-s^2 t}}{\beta - \alpha} \frac{x\Delta - \frac{1}{b}}{x^2 - \mu_2^2} H\left(x\sqrt{t} + \frac{z}{2\sqrt{t}} \right), \qquad x = \alpha, \beta. \qquad (8.67d)$$

(a) $I_{41}(r, z, t)$

By variable transform from s to Γ, defined as

$$s^2 = (1 - \Gamma^2) s_o^2 , \qquad (8.68)$$

the integration interval is changed to $0 \le \Gamma \le 1$, and $I_{41}(r, z, t)$ can be written as

$$I_{41}(r, z, t) = \frac{2}{\pi} e^{-\frac{z^2}{4t} - \lambda t} \frac{1}{2} \left\{ I_{41}^{+}(r, z, t) - I_{41}^{-}(r, z, t) \right\}, \qquad (8.69)$$

where

$$I_{41}^{\pm}(r, z, t) = \int_0^1 e^{-(1-\Gamma^2) s_o^2 t} w_{\pm}(\Gamma; z, t) \frac{\Phi\left(r, s_o\sqrt{1-\Gamma^2} \right)}{\left[M_0\left(s_o\sqrt{1-\Gamma^2} \right) \right]^2} \, d\Gamma, \qquad (8.70a)$$

$$w_{\pm}(\Gamma; z, t) = \frac{\Delta\Gamma \pm (\Delta - 2)}{\left\{ \Delta\Gamma \pm (\Delta - 2) \right\}(1 \pm \Gamma) - \frac{\lambda}{s_o^2}} H\left(\frac{\sqrt{t}}{2b}(1 \pm \Gamma) + \frac{z}{2\sqrt{t}} \right). \qquad (8.70b)$$

Assuming $\lambda \neq 0$, one may notice that either w_+ or w_- has a singularity inside $0 \le \Gamma \le 1$, depending on the values of Δ, b, and λ. If $1 < \Delta \le 2 + \lambda/s_0^2$, then $w_+(\Gamma; z, t)$ becomes singular at $\Gamma = \Gamma_s = \{1 - \Delta + \sqrt{1 + \lambda\Delta/s_0^2}\}/\Delta$. If $\Delta > 2 + \lambda/s_0^2$, then $w_-(\Gamma; z, t)$ becomes singular at $\Gamma = \Gamma_s = \{\Delta - 1 - \sqrt{1 + \lambda\Delta/s_0^2}\}/\Delta$. These singular points are never

the end-point of the integration interval, and so $I_{41}^{\pm}(r, z, t)$ can be considered as Hilbert transform:

$$I_{41}^{\pm}(r, z, t) = \int_0^1 \frac{f(\Gamma)}{(\Gamma - \Gamma_s)}\, d\Gamma, \quad 0 < \Gamma_s < 1, \tag{8.71}$$

where $f(\Gamma)$ can be obtained from (8.70 a,b). The integral is interpreted as a Cauchy principal value. D01AQF from NAG library [6] is the suitable package subroutine for this type of integration. The subroutine employs modified Clenshaw-Curtis integration scheme [7] and global acceptance criterion for error estimation [8]. The same type of singularity is found also in $I_1(r, z, t)$.

If $\lambda = 0$, $w_-(\Gamma; z, t)$ has an end-point singularity at $\Gamma = 1$, while $w_+(\Gamma; z, t)$ has no singularity point inside the interval. This singularity can be removed by the variable transformation from Γ to ξ by

$$\Gamma = 1 - e^{-\xi}. \tag{8.72}$$

Then, $\bar{I}_{41}$ reduces to

$$\bar{I}_{41}(r, z, t) = \int_0^{\infty} e^{-s_o^2 tA} H\left(\frac{\sqrt{t}}{2b} e^{-\xi} + \frac{z}{2\sqrt{t}}\right) \frac{\Phi\left(r, s_o\sqrt{A}\right)}{\left[M_0\left(s_o\sqrt{A}\right)\right]^2}\, d\xi, \tag{8.73}$$

where $A \equiv 2e^{-\xi} - e^{-2\xi}$. As ξ tends to infinity, A tends to zero, and the H function tends to $H(z/2\sqrt{t})$. If A approaches to zero, $Y_0(s_o\sqrt{A})$ in Φ and M_0 tends to $-\infty$. To avoid this difficulty, let us consider the following polynomial approximation [9]:

$$Y_0(x) = \frac{2}{\pi} \ln\left(\frac{x}{2}\right) J_0(x) + a_0 + a_1\left(\frac{x}{3}\right)^2 + a_2\left(\frac{x}{3}\right)^4 + \ldots + a_6\left(\frac{x}{3}\right)^{12} + \varepsilon$$

$$0 < x \le 3, \quad |\varepsilon| < 1.4 \times 10^{-8}, \tag{8.74}$$

where

$$a_0 = 0.36746691, \quad a_1 = 0.60559366, \quad a_2 = -0.74350384, \quad a_3 = 0.25300117$$

$$a_4 = -0.04261214, \quad a_5 = 0.00427916, \quad a_6 = -0.00024846$$

Substituting $s_o\sqrt{A}$ into x in (8.74), we may approximate $Y_0(s_o\sqrt{A})$, for large ξ, by

$$Y_0(s_o\sqrt{A}) \approx \frac{1}{\pi}\left(\ln\frac{s_o^2}{2} - \xi\right) + a_0, \quad J_0(s_o\sqrt{A}) \approx 1. \tag{8.75}$$

Then, $\Phi(r, s_o\sqrt{A})$ can be approximated, for large ξ, by

$$\Phi(r, s_o\sqrt{A}) \approx \frac{1}{\pi}\ln\left(\frac{1}{r}\right), \tag{8.76}$$

and $[M_0(s_o\sqrt{A})]^2$ becomes proportional to (ξ^2 + const) for large ξ. Thus in the interval $[\xi_c, \infty)$, where ξ_c is determined so that the approximation (8.75) holds, (8.73) can be calculated as [10]

$$\begin{aligned} &H\left(\frac{z}{2\sqrt{t}}\right)\frac{1}{\pi}\ln\frac{1}{r}\int_{\xi_c}^{\infty}\left[1+\left\{\frac{1}{\pi}\left(\ln\frac{s_o^2}{2}-\xi\right)+a_0\right\}^2\right]^{-1}d\xi \\ &=\frac{1}{\pi}\ln\frac{1}{r}\,H\left(\frac{z}{2\sqrt{t}}\right)\left\{\frac{\pi}{2}-\tan^{-1}\left(\frac{\xi_c-\pi a_0-\ln\left(s_o^2/2\right)}{\pi}\right)\right\}. \end{aligned} \tag{8.77}$$

In the rest of the interval, i.e., $[0, \xi_c]$, (8.73) is evaluated numerically by Gaussian quadratures without any difficulties. The same type of singularity occurs also in $I_3(r, z, t)$.

(b) $I_{42}(r, z, t)$

In the interval $s > s_o$, α and β become complex. For a complex argunent, error function can be evaluated by the following formula [11]:

$$erf(x + yi) = R(x, y) + i\,I(x, y), \tag{8.78a}$$

where

$$R(x, y) = erf(x) + \frac{e^{-x^2}}{2\pi x}\left(1 - \cos 2xy\right) + \frac{2}{\pi}e^{-x^2}\sum_{n=1}^{\infty}\frac{e^{-\frac{1}{4}n^2}}{n^2 + 4x^2}\,f_n(x, y), \tag{8.78b}$$

$$I(x, y) = \frac{e^{-x^2}}{2\pi x}\sin 2xy + \frac{2}{\pi}e^{-x^2}\sum_{n=1}^{\infty}\frac{e^{-\frac{1}{4}n^2}}{n^2 + 4x^2}\,g_n(x, y), \tag{8.78c}$$

$$f_n(x, y) = 2x - 2x\cosh(ny)\cos(2xy) + n\cdot\sinh(ny)\sin(2xy), \qquad (8.78d)$$

and

$$g_n(x, y) = 2x\cosh(ny)\sin(2xy) + n\cdot\sinh(ny)\cos(2xy). \qquad (8.78e)$$

With (8.78a–e) and the variable transformation:

$$\gamma = \sqrt{\frac{s^2}{s_o^2} - 1}, \qquad (8.79)$$

$I_{42}(r, z, t)$ can be rewritten as follows:

$$I_{42}(r, z, t) = \frac{2}{\pi} e^{-\frac{z^2}{4t} - \lambda t} e^{-s_o^2 t} \left\{ \phi\left(\frac{b}{\sqrt{t}}\Omega\right) I_{421}(r, z, t) - I_{422}(r, z, t) \right\}, \qquad (8.80)$$

where

$$I_{421}(r, z, t) = \int_0^\infty \frac{e^{-\Delta s_o^2 t\gamma^2}}{D(\gamma)} \left\{ A(\gamma)\sin(\Omega\gamma) - B(\gamma)\cos(\Omega\gamma) \right\} \frac{\Phi\left(r, s_o\sqrt{1+\gamma^2}\right)}{\left[M_0\left(s_o\sqrt{1+\gamma^2}\right)\right]^2} d\gamma,$$

$$I_{422}(r, z, t) = \int_0^\infty \frac{e^{-s_o^2 t\gamma^2}}{D(\gamma)} S(\gamma) \frac{\Phi\left(r, s_o\sqrt{1+\gamma^2}\right)}{\left[M_0\left(s_o\sqrt{1+\gamma^2}\right)\right]^2} d\gamma \qquad (8.81b)$$

$$\phi(x) = H(x) - \frac{1}{2\pi x} - \frac{4x}{\pi} \sum_{n=1}^{\infty} \frac{e^{-\frac{1}{4}n^2}}{n^2 + 4x^2}, \qquad (8.81c)$$

$$A(\gamma) = \sigma(\gamma) - (\Delta - 2)\frac{\lambda}{s_o^2}, \qquad B(\gamma) = \gamma\left\{\sigma(\gamma) + \frac{\lambda}{s_o^2}\Delta\right\}, \qquad (8.81d)$$

$$D(\gamma) = (\gamma^2+1)\,\sigma(\gamma) + \frac{2\lambda}{s_o^2}\left(\Delta\gamma^2 - \Delta + 2\right) + \frac{\lambda^2}{s_o^4}, \qquad (8.81e)$$

$$S(\gamma) = \frac{B(\gamma)}{2\pi x} e^{-\frac{r\gamma^2}{4b^2}} + \frac{1}{\pi} \sum_{n=1}^{\infty} \frac{\left(2xB(\gamma) + nA(\gamma)\right)}{n^2+4x^2} e^{-\frac{1}{4}\left(n - \frac{\sqrt{t}}{b}\gamma\right)^2} +$$

$$+\frac{1}{\pi}\sum_{n=1}^{\infty}\frac{\{2xB(\gamma)-nA(\gamma)\}}{n^2+4x^2}\,e^{-\frac{1}{4}\left(n+\frac{\sqrt{t}}{b}\gamma\right)^2}, \qquad (8.81f)$$

$$\sigma(\gamma)=\Delta^2\gamma^2+(\Delta-2)^2, \quad \Omega=\frac{t}{2b^2}+\frac{z}{2b}, \quad x=\frac{b}{\sqrt{t}}\Omega. \qquad (8.81g)$$

The function $\phi(x)$ vanishes quite rapidly for $x > 1$. Therefore, $I_{421}(r, z, t)$ may be evaluated only for $x < 1$.

8.4.3 Oscillation of Integrands

Due to the presence of $\Phi(r, s)$, all integrands in $N_1(r, t)$, $N_2(r, z, t)$, and $q(r, t)$ oscillate. How rapidly they oscillate depends on how large r is. For the cases of $I_3(r, z, t)$ and $I_4(r, z, t)$, the integrands vanish quite rapidly because of the term, $\exp(-\mu_2^2 t)$, so that the integration interval can be considered to be finite. If the computer underflow limit is e^{-U}, then the integration may be performed in the interval of $0 \le s \le \sqrt{\frac{U}{t}-\lambda}$. On the other hand in case of $I_1(r, z, t)$ and $I_2(r, z, t)$, their integrands vanish much slower, so one may have to integrate over hundreds of cycles of oscillation to evaluate the integrals with enough accuracy. For such slowly convergent integrands, ε^1-transformation for slowly convergent series and integrals [12] is employed.

8.5 Numerical Evaluations

Computer programs are implemented for $N_2(r, z, t)$, $j_2(z, t)$ and $q(r, t)$. $N_1(r, t)$ and $j_1(t)$ can be calculated by setting $z = 0$ in the input data for the programs for $N_2(r, z, t)$, and $j_2(z, t)$, respectively. Programs are written in FORTRAN 77.

8.5.1 Input Data

We assume that the waste solid comes from the spent fuel of the pressurized water reactor. The radius of the cylinder is $\hat{a} = 25$ cm. Fracture width $2\hat{b}$ is 1 cm. Surrounding

rock has porosity $\varepsilon_2 = 0.01$ whereas the fracture has no filling material ($\varepsilon_1 = 1$). The diffusion coefficient is the same for both fracture and rock, and is conservatively chosen as that for a liquid continuum (500 cm^2/yr). Sorption in the fracture walls is neglected ($\hat{K}_1 = 1$) while sorption in rock matrix is assumed to retard diffusion process by the factor of $\hat{K}_2 = 500$. Three actinides and a stable nuclide are compared in the numerical results: ^{234}U ($\hat{\lambda} = 2.806 \times 10^{-6}\ yr^{-1}$), ^{241}Am ($\hat{\lambda} = 1.513 \times 10^{-3}\ yr^{-1}$), and ^{239}Pu ($\hat{\lambda} = 2.841 \times 10^{-5}\ yr^{-1}$). With these values, non-dimensionalized parameters can be calculated as:

$$b = 0.004, \qquad \Delta = 500, \qquad t = 1.6 \times 10^{-3}\,\hat{t}\ [yr]$$

and

$$\lambda = 1.754 \times 10^{-3}\ for\ ^{234}U,\ \lambda = 0.9456\ for\ ^{241}Am, \quad and\ \lambda = 1.7755 \times 10^{-2}\ for\ ^{239}Pu$$

8.5.2 Features of Diffusive Mass Transfer in Cylindrical Geometry

Figure 8.2 gives an overall idea of how the contaminant is transfered from the cylinder, and is transported in the fractured porous rock. There shown are instantaneous concentration isopleths, mass flux from the cylinder to rock, mass flux to fracture, and flux across the rock/fracture interface for ^{239}Pu at Fourier number $t = 1$, which corresponds to 625 yr for the parameter values shown above. Concentration in rock is larger near the cylinder and near the fracture. Concentration isopleth shows that influence of the fracture in rock matrix becomes negligible beyond five radii from the rock/fracture interface. The mass flux into the fracture is calculated to be about two orders of magnitude greater than that into the rock matrix because of the assumed hundred-fold greater porosity in the fracture. The mass flux into the rock matrix becomes smaller in the vicinity of the fracture because contaminant diffusing from the fracture reduces the concentration difference between the surface of the cylinder and inside the rock matrix.

The mass flux across the interface between rock and fracture is zero at the surface of the cylinder ($r = 1$) because of the boundary conditions at $r = 1$. Then, the concentration difference increases with the distance from the cylinder surface because due to the assumed

larger retardation factor and smaller porosity in rock matrix, concentration in the rock matrix decreases faster than in the fracture. Mass flux across the interface starts to decrease after it reaches the maximum because both concentrations in the fracture and in the rock matrix approach to zero.

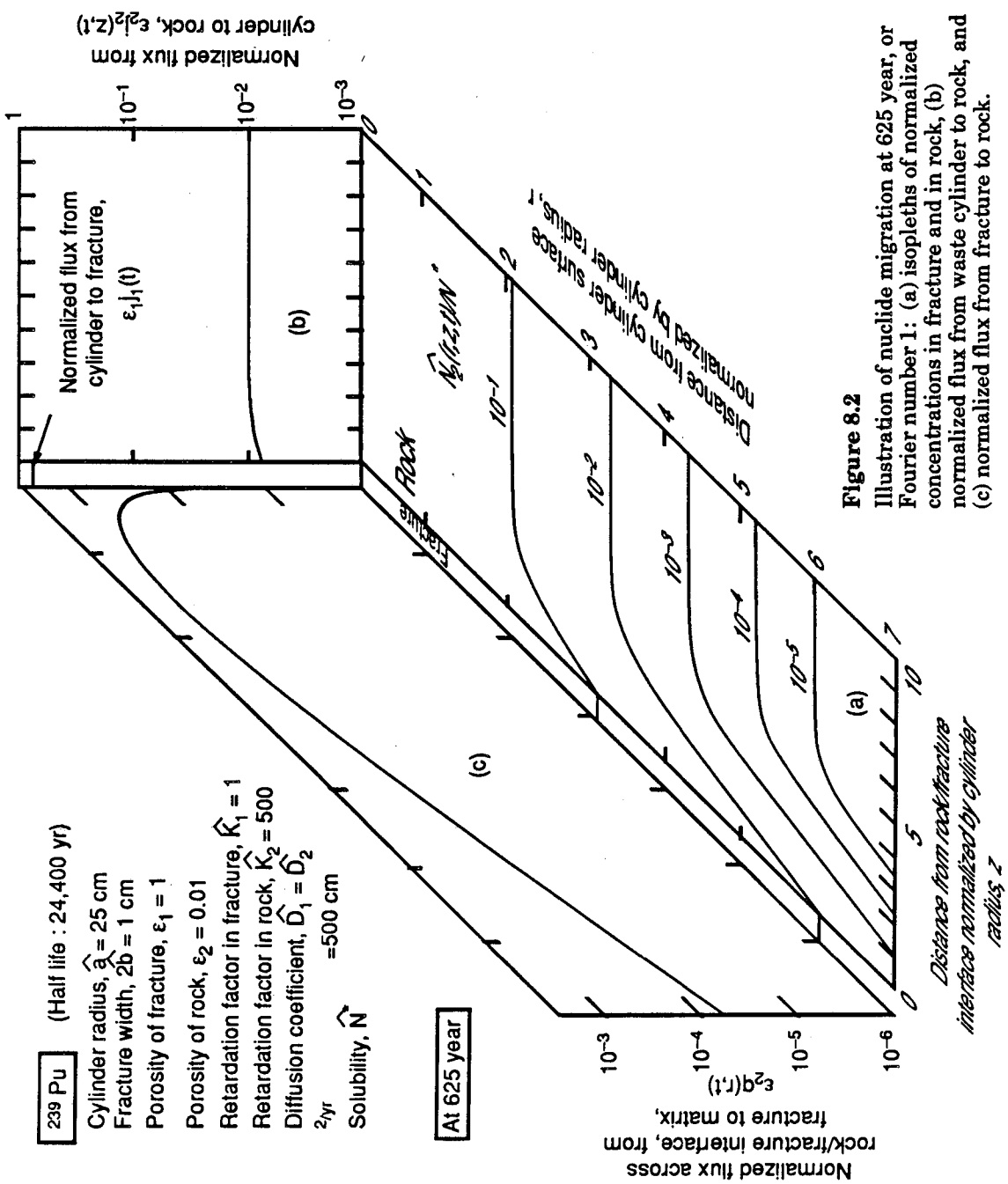

Figure 8.2
Illustration of nuclide migration at 625 year, or Fourier number 1: (a) isopleths of normalized concentrations in fracture and in rock, (b) normalized flux from waste cylinder to rock, and (c) normalized flux from fracture to rock.

Figure 8.3 shows the changes of mass flux from the cylinder to the fracture with Fourier number for three actinides and a stable nuclide. In very early times effect of decay is not apparent. Curves for shorter half-life nuclides deviate from that for a stable nuclide at an earlier time, and reach the steady state. For a stable nuclide the mass flux approaches to zero as time increases. Because of the loss by radioactive decay during diffusion in the medium, less amount will reach a certain point from the surface for shorter half-life nuclides. Therefore, in the steady state the concentration gradient becomes steeper for shorter half-life nuclides. Thus, radioactive decay enhances the mass transfer from the cylinder to the rock matrix and to the fracture.

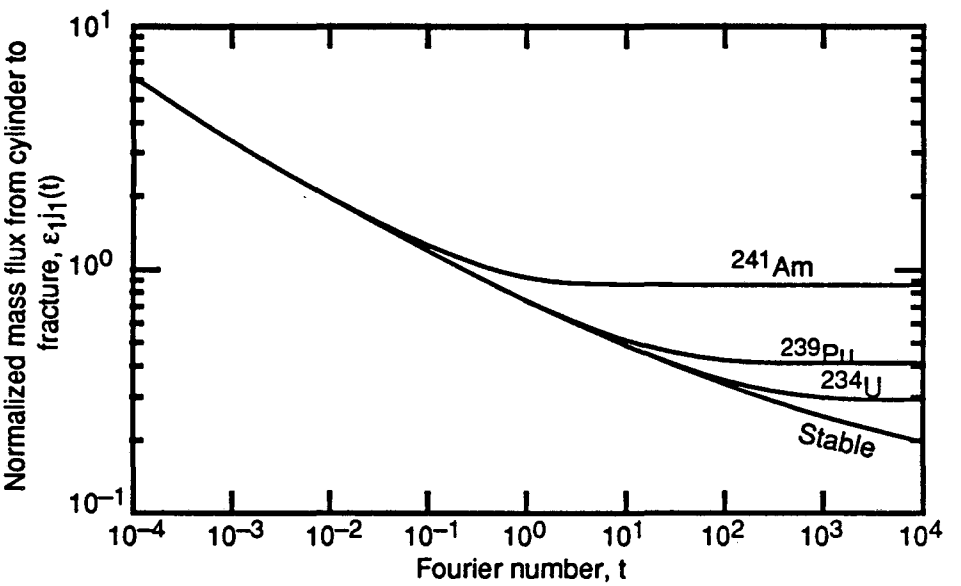

Figure 8.3 Mass fluxes for three radionuclides and a stable nuclide from the cylinder to the fracture at the cylinder surface as a function of time. Parameters from Figure 8.2 apply.

In Figure 8.4 mass flux of ^{239}Pu from the cylinder to the rock matrix is depicted as a function of Fourier number. The location $z = 0+$ is considered to be located at the rock-matrix side of the interface. The curve for $z = 0+$ is, therefore, hundred-fold less than that for $j_1(t)$, shown in the previous figure. In very early times effect of the fracture is limited

in the very vicinity of the fracture in the rock matrix, but the mass flux from the cylinder in the fracture-affected region is much lower than the mass flux in the rest of the cylinder surface in the rock matrix. For example, at $t = 10^{-3}$, in $z > 0.1$, the mass flux from the cylinder is virtually uniform, but the difference between the flux in the region $z > 0.1$ and the flux at the interface is large. As time increases, the affected region extends while the difference between the affected and not-affected regions becomes very small. At $t = 10^{2}$ and later we no longer observe significant difference.

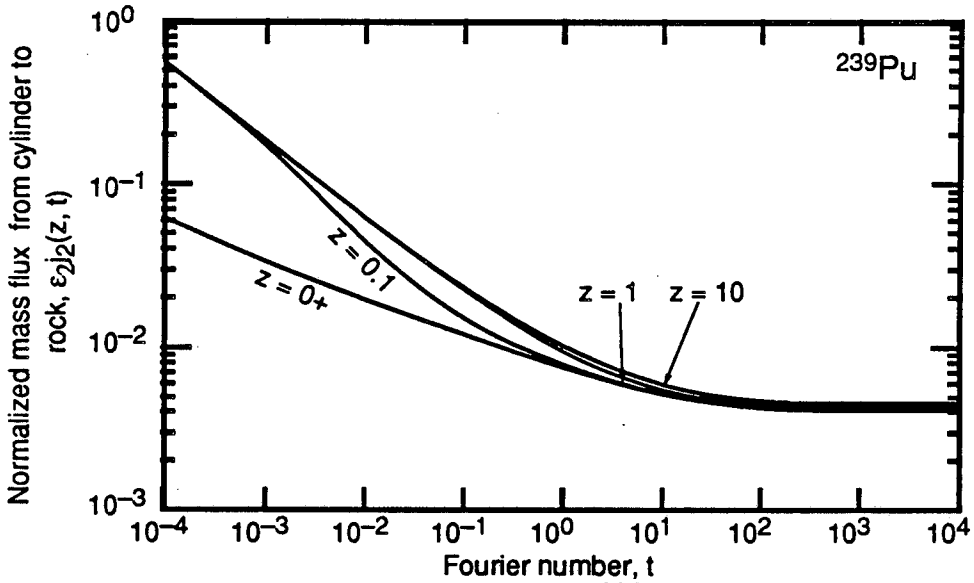

Figure 8.4 Normalized mass flux of ^{239}Pu from the cylinder to the rock matrix at the cylinder surface as a function of Fourier number. Four curves depict the effect of diffusion from the fracture to the rock matrix. Parameters from Figure 8.2 apply.

Figure 8.5 illustrates the effect of Thiele modulus, or radioactive decay on the mass flux to the fracture. In early times for long half-life nuclides radioactive decay has no effect. At $t = 10^{-2}$ only ^{90}Sr and ^{3}H can feel the effect slightly. By $t = 10^{2}$ for almost all radionuclides, which are of interest in waste disposal, mass flux is affected by radioactive decay. A curve for each Fourier number starts to increase at some value of Thiele modulus. Curves merge with each other, and for large Thiele modulus, become expressed with the first term in the right hand side of (8.82).

Figure 8.6 shows the profiles of the mass flux of ^{239}Pu at the rock/fracture interface from the fracture to the rock matrix as a function of distance from the waste surface. Important observation is that there is a maximum along r, which is quite different from what has been observed in the planar geometry in Chapter 2. The comparison between the cylinder model and the planar model is made in Section 8.5.4. At r =1, the mass flux is zero because of the boundary conditions (8.21) and (8.23). Because diffusion in rock matrix is slower than in the fracture, concentration in the fracture is always larger than that in rock matrix if compared at the same distance from the cylinder surface. As r tends to infinity, both concentrations tend to zero. Therefore, there should be a maximum mass flux in between r =1 and infinity. The maximum value decreases and the location of the maximum advances with time. Because the both concentrations approach to the steady state, the profile for $t = 10^4$ shows slight change from $t = 10^2$.

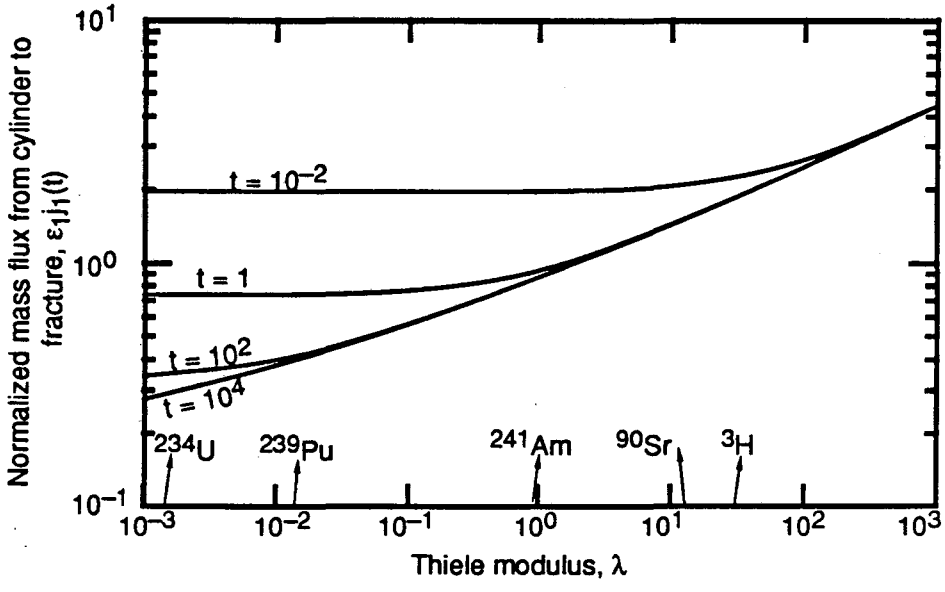

Figure 8.5 Mass flux from the cylinder to the fracture as a function of Thiele modulus. Typical radionuclides are indicated at the corresponding Thiele moduli, which can be calculated by assuming the parameter values applied in Figure 8.2.

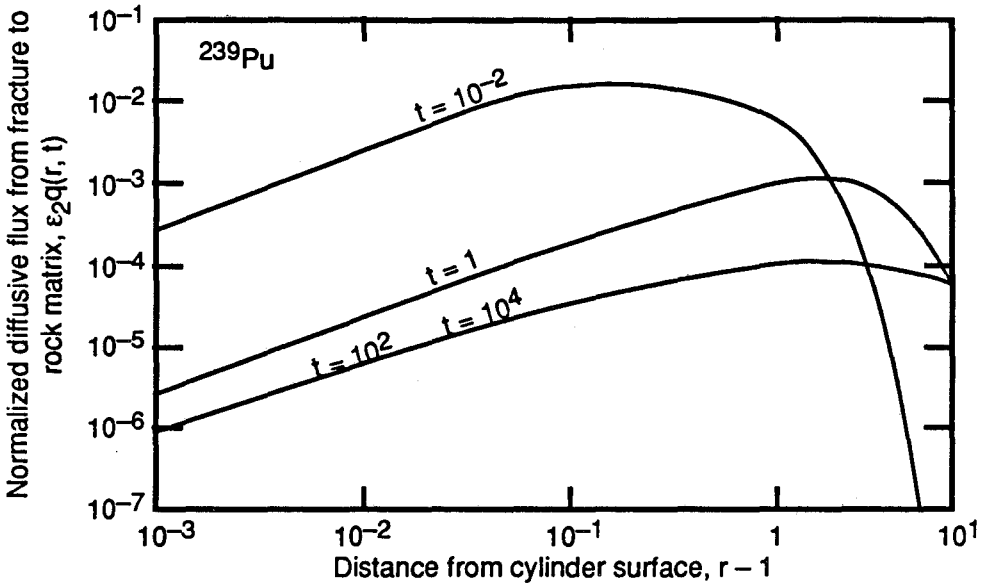

Figure 8.6 Diffusive flux across the interface between rock and fracture from fracture to rock matrix, as a function of distance from the cylinder surface. The curve for Fourier number of 10,000 is so close to that for 100.

8.5.3 Validity of the Cylinder Model

As the material is released, the cylinder radius will decrease with time. So the boundary conditions (8.21) and (8.23) might be valid within limited time. Considering that actinides have very low solubilities [13], one could make the following argument related to the validity of the assumption of constant cylinder radius. Because of their low solubilities, actinides will precipitate immediately after they are released from the cylinder. Even though the cylinder itself shrinks, nuclides will remain as a form of precipitates around the region where originally the cylinder exists, and the concentration at $r = 1$ might be maintained at their solubilities.

Rather, from assumed finite initial inventory of radionuclides in the waste cylinder, we must have an upper bound of time for applicability of the present model. For this purpose we consider a cumulative mass release from the cylinder. Here, to simplify, we assume that radionuclides do not move inside the cylinder along the z-direction. Then, the

material diffusing into the fracture comes only from a slice of the cylinder of width $2\hat{b}$. Because the material in the slice is released faster than that in the rest of the cylinder exposed to the rock matrix, we consider a cumulative mass release from the entire surface connected with the fracture to the fracture, which is defined as:

$$\hat{\dot{M}}_1(\hat{t}) = \int_0^{\hat{t}} \hat{j}_1(\hat{\tau})\, d\hat{\tau} \cdot 2\pi\hat{a} \cdot 2\hat{b} \quad [g]. \tag{8.82}$$

By (8.27) and (8.13), (8.82) can be written in terms of Fourier number and nondimensionalized flux as:

$$\hat{\dot{M}}_1(t) = 4\pi\hat{a}^2 \hat{b} K_2 \frac{\hat{D}_1}{\hat{D}_2} \hat{N}^* \int_0^t j_1(\tau) d\tau \quad [g], \tag{8.83}$$

where t is Fourier number. If the initial inventory of the nuclide of interest in the unit length of the waste cylinder is $\hat{w}^o$ [g/cm], amount of the nuclide in the slice of the cylinder $2\hat{b}$ is $2\hat{b}\cdot\hat{w}^o$ [g]. Normalized with this amount, the cumulative release of the nuclide is now written as:

$$\dot{M}_1(t) = R \int_0^t j_1(\tau)\, d\tau, \quad \text{where } R = \frac{2\pi \hat{a}^2 \hat{K}_2 \hat{D}_1 \hat{N}^*}{\hat{w}^o \hat{D}_2}. \tag{8.84}$$

Then the present model is considered to be valid until $\dot{M}_1(t)$ becomes unity.

For a spent fuel we assume $\hat{L}$ = 300 cm, where $\hat{L}$ is the length of a spent-fuel assembly. In one assembly, there are 2,300 g of ^{239}Pu, 230 g of ^{241}Am, and 88 g of ^{234}U [13]. If the solubility of these three nuclides is assumed to be $\hat{N}^* = 10^{-9}$ g/cm^3, we have:

For ^{239}Pu, $\hat{w}^o = 7.67$ g/cm, $R = 2.56 \times 10^{-4}$

For ^{241}Am, $\hat{w}^o = 0.767$ g/cm, $R = 2.56 \times 10^{-3}$

For ^{234}U, $\hat{w}^o = 0.293$ g/cm, $R = 6.70 \times 10^{-3}$.

In Figure 8.7 plotted are $\dot{M}_1(t)$ versus Fourier number. These curves reach unity at 10^4 for ^{239}Pu, 470 for ^{241}Am and ^{234}U.

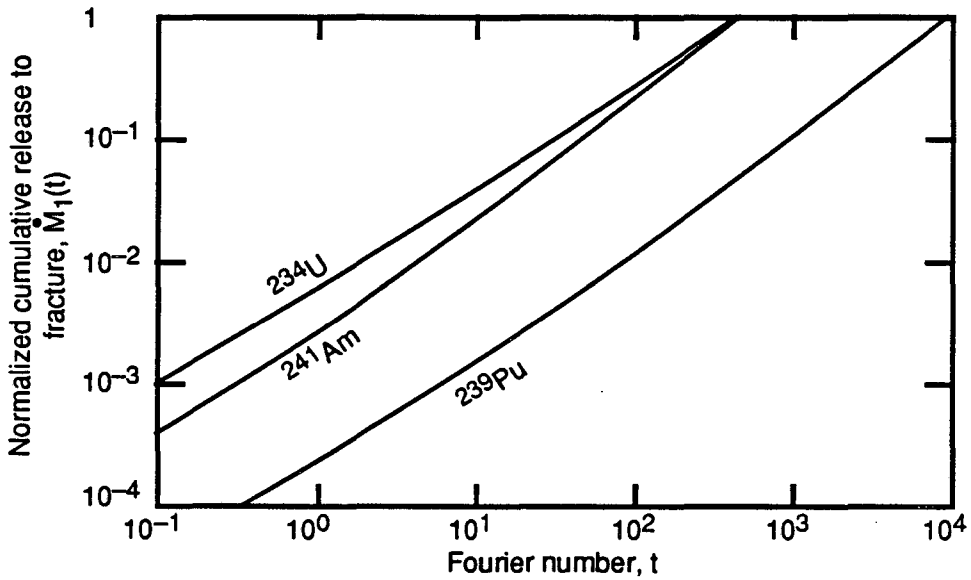

Figure 8.7 Cumulative mass release from the cylinder to the fracture, normalized by the initial inventory of each radionuclide in the slice of the cylinder exposed to the fracture.

In Figure 8.8 amount of radionuclide released into rock matrix is compared with that into the fracture. Instantaneous release rate into the fracture is defined as:

$$\dot{\hat{m}}_1(t) = 2\hat{b} \cdot 2\pi\hat{a}\,\hat{j}_1(t) = 4\pi\hat{a}\,\hat{D}_2\hat{N}^*\left(\varepsilon_1 \frac{\hat{b}}{\hat{a}} \frac{\hat{D}_1}{\hat{D}_2}\right) j_1(t) \qquad (8.85)$$

Instantaneous release rate into the rock matrix is defined as:

$$\dot{\hat{m}}_2(t) = 2 \times 2\pi\hat{a} \int_0^{\frac{\hat{L}}{2}-\hat{b}} \hat{j}_2(\hat{z}, t)\, d\hat{z} = 4\pi\hat{a}\hat{D}_2\hat{N}^* \varepsilon_2 \int_0^{\frac{\hat{L}}{2\hat{a}}-\frac{\hat{b}}{\hat{a}}} j_2(z, t)\, dz. \qquad (8.86)$$

In Figure 8.8 release rates are normalized by the factor $4\pi\hat{a}\hat{D}_2\hat{N}^*$. Even through the mass flux from the waste into the rock matrix is low relative to that into fracture, the larger waste surface exposed to the matrix and the greater assumed matrix sorption result in greater release rate to the matrix than to the fracture. This indicates that for the parameters

assumed here, the earlier mass-transfer theory [14] for a waste solid completely surrounded by porous rock can adequately predict release rates in low-flow conditions in fractured rock. If tortuosity significantly reduces the diffusion coefficient in the rock matrix and not in the fracture, mass-transfer directly from the waste to the fracture becomes more important.

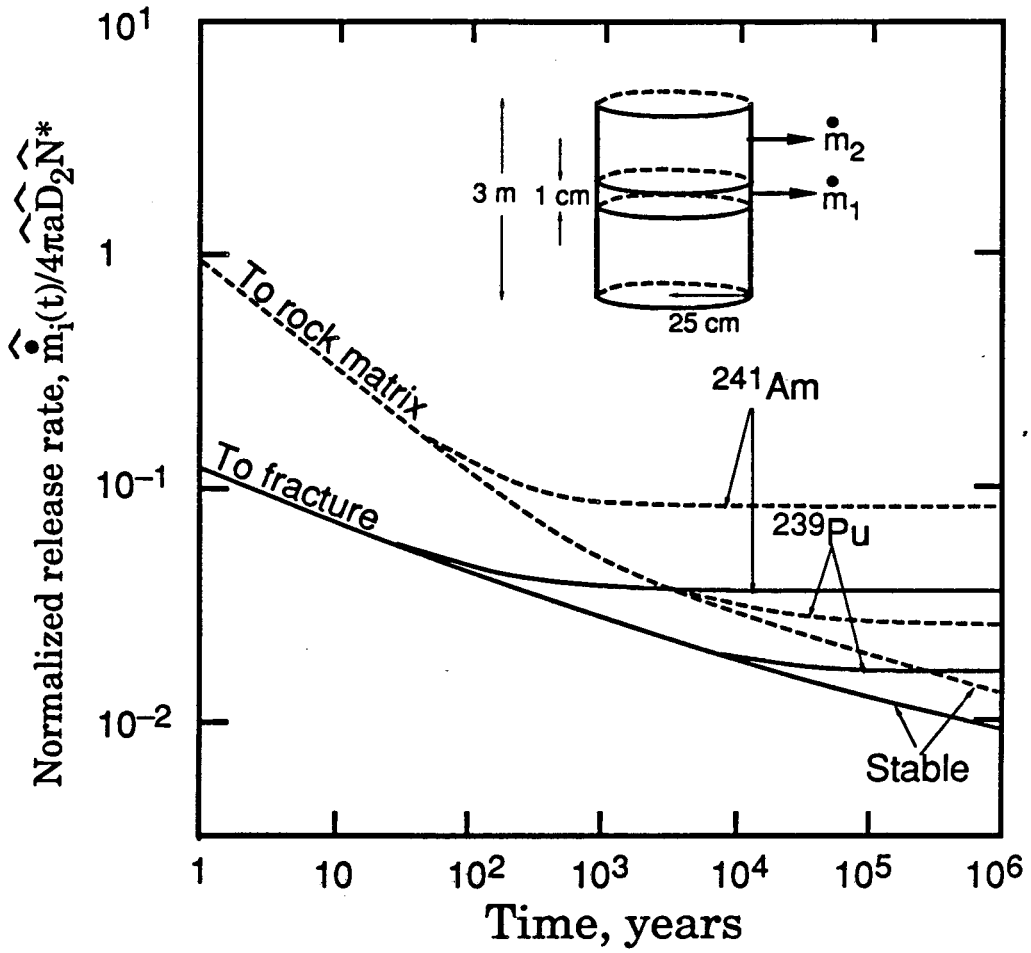

Figure 8.8 Normalized release rates of nuclides from a 3 m-high waste cylinder. Geologic parameters from Figure 8.2 apply.

8.5.4 Comparison for the Cylinder Model with the Plane Model

In Chapter 2 we studied the one-dimensional advective-dispersive transport in the fracture associated with one-dimensional matrix diffusion in the planar geometry. The

contaminant is released only to the fracture. We compare in this section the plane model with the cylinder model.

To compre, we make the following assumptions for the plane model. The planar source exposed to the fracture is assumed to be the constant-concentration boundary. Then, the boundary condition (2.14) can be written as:

$$N(0, t) = \psi(t) \equiv \hat{N}^{*} h(t). \tag{8.87}$$

No advection is assumed in the fracture ($v = 0$).

The both models can be compared in two ways. First, we can compare them from the standpoint of mass transfer from the source. The diffusive mass flux from the source to the fracture is obtained in the both models. Second, comparison is possible from the standpoint of far-field transport.

For the mass transfer from the source, we need to derive the expression for the mass flux from the plane source to the fracture, comparable to (8.27a). By setting v and z to be zero and $\psi(t)$ to be as (8.87) in (2.38), we can obtain the mass flux as:

$$\hat{j}_p(\hat{t}) = \frac{\hat{N}^{*}}{\sqrt{\pi}} \sqrt{\hat{A}\hat{D}\hat{R}_f} \int_0^{\sqrt{\hat{t}/\hat{A}}} \left\{ exp\left(-\frac{\mu^4}{4(\hat{t} - \mu^2\hat{A})} - \hat{\lambda}\hat{t} \right) \left[\left(\hat{\lambda} - \frac{\sqrt{\hat{\lambda}}}{\hat{A}} \right) H\left(\frac{\mu^2}{2\sqrt{\hat{\lambda}(\hat{t} - \mu^2\hat{A})}} + \sqrt{\hat{\lambda}(\hat{t} - \mu^2\hat{A})} \right) + \frac{1}{\hat{A}} \frac{2\hat{t} - \mu^2\hat{A}}{(\hat{t} - \mu^2\hat{A})^{3/2}} \right] + \left(\hat{\lambda} + \frac{\sqrt{\hat{\lambda}}}{\hat{A}} \right) e^{-\hat{\lambda}\hat{A}\mu^2 - \sqrt{\hat{\lambda}}\mu^2} \right.$$

$$\left. \times erfc\left(\frac{\mu^2}{2\sqrt{\hat{t} - \mu^2\hat{A}}} - \sqrt{\hat{\lambda}(\hat{t} - \mu^2\hat{A})} \right) \right\} d\mu, \quad \hat{t} > 0, \tag{8.88}$$

where

$$\hat{A} = \frac{\hat{b}\hat{R}_f}{\varepsilon\sqrt{\hat{D}_p \hat{R}_p}},$$

and ε, $\hat{R}_f$, $\hat{R}_p$, $\hat{D}_f$, and $\hat{D}_p$ are defined in Chapter 2. Here the symbol ^ is put to make the

notation consistent with that of the cylinder model. The subscript p stands for the planar geometry.

For the comparison of the features of the far-field transport, the steady-state solutions are useful. From (8.54), as t increases, the concentration in the fracture for the cylinder case approaches:

$$N_1^s(r) = \frac{K_0\left(\sqrt{\lambda}\, r\right)}{K_0\left(\sqrt{\lambda}\right)} - \frac{2}{\pi}(\Delta - 1)\lambda \int_0^{\infty} \frac{1}{\mu_2^2\left(\mu_1^2 + \mu_2/b\right)} \frac{\Phi(r,p)}{\left[M_0(p)\right]^2}\, pdp,\ r \geq 1. \quad (8.89)$$

Superscript s stands for steady state. For the plane model, we can obtain from (2.41) the steady-state solution for the concentration in the fracture for the case of zero advection and the constant-concentration boundary as:

$$\hat{N}^s(\hat{z}) = \hat{N}^* exp\left\{-\sqrt{\frac{\hat{\lambda}\hat{R}_f}{\hat{D}} + \frac{\varepsilon\sqrt{\hat{D}_p \hat{\lambda}\hat{R}_p}}{\hat{D}\hat{b}}}\ \hat{z}\right\}, \quad (8.90)$$

where $\hat{z}$ is the distance from the plane source.

In the numerical results shown in Figures 8.9 and 8.10, the following values are assumed:

Table 8.1 Summary of Assumed Parameter Values

		nomenclature		value
		cylinder	plane	
cylinder radius		$\hat{a}$	—	25 cm
fracture aperture		$\hat{b}$		1 cm
porosity:	fracture	ε_1	—	1
	rock	ε_2	ε	0.01
water velocity		—	v	0
retardation coefficients	fracture	$\hat{R}_1$	$\hat{R}_f$	1
	rock	$\hat{R}_2$	$\hat{R}_p$	500
diffusion coefficients	fracture	$\hat{D}_1$	$\hat{D}$	0.05 m^2/yr
	rock	$\hat{D}_2$	$\hat{D}_p$	0.05 m^2/yr

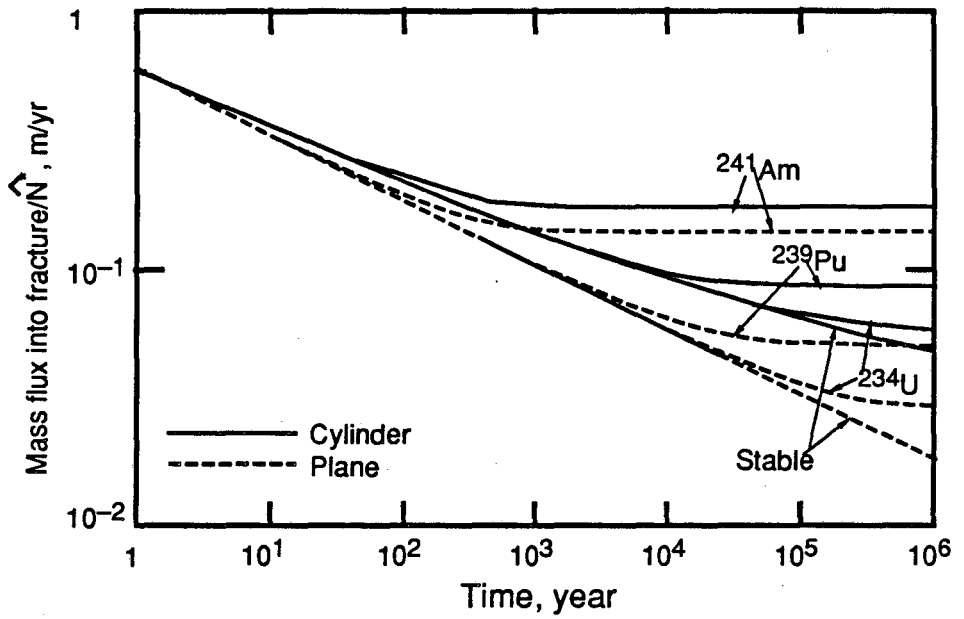

Figure 8.9 Comparison of the diffusive mass flux from the source in the cylinder model with that in the plane model. Parameter values in Table 8.1 apply.

In Figure 8.9 the mass flux from the source, normalized by the source-boundary concentration, is plotted against time in years. For the cylinder case, the curves are identical to the curves in Figure 8.3; the scaling of the both axes are changed. In early times the both geometry gives very close results. As time proceeds, the plane model yields smaller mass fluxes, and the difference between the two models at the steady state is greater for longer-lived radionuclides.

In the cylindrical geometry, the contaminant is diluted with more volume of the medium as it progresses farther away from the cylinder-source surface. So the mass transfer from the source is enhanced in the cylindrical geometry, compared with the planar geometry. On the other hand, becuase there is no matrix diffusion parallel to the fracture, the diffusive flux at the interface between fracture and rock becomes larger in the plane model than in the cylinder model, especially in the vicinity of the source surface. More nuclides would be removed from the fracture in the plane model, resulting in the enhanced mass transfer from the source. Then a question is, which is more dominant, the geometry effect or the diffusion into the rock matrix? The numerical results in Figure 8.9 show that

the cylindrical geometry enhances the mass transfer from the source more than does one-dimensional matrix diffusion.

In Figure 8.10, the normalized concentration in the fracture at the steady state is compared. The horizontal axis represents the distance from the source surface; in the cylinder case, $\hat{r} - \hat{a}$, and in the plane case, $\hat{z}$. In the region near the source, the plane model gives greater concentration, whereas in the far region the cylinder model is more conservative. For shorter half-life nuclides such as ^{241}Am, the difference is negligible, but for ^{234}U, the difference is prominent.

Because the contaminant is released into the rock matrix as well as to the fracture in the cylinder model, less contaminant in the fracture can diffuse into the rock matrix than in the plane model. Consequently, more nuclides stay and are transported in the fracture, resulting in greater concentration in the far field. For short-lived nuclides, because radioactive decay is predominant, effect of parallel matrix diffusion is not apparent.

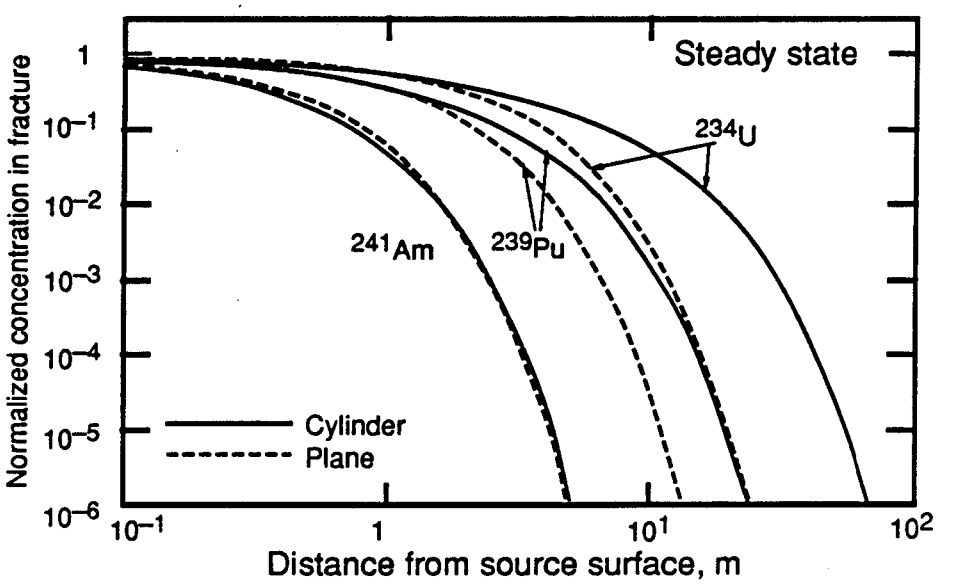

Figure 8.10 Concentration profiles in the fracture, normalized by the source concentration. Parameter values in Table 8.1 apply.

Thus both for the near-field mass transfer and for the far-field transport, the

cylinder model gives conservative results, provided that molecular diffusion is the sole transport mechanism in the medium.

8.6 Conclusions

Both mass fluxes to the fracture and to the rock matrix for radionuclides reach the steady state. Shorter half-life nuclides reach the steady state earlier. In very early times effect of radioactive decay is negligible.

Because of diffusion from fracture to rock, the mass flux from the cylinder to rock matrix is smaller in the region near the fracture than in far region. The effect of presence of the fracture is limited in a very shallow region in the rock matrix in eaaly times. From the numerical result for ^{239}Pu, after Fourier number of 100, the fracture effect on the mass flux from the cylinder to rock matrix can be neglected, and the mass flux to the rock matrix becomes virtually independent of z.

The present model is applicable until the nuclide, which initially exists in the slice of the cylinder exposed to the fracture, is all released into the fracture.

Although the mass flux to the fracture is hundred-fold larger than that to the rock matrix because of complete openness of the fracture, total amount of the nuclide released into the rock matrix at a certain time becomes in some cases greater than that to the fracture because the surface area contacted with the rock matrix is much larger than that with the fracture. If it is the case, the model for the cylinder surrounded completely by rock matrix is still good.

Three-dimensional diffusion in the rock matrix and the release from the cylinder to the rock matrix as well as to the fracture result in a quite different feature of transport in the fracture, if compared with the transport in the planar geometry as done in Chapter 2. The cylinder model is more conservative than the plane model with respect to the mass transfer from the source and to the far-field transport.

References

[1] Chambré, P. L., and T. H. Pigford, Predictions of Waste Performance in a Geologic Repository, *Scientific Basis for Nuclear Waste Management VII*, edited by G. L. McVay, New York: Elsevier, 985, 1983,

[2] Griffith, J. L., On Weber Transforms, *J. and Proc. of the Royal Soc. New South Wales, LXXXIX, Part 4*, 232, 1955,

[3] Abramowitz, M., and I. A. Stegun, *Handbook of Mathematica Functions with Formulas, Graphs, and Mathematical Tables*, 10th ed., Chapter 29, Dover, New York, 1972,

[4] *ibid.*, Identity 9.1.16,

[5] Carslaw, H. S., and J. C. Jaeger, *Conduction of Heat in Solids*, Second ed., §13.5, Oxford Univ. Press, New York, 1959,

[6] NAG library Mark 10, Numerical Algorithm Group,

[7] Piessens, R., E. deDoncker-Kapenga, C. W. Überhuber, and D. K. Kahaner, *QUADPACK : A Subroutine Package for Automatic Integration*, Springer-Verlag, Berlin Heidelberg, 1983,

[8] Davis, P. J., and P. Rabinowitz, *Methods of Numerical Integration*, Second ed., Academic Press, Orlando, 1984,

[9] Same as [3], Identity 9.4.2,

[10] Gradshteyn, I. S., and I. M. Ryzhik, *Table of Integrals, Series, and Products*, Corrected and Enlarged Ed., Identity 2.141, Academic Press, Orlando, 1980,

[11] Salzer, H. E., Formulas for Calculating the Error Function of a Complex Variable, *Math. Tables Aids Comp., 5*, 67, 1951,

[12] Shanks, D., Non-Linear Transformations of Divergent and Slowly Convergent Sequences, *J. Math. and Phys., 34*, 1, 1955,

[13] Waste Isolation Systems Panel, Board on Radioactive Waste Management, National Research Council, *A Study of the Isolation System for Geological Disposal of*

Radioactive Waste, National Academy Press, Washington D. C., 1983,

[14] Chambré, P. L., T. H. Pigford, Y. Sato, A. Fujita, H. Lung, S. Zavoshy, and R. Kobayashi, *Analytical Performance Models for Geologic Repositories,* LBL-14842, Lawrence Berkeley Lab., 1982.

Chapter 9
Conclusions

The purpose of this dissertation is to obtain a bounding model which predicts transport of radionuclides through a fractured porous rock.

As a conclusion, the following bounding model has been obtained. Proceeding from the assumption of a discrete planar fracture surrounded by porous rock, where water is assumed to be at rest, the transport of radionuclides can be conservatively predicted by taking into account one-dimensional advection in the fracture, one-dimensional molecular diffusion perpendicular to the fracture in the rock matrix, sorption equilibrium in the fracture and in the rock matrix, and radioactive decay without precursing nuclides. Matrix diffusion is the most important feature in the fracture-flow transport.

The bounding model has the following limitations:

(1) In early times, longitudinal hydrodynamic dispersion enhances advective transport in the fracture. One can neglect longitudinal dispersion by assuming large fracture aperture and water velocity.

(2) The bounding model can be used for the case of the multiple-patch source with transverse dispersion in the fracture at some distance away from the source. In very far region the equivalent-single-patch model is more accurate.

(3) The discrete-fracture model can be used for the case of moderate overlap of concentration fields in the rock matrix in between two adjacent parallel fractures. If fractures are intersected each other frequently, the analysis based on the assumption of parallel fractures does not apply; effects of intersection may be taken into aacount by longitudinal dispersion.

(4) Neglecting the mother nuclide results in optimistic estimates of concentration in the fracture in early times, if both the mother and the daughter nuclides exist in the source initially. For the nuclides that initially do not exist in the source, such as ^{230}Th and

^{226}Ra, decay chain must be included in the formulation.

(5) If advection is negligible and mass transfer from the source and transport in the fracture and in the rock matrix are controlled by molecular diffusion, the cylindrical geometry and the molecular diffusion parallel to the fracture in the rock matrix must be assumed for obtaining conservative evaluations. The planar geometry and one-dimensional matrix diffusion perpendicular to the fracture no longer give conservative results.

Appendix A: Derivation from (3.3) to (3.11)

Suppose the function $\psi(t)$ can be differentiated once, and its derivative is again an integrable function. By integrating (3.3) by parts with respect to t', we obtain:

$$N(T_n, t) = \frac{2}{\sqrt{\pi}} e^{\frac{Pe}{2}} \int_g^\infty G(\xi; T_n, t, Pe)\, e^{-\gamma\lambda} \{ f(t-\gamma)\,\psi(0) - f(0)\,\psi(t-\gamma) \}\, d\xi$$

$$- \frac{2}{\sqrt{\pi}} e^{\frac{Pe}{2}} \int_g^\infty G(\xi; T_n, t, Pe)\, e^{-\gamma\lambda} \int_0^{t-\gamma} \frac{d\psi}{dt'}(t-\gamma-t') f(t') dt'\, d\xi, \qquad (A.1)$$

where $f(t')$ can be defined as the indefinite integral of $E(t;\frac{\gamma}{A})$:

$$f(t') \equiv \int^{t'} E(t'; \tfrac{\gamma}{A})\, dt' = \frac{-1}{2} \left\{ e^{\frac{\gamma\sqrt{\lambda}}{A}} erf\left(\frac{\gamma}{2A\sqrt{t'}} + \sqrt{\lambda t'} \right) + e^{-\frac{\gamma\sqrt{\lambda}}{A}} erf\left(\frac{\gamma}{2A\sqrt{t'}} - \sqrt{\lambda t'} \right) \right\}$$

$$+ Constant. \qquad (A.2)$$

Now we take A to infinity. The first integral in (A.1) satisfies the following conditions [1]: (i) $\int_g^\infty G(\xi; T_n, t, Pe))\, e^{-\gamma\lambda}\, d\xi$ converges absolutely, and (ii) $\{f(t-\gamma)\psi(0) - f(0)\,\psi(t-\gamma)\}$ converges uniformly over any finite subdomain of $\xi \geq g$ to a function $\psi(t-\gamma)$ by taking A to infinity. Then, we can change the order of integration with respect to ξ and the limit operation with repsect to A, obtaining

$$\begin{pmatrix} \textit{the first term} \\ \textit{of the r. h. s.} \\ \textit{of (A.1)} \end{pmatrix} = \frac{2}{\sqrt{\pi}} e^{\frac{Pe}{2}} \int_g^\infty G(\xi; T_n, t, Pe)\, e^{-\gamma\lambda} \psi(t-\gamma) d\xi$$

The second integral in (A.1), we consider the limit:

$$\lim_{A\to\infty} \int_0^{t-\gamma} \frac{d\psi}{dt'}(t-\gamma-t')\, f(t')\, dt'$$

In $0 \leq t' \leq t-\gamma$, $f(t')$ is continuous, and converges uniformly to zero by taking A to infinity for $\xi \geq g$, $t \geq 0$, $T_n \geq 0$. Hence the above limit converges uniformly to zero. The

two conditions given above for changing the order of integration and limit operation are satisfied also in case of the second integral. Then we can change the orger of integration with respect to ξ and the limit operation, obtaining zero. Thus the result follows.

Reference for Appendix A

[1] Chambré, P. L., and E. J. Pinney, *Notes for Mathematics 120*, Theorem 6.1.9, Department of Mathematics, University of California, Berkeley, 1985.

Appendix B: Derivation of the Green's Function for (4.9)

In eq. (4.2), we change the variables as follows:

$$M(y, z, t) = e^{-\lambda t} K(\eta; z, t), \tag{B.1a}$$

$$\eta = B(y - b). \tag{B.1b}$$

Then, (4.2) reduces to

$$\frac{\partial K}{\partial t} = \frac{\partial^2 K}{\partial \eta^2}, \qquad \eta > 0, t > 0, z > 0. \tag{B.2}$$

The initial condition for (B.2) is defined as

$$K(\eta; z, 0) = \Psi(\eta, z), \quad \eta > 0, z > 0. \tag{B.3}$$

Applying Laplace transform on (B.2) yields:

$$\frac{d^2 \tilde{K}}{d\eta^2} - pK + \Psi(\eta, z) = 0, \qquad \eta > 0. \tag{B.4}$$

Instead of (4.9), we consider the Green's function for (B.4).

(1) First, we solve (B.4) in a finite span, $0 < \eta < l$, with homogeneous boundary conditions, i.e.,

$$\tilde{K}(0; z, p) = \tilde{K}(l; z, p) = 0. \tag{B.5}$$

To have a unique solution, which can be written in terms of the Green's function $\bar{G}(\eta, s)$ for a finite span, p must *not* an eigen value of the self-adjoint linear operator, $\frac{d^2}{d\eta^2}$. Otherwise, the problem becomes the Strum-Liouville problem. Thus p must satisfy the restriction:

$$p \neq -\frac{n^2 \pi^2}{l^2}, \qquad n = 0, 1, 2, \ldots. \tag{B.6}$$

If the Green's function is obtained, the solution for (B.4) subject to the homogeneous boundary conditions (B.5) is written as

$$\tilde{K}(\eta; z, p) = \int_0^l \bar{G}(\eta, s)\, \Psi(s, z)\, ds. \qquad (B.7)$$

Th following is the derivation of the Green's function for the finite span. The Green's function can be obtained by solving a problem:

$$\frac{d^2\bar{G}}{d\eta^2} - p\bar{G} = -\delta(\eta - s), \quad 0 < \eta < l, \quad 0 < s < l, \qquad (B.8a)$$

subject to

$$\bar{G}(0, s) = \bar{G}(l, s) = 0. \qquad (B.8b)$$

Let $u_1(\eta)$, $u_2(\eta)$ be the solutions to the problem (B.8a,b) satisfying the boubndary conditions of (B.8b) individually, and C_1, C_2 be certain constants. Then, the Green's function has the form of

$$\bar{G}(\eta, s) = \begin{cases} C_1 u_1(\eta), & 0 \le \eta \le s \\ C_2 u_2(\eta), & s \le \eta \le l \end{cases} \qquad (B.9)$$

By continuity at $\eta = s$, $C_1 = Cu_2(s)$, $C_2 = Cu_1(s)$, C a constant. Then, (B.9) can be written as:

$$\bar{G}(\eta, s) = \begin{cases} C\, u_2(s)\, u_1(\eta), & 0 \le \eta \le s \\ C\, u_1(s)\, u_2(\eta), & s \le \eta \le l \end{cases}$$

The constant is obtained by the jump conditions [1] at $\eta = s$:

$$C\left[u_1(s)\, u_2'(s) - u_2(s)\, u_1'(s)\right] = -1. \qquad (B.10)$$

Considering that $u_1(\eta) = sinh(\sqrt{p}\,\eta)$, $u_2 = sinh(\sqrt{p}\,(\eta - l))$, we obtainn from (B.10) the constant as

$$C = -\frac{1}{\sqrt{p}} \frac{1}{sinh(\sqrt{p}\, l)}. \qquad (B.11)$$

Thus, the Green's function for the finite span is obtained as:

$$\bar{G}(\eta, s) = \frac{1}{\sqrt{p}\, sinh(\sqrt{p}\, l)} \times \begin{cases} sinh(\sqrt{p}\,(l - s))\, sinh(\sqrt{p}\,\eta), & 0 \le \eta \le s \\ sinh(\sqrt{p}\, s)\, sinh(\sqrt{p}\,(l - \eta)), & s \le \eta \le l \end{cases} \qquad (B.12)$$

(2) Next, we consider the problem (B.4) in a semi-infinite span, $0 < \eta < \infty$. The solution for this problem is obtained by taking the limit of $l \to \infty$ in (B.7), i.e.,

$$\tilde{K}(\eta; z, p) = \lim_{l \to \infty} \frac{\sinh(\sqrt{p}\,(l-\eta))}{\sqrt{p}\,\sinh(\sqrt{p}\,l)} \int_0^{\eta} \sinh(\sqrt{p}\,s)\,\Psi(s, z)\,ds$$

$$+ \lim_{l \to \infty} \frac{\sinh(\sqrt{p}\,\eta)}{\sqrt{p}} \int_{\eta}^{l} \frac{\sinh(\sqrt{p}\,(l-s))}{\sinh(\sqrt{p}\,l)}\,\Psi(s, z)\,ds \qquad (B.13)$$

Let us conisder the factor before the first integral of the right hand side of (B.13). Substituting $p = R\,e^{i\theta}$, $R > 0$, $-\pi < \theta < \pi$, into $e^{-\sqrt{p}\,l}$ yields

$$e^{-\sqrt{p}\,l} = e^{-\sqrt{R}\,l\cos\frac{\theta}{2}} \left\{ \cos\left(\sqrt{R}\,l\sin\frac{\theta}{2}\right) - i\sin\left(\sqrt{R}\,l\sin\frac{\theta}{2}\right) \right\} \qquad (B.14)$$

Since $\cos\frac{\theta}{2} > 0$, the exponential factor in the right hand side of (B.14) vanishes if l goes to infinity. Thus (B.14) goes to zero if l becomes infinity. Similarly, $e^{-\sqrt{p}(l-\eta)}$ becomes zero since $l > \eta$. Therefore, the factor before the first integral in (B.13) becomes $e^{-\sqrt{p}\,\eta}/\sqrt{p}$ if $l \to \infty$.

For the second integral, we show the following points to exchange the order of limit operation and integration [2]:

(i) As l tends to infinity, $\frac{\sinh\{\sqrt{p}(l-s)\}}{\sinh(\sqrt{p}l)}$ converges uniformly to a certain function $F(s)$.

(ii) $\left|\frac{\sinh\{\sqrt{p}(l-s)\}}{\sinh(\sqrt{p}l)}\right| < \exists\, G(s),\ 0 < s < l.$

(iii) $\int_{\eta}^{\infty} G(s)\Psi(s, z)ds$ converges absolutely.

For point (i), we have already shown in the first integral of (B.13). For the second point, $G(s) = C\,e^{-\kappa s}$, $0 < s < l$. If we assume that the obtained $G(s)$ satisfies the third condition, we can exchange the order of limit operation and integration in (B.13), resulting in:

$$\tilde{K}(\eta; z, p) = \int_0^\infty \frac{1}{2\sqrt{p}} \left\{ e^{-|\eta - s|\sqrt{p}} - e^{-(\eta + s)\sqrt{p}} \right\} \Psi(s, z)\, ds \qquad (B.15)$$

Therefore, the Green's function for the semi-infinite span is obtained as

$$G(\eta, s) = \frac{1}{2\sqrt{p}} \left\{ e^{-|\eta - s|\sqrt{p}} - e^{-(\eta + s)\sqrt{p}} \right\}, \quad 0 < \eta < \infty, \quad 0 < s < \infty. \quad (B.16)$$

By the variable transformations defined by (B.1a,b), the Green's function for (4.9) is finally obtained.

References for Appendix B

[1] Chambré, P. L., *Notes for Mathematics 220A/B*, Department of Mathematics, University of California, Berkeley, 1984—1985,

[2] Chambré, P. L., and E. J. Pinney, *Notes for Mathematics 120*, Theorem 6.1.9, Department of Mathematics, University of California, Berkeley, 1985.

Appendix C: Errors in Sudicky and Frind's Solutions for Multiple Parallel Fractures

In Sudicky and Frind's solutions for $N(z, t)$, they changed the order of the integrations of μ and t' in (5.3) and (5.5), and performed the integration with respect to t'. This results in, for the case of $D = 0$,

$$N(z, t)/N^o = \frac{e^{-\lambda ZA}}{\pi} h(\tau^o) \int_0^\infty \frac{\mu e^{\mu_R^o}}{\lambda^2 + \mu^4/4} \left[e^{-\lambda\tau^o} \left\{ \frac{\mu^2}{2} sin(\mu_g^o|_{\tau^o}) - \lambda cos(\mu_g^o|_{\tau^o}) \right\} \right.$$

$$\left. + \frac{\mu^2}{2} sin(\Omega^o) + \lambda cos(\Omega^o) \right] d\mu, \qquad (C.1)$$

However, (C.1) does not satisfy the boundary condition at $z = 0$, (5.2). If we substitute $z = 0$ into (C.1), we obtain:

$$N(0, t)/N^o = \frac{h(t)}{\pi} \int_0^\infty \frac{\mu}{\lambda^2 + \mu^4/4} \left[e^{-\lambda t} \left\{ \frac{\mu^2}{2} sin\left(\frac{\mu^2 t}{2}\right) - \lambda cos\left(\frac{\mu^2 t}{2}\right) \right\} + \lambda \right] d\mu, \quad (C.2)$$

which cannot be reduced to $h(t)$. This error stems from changing the order of integration of μ and t'. This operation is valid only if the following conditions are met [1] (We consider the case for zero dispersion, but very similar argument applies for the case of non-zero dispersion): (1) $\exp(-\lambda t')\cos(\mu_g^o|_{t'})$ is continuous and bounded for t' and μ on the intervals $0 \le t' \le \tau^o$ and $0 \le \mu < \infty$, and (2) the integral $\int_0^\infty \mu \exp(\mu_R^o) d\mu$ converges absolutely. The second condition cannot be met if $z = 0$ because with $z = 0$ we have $\mu_R^o = 0$, and the integral does not converge at all. Thus (5.3) and (5.5) must be the exact solutions for $N(z, t)$ instead of theirs.

Let us check if (5.3) and (5.5) actually satisfy the boundary condition (5.2). By substituting $z = 0$ into (5.5) we obtain:

$$N(0, t)/N^o = \frac{1}{\pi} \int_0^t e^{-\lambda t'} \int_0^\infty \mu cos\left(\frac{\mu^2 t'}{2}\right) d\mu dt'. \qquad (C.3)$$

Considering the integral with respect to μ,

$$\int_0^\infty \frac{\mu}{\pi} \cos\left(\frac{\mu^2 t'}{2}\right) d\mu = \int_0^\infty \frac{\cos(xt')}{\pi} dx = \left[\frac{\sin(xt')}{\pi t'}\right]_0^\infty = \lim_{x\to\infty} \frac{\sin(xt')}{\pi t'} = \delta(t'), \qquad (C.4)$$

where $\delta(t')$ is Dirac's delta function, (C.3) becomes unity for positive t. Thus (5.5) satisfies the boundary condition (5.2). For (5.3) procedures are very similar.

Their solutions to $M(y, z, t)$ contain two different kinds of errors. These are pointed out independently in [2]. One type of errors comes from the incorrect time integration. When they obtained the expressions for $M(y, z, t)$ by inverse Laplace transform of

$$\tilde{M}(y, z, p) = \tilde{N}(z, p)\,\tilde{f}(p), \qquad (C.5)$$

where

$$\tilde{f}(p) = \frac{\cosh\left(B\sqrt{p+\lambda}\,(S-y)\right)}{\cosh\left(B\sqrt{p+\lambda}\,(S-b)\right)}.$$

With the convolution theorem:

$$\mathcal{L}^{-1}\left[\tilde{f}_1(p)\,\tilde{f}_2(p)\right] = \int_0^t f_1(t')\,f_2(t-t')\,dt', \qquad (C.6)$$

they ignored that the lower limit, g, of the integration in $N(z, t)$ for non-zero dispersion with respect to ξ becomes a function of t'. In case of zero dispersion they apparently ignored the presence of $h(\tau^o)$ in (5.5) on substitution of their solution to $N(z, t)$ into (C.6).

After correction of these errors, their solution to $M(y, z, t)$ for zero or non-zero dispersion does not satisfy the boundary condition at the rock-fracture interface, (2.16). This is because the inverse transform of $\tilde{f}(p)$ in (C.5) is valid only in the region $b < y < 2S - b$ [3]. Hence their solutions for $N(z, t)$ are correct only in this region. In order to avoid this difficulty, we write the Laplace-transformed solution $\tilde{M}/N^o$ explicitly by substituting the Laplace-transformed solution $\tilde{N}/N^o$ into (C.5), and rearrange the terms as follows:

$$\tilde{M}(y, z, p) = \tilde{f}_1(p)\,\tilde{f}_2(p)$$

where

$$\tilde{f}_1(p) = \frac{\cosh\left(B\sqrt{p+\lambda}\,(S-y)\right)}{p\cosh\left(B\sqrt{p+\lambda}\,(S-b)\right)}, \qquad (C.7)$$

and

$$\tilde{f}_2(p) = N^o e^{\alpha z} \exp\left\{-\alpha z\sqrt{1+\beta^2\left(\frac{\sqrt{p+\lambda}}{A}\tanh\left(\sigma\sqrt{p+\lambda}\right)+(p+\lambda)\right)}\right\}, \quad \text{for } D \neq 0, \qquad (C.8a)$$

$$\tilde{f}_2(p) = N^o \exp\left\{-\frac{R_f z}{v}\left(p+\lambda+\frac{\sqrt{p+\lambda}}{A}\tanh\left(\sigma\sqrt{p+\lambda}\right)\right)\right\}, \quad \text{for } D = 0. \qquad (C.8b)$$

The inverse for (C.7) is now valid for $b \le y \le 2S - b$. And the correct solutions (5.4) and (5.6) are obtained.

Note that for (5.4) and (5.6) $z = 0$ is carefully excluded from their domain of definition because the cocnentration in the rock is considered only in the region $z > 0$. Therefore, we can exchange the order of integration with respect to μ and t' this time in the preceding forms of (5.4) and (5.6), which contain very similar forms to(5.3) and (5.5) respectively.

References for Appendix C

[1] Chambré, P. L., *Notes for Mathematics 120*, Theorem 6.1.12, Department of Mathematics, University of California, Berkeley, 1984,

[2] Davis, G. B., and C. D. Johnston, Comment on 'Contaminant Transport in Fractured Porous Media: Analytical Solution for a System of Parallel Fractures, *Water Resources Res., 20,* 1321, 1984,

[3] Oberhettinger, F., and L. Baddi, *Tables of Laplace Transforms,* Springer-Verlag, New York, 1973.

Appendix D: On Weber Transforms

(1) Derivation of (8.31)

Integrating the left hand side of (8.31) with respect to r, we obtain:

$$\int_1^r \frac{1}{r}\frac{\partial}{\partial r}\left(r\frac{\partial f}{\partial r}\right)\Phi(r,s)\,r dr = \left[r\frac{\partial f}{\partial r}\Phi(r,s)\right]_1^\infty - \int_1^\infty r\frac{\partial f}{\partial r}\frac{\partial \Phi}{\partial r}dr. \qquad (D.1)$$

For large arguments of $J_0(z)$ and $Y_0(z)$ [1],

$$J_0(z) \approx \sqrt{\frac{2}{\pi z}}\left\{\cos\left(z-\frac{\pi}{4}\right)+O\left(|z|^{-1}\right)e^{|Im\,z|}\right\}, \qquad (D.2a)$$

$$Y_0(z) \approx \sqrt{\frac{2}{\pi z}}\left\{\sin\left(z-\frac{\pi}{4}\right)+O\left(|z|^{-1}\right)e^{|Im\,z|}\right\}, \qquad (D.2b)$$

$$|arg\,z| < \pi, \qquad |z| \to \infty, \qquad z \text{ complex.}$$

For a real x, these reduce to

$$J_0(x) \approx \sqrt{\frac{2}{\pi x}}\left\{\cos\left(x-\frac{\pi}{4}\right)+O\left(x^{-1}\right)\right\}, \qquad (D.3a)$$

$$Y_0(x) \approx \sqrt{\frac{2}{\pi x}}\left\{\sin\left(x-\frac{\pi}{4}\right)+O\left(x^{-1}\right)\right\}, \qquad (D.3b)$$

$$x \to \infty$$

Therefore,

$$\Phi(r,s) \sim O\left(r^{-1/2}\right) \qquad (D.4)$$

We assume that $f(r)$ is Weber-transformable, i.e., the integral $\int_1^\infty f(r)\sqrt{r}dr$ exists [2], and $f(r)$ is continuous over $r \in [1, \infty)$. Then,

$$f(r) \sim O\left(r^{-1/2-\alpha}\right), \quad \frac{\partial f}{\partial r} \sim O\left(r^{-3/2-\alpha}\right), \quad \alpha > 0. \qquad (D.5)$$

Because $\Phi(1, s) = 0$, the first term of the right hand side of (D.1) vanishes. If we integrate the second term in the right hand side of (D.1) by parts once more, then we obtain:

$$\int_1^\infty r \frac{\partial f}{\partial r} \frac{\partial \Phi}{\partial r} dr = \left[r f(r) \frac{\partial \Phi}{\partial r} \right]_1^\infty - \int_1^\infty f(r) \frac{\partial}{\partial r} \left(r \frac{\partial \Phi}{\partial r} \right) dr. \qquad (D.7)$$

Similarly,

$$\lim_{r \to \infty} r f(r) \frac{\partial \Phi}{\partial r} = 0$$

At $r = 1$, $\frac{\partial \Phi}{\partial r}$ can be evaluated as follows [3]:

$$\left. \frac{\partial \Phi}{\partial r} \right|_{r=1} = s \left\{ -J_1(rs) Y_0(s) + J_0(s) Y_1(rs) \right\}_{r=1} = s \left(-\frac{2}{\pi s} \right) = -\frac{2}{\pi}$$

Therefore, the first term in the right hand side of (D.7) becomes:

$$\left[r f(r) \frac{\partial \Phi}{\partial r} \right]_1^\infty = \frac{2}{\pi} f(1) \qquad (D.8)$$

By differentiating $\Phi(r, s)$ twice with respect to r,

$$\frac{\partial}{\partial r} \left(r \frac{\partial \Phi}{\partial r} \right) = -s^2 \Phi(r, s). \qquad (D.9)$$

From (D.8) and (D.9), the result follows.

(2) Inverse Weber Transform of $\bar{W}_0(s)$

Consider the following problem:

$$\frac{1}{r} \frac{d}{dr} \left(r \frac{df}{dr} \right) - \lambda f = 0, \qquad r > 1, \qquad (D.10a)$$

subject to

$$f(1) = 1, \; f(\infty) = 0. \qquad (D.10b)$$

Applying Weber transform on (D.10a) yields

$$\bar{f}(s) = \frac{-2}{\pi} \frac{1}{s^2 + \lambda}. \qquad (D.11)$$

This implies that the Weber transform of the solution to (D.10a) is written as (D.11). The solution to (D.10a) is known as

$$f(r) = \frac{K_0\left(r\sqrt{\lambda}\right)}{K_0\left(\sqrt{\lambda}\right)} .$$

Then, the result follows.

References for Appendix D

[1] Abramowitz, M., and I. A. Stegun, *Handbook of Mathematical Functions with Formulas, Graphs, and Mathematical Tables,* 10th ed., Identities 9.2.1 and 9.2.2, Dover, New York, 1972,

[2] Griffith, J. L., On Weber Transforms, *J. and Proc. of the Royal Soc. New South Wales, LXXXIX, Part 4,* 232, 1955,

[3] Same as [1], Identity 9.1.16.

LAWRENCE BERKELEY LABORATORY
TECHNICAL INFORMATION DEPARTMENT
UNIVERSITY OF CALIFORNIA
BERKELEY, CALIFORNIA 94720